Endoscopic Low Coherence Interferometry Applied to Tri-Dimensional Contouring of Upper Airways

THÈSE N° 4287 (2009)

PRÉSENTÉE LE 13 FÉVRIER 2009
À LA FACULTE SCIENCES ET TECHNIQUES DE L'INGÉNIEUR
LABORATOIRE D'OPTIQUE APPLIQUÉE
PROGRAMME DOCTORAL EN PHOTONIQUE

ÉCOLE POLYTECHNIQUE FÉDÉRALE DE LAUSANNE

POUR L'OBTENTION DU GRADE DE DOCTEUR ÈS SCIENCES

PAR

Yves DELACRÉTAZ

acceptée sur proposition du jury:

Prof. O. Martin, président du jury
Prof. C. Depeursinge, Dr F. Lang, directeurs de thèse
Prof. A. Ettemeyer, rapporteur
Prof. G. Indebetouw, rapporteur
Prof. P. Jacquot, rapporteur

EPFL

ÉCOLE POLYTECHNIQUE
FÉDÉRALE DE LAUSANNE

Suisse
2009

En mémoire de Grand-Maman...

...Pour Nadine.

Version abrégée

Cette thèse présente une nouvelle technique optique de mesure topographique, ne nécessitant qu'une seule acquisition par courbe de niveau. La méthode est basée sur une mesure interférométrique utilisant une source de lumière à longueur de cohérence réduite, et est totalement intégrable aux procédures d'inspection endoscopiques communément utilisées en oto-rhino-laryngologie (ORL). Il a été démontré que cette méthode peut être appliquée avec succès à l'imagerie des voies aériennes supérieures sur un porc. Bien que la méthode utilise une approche interférométrique, le signal de phase n'est pas directement évalué, mais plutôt la position de la zone de superposition cohérente des deux ondes, ce qui rend la mesure robuste, même lorsque celle-ci est effectuée dans un environnement difficile. L'idée principale est de localiser des franges d'interférence intentionnellement créées au moyen de l'addition, dans une géométrie hors-axe, d'une onde de référence et d'une onde objet provenant d'un échantillon rugueux ou diffusant et ayant été collecté par un système optique à faible ouverture.

Un modèle décrivant la propagation de la lumière au travers du système a été développé. Ce modèle prend en compte le spectre d'émission élargi de la source lumineuse, ainsi que l'effet statistique du speckle induit par l'illumination d'une surface rugueuse avec une lumière partiellement cohérente. Les résultats simulés ont été précautionneusement comparés avec les mesures expérimentales, tant en ce qui concerne l'espace direct que l'espace de Fourier (espace des fréquences spatiales), ce qui a permis de mieux comprendre les processus impliqués dans la création des franges d'interférences, et également d'améliorer le design du dispositif.

Plusieurs méthodes de filtrage ont été étudiées dans le but d'extraire l'information de profondeur des interférogrammes acquis. En utilisant des bancs de filtres de Gabor, qui ne nécessitent aucune connaissance *a priori* du signal, la sélectivité du signal extrait a pu être améliorée d'un facteur 1.3 comparé à une simple évaluation locale du spectre de Fourier, et le temps de calcul divisé par 6, même en comparaison avec des méthodes itératives rapides dans le domaine des fréquences spatiales. De plus, en faisant une supposition sur la fréquence et/ou l'orientation du signal à extraraire, qui peuvent être obtenus par une simple procédure de calibration, il a été démontré que la sélectivité peut encore être augmentée d'un facteur 2.5, tout en gardant le même temps de calcul.

Un prototype compact a été construit, avec un arrangement comportant plusieurs fibres d'illumination. Le système est constitué de 2 parties: la première est adaptable sur un endoscope rigide. Cette partie contient une optique d'imagerie, des optiques pour recombiner le faisceau objet et le faisceau de référence, et le détecteur. Le volume de l'ensemble est de $115 \times 83 \times 94$ mm. La seconde partie contient la source laser, l'axe motorisé pour le balayage de l'objet, et les optiques d'injection dans les fibres optiques, elle est destinée à être posée sur un chariot. Ceci permet d'amener l'instrument de mesure au chevet du patient, ou de l'utiliser durant les procédures d'inspection endoscopiques classiques.

En conjonction avec le dispositif, une structure complète a été développée dans le but de simplifier au maximum la mesure, ainsi que le traitement du signal. Finalement, un environnement totalement automatisé a été mis en place, se chargeant du contrôle du matériel, de l'enregistrement des données, et du traitement du signal, jusqu'à la visualisation de la surface observée en trois dimensions

Mots clefs: Faible cohérence, interférométrie, endoscopie, single-shot, topographie, speckle, voies aériennes.

Abstract

This thesis presents a novel approach for optical tri-dimensional contouring, requiring only one acquisition to extract a contour depth. It is based on an interferometric setup, using a reduced coherence light source, and is fully adaptable to endoscopic procedure commonly in used in ear-nose-throat (ENT) medicine. It has been demonstrated that the method can be successfully applied to imaging of porcine upper airways. Although this method uses interferometry to obtain depth range measurement, the phase signal is not directly evaluated, rather the location of the coherent superposition of two waves is extracted, and thus provides a robust technique even in harsh environment. The key feature is to extract the coherent area on the image by locating intentionally induced fringes created by off-axis superposition of a smooth reference wave and an object wave coming from a rough or diffusing sample through an optical system with limited aperture.

A model for the propagation of the light through the optical system has been developed. It takes into account the broadened emission spectrum of the light source, as well as the statistical speckle effect induced by the illumination of a rough surface with partially coherent light. Simulated results have been carefully compared with measurements, both in the spatial domain and in the Fourier domain (spatial frequencies response), which has permitted to better understand the processes involved in the creation of the interference fringes, and improve the design of the device.

Different filters have been investigated in order to extract the depth information from acquired interferograms. By using Gabor filterbanks, which do not need any *a priori* knowledge of the signal, selectivity of the extracted signal has been enhanced by a factor of 1.3 compared to a simple local Fourier spectrum evaluation, and time of the extraction procedure divided by 6, even when compared to fast iterative calculation in the Fourier spectrum. Moreover, by imposing the frequency and/or orientation of the signal to detect, which can be known by a simple calibration procedure, it has been proved that the selectivity can be further enhanced by a factor of 2.5, keeping the calculation time as short or even shorter.

A compact prototype has been designed and built, with a specific multiple fibers arrangement for illumination. The system is separated in two parts: the first one is directly attached to the rigid endoscope, and contains imaging as well as recombining object/reference wave optics, and the detector. It fits into a box with overall dimensions of $115 \times 83 \times 94$ mm. The second part contains the laser source, the scanning arm and the injection optics for the fibered system. It is designed to be left on a small cart. This device can potentially be brought to the bedside, and used during routine endoscopic check-up.

Associated with the device, a complete framework has been elaborated in order to simplify the acquisition procedure as well as the signal processing. This results in a fully automated environment taking in charge hardware control, data storage and signal processing, up to the tri-dimensional scene rendering.

Keywords: Low coherence, single shot, interferometry, endoscopy, contouring, speckle, upper airways.

Acknowledgments

Firstly, I would like to gratefully thank my thesis director, Prof. Christian Depeursinge who gave me the opportunity to join his research group, first as an engineer for a few months after my diploma project, and finally as PhD student. His high quality reflexions helped me all around the way. For sure it was a real pleasure being supervised by someone with such a great scientific knowledge, inside a really motivating atmosphere. I also thank my thesis co-director, Dr. Florian Lang, for its skilled medical point-of-view, always very helpful to head toward realistic solutions.

Thanks to Prof. Pierre Jacquot, Prof. Guy Indebetouw, and Prof. Andreas Ettemeyer for participating in the present work as jury members, as well as to Prof. Olivier Martin for presiding the jury.

I would also like to thank my close colleagues, being still there in the μvision group or not: Florian, for being my diploma assistant and giving me the desire to push further. Jonas, your unrivaled feeling concerning the alignment procedure of the lab setups was really a precious help. My office mate, Nicolas, Etienne and Ata, always there for (not so) short discussions, being science-related, or not: the mood in this room has always been nice. Yann, it was a pleasure collaborating this last year with you, keep your smile, it helps! Good luck to Stéphane for the supervision of the Vector project, and thank you for digging into the administrative hell of salary, so that I could have food in my plate. I wish the best to Olivier for pointing his photons to the right targets. Thanks to Jérome, for all the answers he gave me when I was not so far from becoming mad with Proe, and I hope the DahuShaper community will grow on... Thanks to Daniel, for being such a great master student, you clearly contributed a lot to the finalization of this thesis! My best wishes to all the members of Lyncée Tec: Etienne Cuche, Yves Emery, Nicolas Aspert, Frédéric Montfort, François Marquet, Claude Joris, Eduardo Solanas, with a special thanks to Sébastien Bourquin and Mikhail Botkine for helping me in the design of the prototype. Thanks to Tristan, for introducing me to the pleasure of the LabView wiring, and for taking the time of discussing my software jam.

I would also like to acknowledge the secretaries, Manuelle, Yvette, Doris, and Mme Paulou-Vaucher, always there to give an essential hand with my administrative duties. I thank Alejandro for the IT, Ronald for electronics and Claude as well as the staff of the workshop for mechanics.

Merci à ma famille, pour avoir toujours été là et m'avoir laissé faire mes choix, même lorsqu'ils étaient mauvais. Je remercie spécialement ma soeur, de se soucier de moi quotidiennement. Je te dis également bravo pour ton courage Nadine, tu es une battante, je suis fier de toi.

Last, but probably the most important: I want to sincerely express all my gratitude to Bénédicte, who has always been there on my side to support me. I do know what it costed to you, so I will end up this chapter with a special big word of love for you.

Contents

List of Figures

List of Tables

List of notations

Roman letters

C	Contrast
C_x	Covariance matrix
I	Intensity
L_c	Coherence length
M_t	Transverse magnification
O, R	Object, reference wave
U	Wave
d_o, d_i	Object, image distance
dx	Pixel size or sampling step
f	Focal length
$g(\tau)$	Degree of temporal coherence, normalized autocorrelation function
$h(x)$	Impulse response for linear system (PSF for optical systems)
$\boldsymbol{n}$	Surface normal vector
p_x, p_y	Spatial frequencies

Greek letters

$\Phi(r)$	Radial function
Ψ	Random speckle phase term
Γ	Diffracted field
$\Delta\phi$, $\Delta\varphi$	Phase difference
$\delta(x)$	Dirac function
γ	Smoothing factor
λ	Wavelength
λ_0	Center wavelength
$\Delta\lambda$, $\Delta\nu$	Spectrum bandwidth
ϕ, φ	Phase term
ρ	Radius of curvature
σ	Standard deviation
τ_c	Coherence time
ν_1, ν_2	Eigenvector
λ_1, λ_2	Eigenvalue

Other notations

$\mathscr{F}$	Fourier transform
$\otimes$	Convolution symbol
CAD	Computer Aided Design
CCD	Charged-Coupled Device
CSNE	Cylindrical Shape Normal Estimation
CT	Computed Tomography
DCT	Discrete Cosine Transform
DHI	Digital Holographic Interferometry
DHM	Digital Holographic Microscopy
DS	Delay Stage
DSPI	Digital Speckle Pattern Interferometry
ENT	Ear-Nose-Throat (medical speciality)
ESPI	Electronic Speckle Pattern Interferometry
FD-OCT	Fourier Domain Optical Coherence Tomography
FFT	Fast Fourier Transform
FWHM	Full Width at Half Maximum
LocalFFT	Local Fast Fourier Transform
LCSI	Low Coherence Speckle Interferometry
MRI	Magnetic Resonance Imaging
MTF	Modulation Transfer Function
MVANE	Minimum Variance Axis Normal Estimation
NOHD	Nominal Ocular Hazard Distance
OCT	Optical Coherence Tomography
OPD	Optical Path Difference
OTF	Optical Transfer Function
QF	Quality Factor
PDF	Probability Density Function
PSF	Point Spread Function
RBF	Radial Basis Function
RMSE	Root Mean Square Error
ROI	Region of Interest
SI	Speckle Interferometry
SNR	Signal-to-noise ratio
SPS	Spatial Phase Shifting
TPS	Time Phase Shifting
VBR	Virtual Bronchoscopy

Chapter 1

Introduction

1.1 Medical context and goal of the thesis

In the last 20 years, considerable progress has been achieved in the treatment of benign as well as of malignant laryngeal, tracheal and bronchial stenoses. In airways, endoscopic treatment is mainly used for endoluminal obstructing pathologies, rarely in cases of a deformation of the air channel inherent to a mass situated on the outer side of the bronchial tube. It consists in a laser excision, in a dilatation, in the placement of an endoluminal prosthesis to keep the airway open (stent) or in a combination of these procedures [1]. Stenosis dimensioning is a key predictive factor for the success of endoscopic treatment [2]. Moreover, since the introduction of stents for the treatment of airways stenoses, the accurate evaluation of the diameter of the airways and the evaluation of the length of the stenosis is of utmost importance for correct choice of the prosthesis, especially to prevent the migration of the endoluminal prosthesis. This evaluation is even more important for the placement of self-expanding prosthesis, because the final length of the prosthesis *in situ* depends on the degree of its expansion. Taking into account that the more the evaluation of the stenosis dimensions is performed *right on time* before the surgical intervention, the higher the recovery chances are, this shows that there is a real need for a sufficiently accurate and robust method to achieve quantitative measurements in upper airways. This was the challenging demand of Dr. Lang[1] when he first came by us with these observations. Naturally, if the dimensional measurement could be performed at the same time as the routine endoscopic examination, this would provide the most up-to-date quantification. So the first objective of this thesis was to study and develop a direct measurement system usable in medical environment, and compatible with standard rigid endoscopes commonly used in ear-nose-throat (ENT) medical facilities. While focusing on this main goal, the

---

[1]Service ORL, Centre Hospitalier Universitaire Vaudois (CHUV), Lausanne.

chosen approach shows up as a valuable method for more general macroscopic objects contouring applications, such as in general surgery, or even industrial inspection, whether it requires endoscopic procedure or not.

Classical white light endoscopes have a large depth of field and, most of the time, have a large field of view (typically 60-70°). Images created with these endoscopes are two-dimensional and very distorted. Diverging optics are placed in the objective of the endoscope, they are needed to obtain a large field of view, but this introduces a large barrel aberration. So strictly speaking, a standard rigid endoscope gives a good qualitative image, with extended depth of field, but due to the inherent projective nature of the imaging system, no true-scaling information can be directly deduced. At best an experienced endoscopist can provide an estimation of the size of the stenosis during the exploration of the concerned zone.
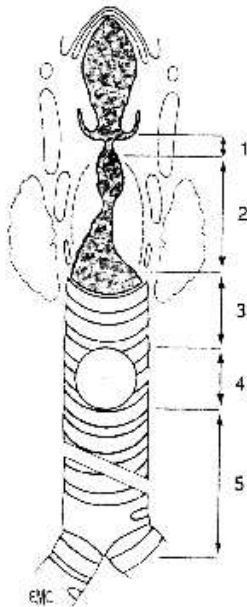
Figure 1.1: Abacus for pre-operative assessment of the dimensions of a benign subglottic stenosis.

Commonly used procedure is to assess the length and the localization of the stenosis with endoscopes of different sizes and lengths and with an intubation laryngoscope. Landmarks are placed with a pencil on the scope and then measured and documented on a specially prepared scheme. This method of manual measurement is relatively accurate for benign stenoses in the larynx and in the trachea ($\pm$ 3 mm). But it is time consuming and dependant on the experience of the endoscopist. Moreover, it is more difficult to use and less accurate in case of malignant stenoses that tend to bleed in contact with the telescope as well as in the main bronchi, where a similar procedure is done through a rigid bronchoscope.

Measurement (or imaging) techniques providing quantitative dimensioning in the case of human upper-airways investigation can be broadly classified in two categories: direct and indirect techniques. Indirect techniques, such as radiology, computed tomography (CT), virtual bronchoscopy (VBS) and magnetic resonance imaging (MRI) provide accurate results and are most of the time non-invasive. The drawback is that they are very expensive, time consuming and more importantly cannot be performed at bedside just before or after an operation.

On the other hand, direct measurement techniques can be used to achieve diagnosis in upper-airways. Although these methods are a bit more invasive, they are far less expensive, require less infrastructures and can be performed right on time and place. They are performed with rigid endoscopes, fibroscopes, and with specifically designed probes, as with the Optical Coherence Tomography (OCT) method [3; 4], and more recently, the Fourier Domain Optical Coherence Tomography (FD-OCT) [5; 6], which surpasses the classical OCT in term of both speed and signal-to-noise ratio. Yelin *et al.* showed that methods based on spectrally encoded recording offer great potential in term of miniaturization, sensitivity and imaging speed for endoscopic applications [7]. Zara and Lingley-Papadopoulos recently publish an article about endoscopic OCT approaches for cancer diagnosis [8].

There is a large panel of techniques available for optical 3D measurements for rough macroscopic objects with a sub-millimeter accuracy [9]. Incoherent light can be used with fringes projection techniques, where a fringe pattern is projected on the surface to measure. Moiré pattern techniques also exist, in which two gratings are used to generate contour fringes [10; 11]. Although in these two cases laser light can be used, and that moiré technique is commonly referenced in the literature as "moiré interferometry", the periodic pattern is generated before the light reaches the sample, and the depth information is obtained by considering the changes in the image of the fringes, so strictly speaking, they cannot be regarded as interferometric measurements. Photogrammetry employing mainly stereo vision procedures to obtain 3D shape are also available [12]. Extended depth-of-field methods can also be used with incoherent white light, for example methods using wavelets to construct a 3D image from a stack of defocused images have been proposed by Forster *et al.* [13]. Mitic investigated the use of a continuously moving structured illumination pattern for microscopic imaging, and achieved sectioning and real-time imaging with the help of a smart pixel detector [14].

Besides these methods using white light, another way of retrieving the depth information is to rely on an interferometric measurement. To achieve interferometric measurement, coherent or partially coherent light must be used. With coherent light comes the question of the speckle pattern. The next section start with a short description of this phenomenon and is followed by a review of macroscopic contouring technologies using laser light.

1.2   Basic principles and current trends

The speckle pattern
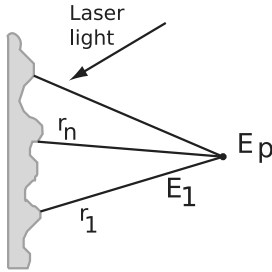
Figure 1.2: Speckle phenomenon.

When coherent light is used to illuminate a rough surface, the scattered field is composed of speckle grains: the mutual interference of the wavefronts creates a complicated interference pattern, with statistical properties. Indeed, each points of the object can be considered as a point source. Thus, the field in a point in space is composed of the coherent addition of every wavelet emanating from the rough object. Due to surface roughness, there is a phase difference between all these wavelets, and the field for a given point in space is given by:

$$E_p(x, y, z) = \sum_n \frac{A_n}{r_n} exp(ikr_n).$$ (1.1)

Assuming that the amplitude and phase of each contribution are independent between them and that the surface roughness is large compared to the wavelength, Goodman [15; 16] derived the probability density function for the real and imaginary parts of the field. And hence, the probability density function for the intensity:

$$p(I) = \begin{cases} \frac{1}{\langle I \rangle} e^{-\frac{I}{\langle I \rangle}} & , I \geqslant 0; \\ 0 & , \text{otherwise}, \end{cases}$$ (1.2a)

and the phase:

$$p(\theta) = \begin{cases} \frac{1}{2\pi} & , \theta \in [-\pi, \pi]; \\ 0 & , \text{otherwise}. \end{cases}$$ (1.2b)

Special care has to be taken to distinguish between "objective" and "subjective" speckle. If a detector is placed anywhere in space within the scattered field without using a lens, an objective speckle pattern is acquired. This pattern only depends on the wavelength of the light, the size of the laser beam which illuminates the surface, and the distance between the scattering surface and the sensor position (i. e.: $s = \lambda z/L$, with λ the wavelength, z the distance between the scattering surface and the observation plane, and L the width of the illuminated area). On the other side, a subjective speckle pattern is obtained when laserlight has been scattered off a rough surface, and that an imaging system is used to collect this field. In this case the mean size of the grains is inversely proportional to the aperture of the imaging system. An intuitive explanation is that the

imaging optic limits the contributions in the image field to wavelets coming from angles that are accepted by the lens.

Holography

Holographic interferometry allows to reconstruct the amplitude and the phase of a wavefront transmitted through or reflected by a specimen. In classical holography, the interference between an object beam (O) and a reference beam (R) is recorded on a photographic plate. If $I_H(x, y)$ is the intensity recorded on the holographic plate, the diffracted field obtained when re-illuminating the developed hologram with a wave U is,

$$\Gamma(x, y) = U I_H(x, y) = U I_R + U I_O + U R^* O + U R O^* \tag{1.3}$$

$U R^* O$ and $U R O^*$ corresponds to a virtual image located at the initial position of the object and to the real image located on the other side of the hologram, respectively. If the holographic plate is re-illuminated with an exact replica of the reference wave R used for recording, the virtual image is then an exact replica of the object wave, multiplied by the reference intensity.

In digital holographic interferometry (DHI), a digital camera is used to record the hologram. Then, instead of illuminating a physical hologram with a replica of the reference wave, all the process is done numerically, thus giving access to quantitative phase and amplitude of the object field [17]. This technique is specially well developed for microscopic imaging, where the magnified defocused image of the sample observed through a microscope objective is recorded. To get rid of the zero order term and of the virtual image term, it is either possible to record the hologram in an off-axis configuration [18], or to use phase shifting [19]. When using an off-axis setup, the zero order and virtual image terms can be discarded by filtering in the spatial frequency domain, the drawback is that the different terms have to be well separated in the Fourier space, which somehow limits the space available for the object spatial frequencies. On the other hand, single shot acquisition is possible. When using phase-shifting inline digital holography, the reconstructed image is free from zero order and virtual image terms, but multiple acquisitions are needed and thus live recording is hardly possible.

Early attempt of an endoscopic application of holography with silver halide holographic plates has been achieved by Smigielski *et al.* [20]. Concerning endoscopic applications of digital holography, Coquoz investigated the application of digital holography with a multicore optical fiber for *in-situ* imaging [21]. Schedin *et al.* published an extensive comparative study of different endoscopes that can be used for pulsed digital holographic Interferometry (pulsed DHI) [22]. Pedrini *et al.* used pulsed DHI with a fibered endo-

scope [23]. Endoscopic pulsed digital holography with 3 different object illumination was recently achieved by Anaya *et al.* [24; 25], they presented measurements on a metallic cylinder excited at 2.18 kHz. With a miniaturization effort, Kolenovic *et al.* achieved endoscopic digital holography by placing the reference beam and the detector inside the endoscopic sensor body [26]. Massatsch investigated the use of digital holography with a low coherence light source in order to achieve vision in turbid media and application to biomedical imaging [27].

Speckle Interferometry

Contouring of macroscopic objects can be obtained with Speckle Interferometry (SI) if using a photographic plate for recording, or Electronic Speckle Pattern Interferometry (ESPI) [28; 29; 30] if using a camera, also usually called Digital Speckle Pattern Interferometry (DSPI) when a digital camera is used. The basic principle is to form correlation fringes when imaging a rough or diffusing sample placed in an interferometer. This can be done in order to observe either changes in shape between two states of the same object, or to obtain direct shape measurement. Recently, Jacquot publied a review of the principal methods based on speckle interferometry in use for experimental mechanics applications [31]. By correctly choosing the optical design of the interferometer, the setup can be made sensitive to either in-plane or out-of-plane changes as well as to the displacement gradient (shear measurement, see Ref. [32] for an extensive review), fig. 1.3 shows basic optical design for each case. Fig. 1.3b shows the basic principle of a shear measurement, in which a tilted version of the field back-scattered by object under study is superposed to an inline one, a thus provide a setup sensitive to the slope change of the object. Fig. 1.3c shows a possible implementation of an in plane displacement measurement setup, with a symmetric illumination, providing a sensitivity vector perpendicular to the z-axis. Fig. 1.3d is another implementation of an in-plane measurement, with reduced sensitivity, which can be useful in case of a setup subject to vibrations, or when a larger depth of field is needed. The formation of the correlation fringes is due to the fact that individual image-plane speckle intensities cyclically vary with respect to the object motion. When a deformation of the object occurs, or if the object is moved, the speckle intensity will vary, and correlation fringes can be observed by either addition or substraction. These correlation fringes encode for the depth information.

Considering a basic Michelson interferometer design, with the mirrors being replaced by two non-specular surfaces, one of them being the observed surface, the interference $I_{tot}(x, y)$ of the wavefronts scattered by these two non-specular surfaces is given by,

$$I_t(x, y) = I_1 + I_2 + 2\sqrt{I_1 I_2} \cos(\Psi_1 - \Psi_2) \tag{1.4}$$
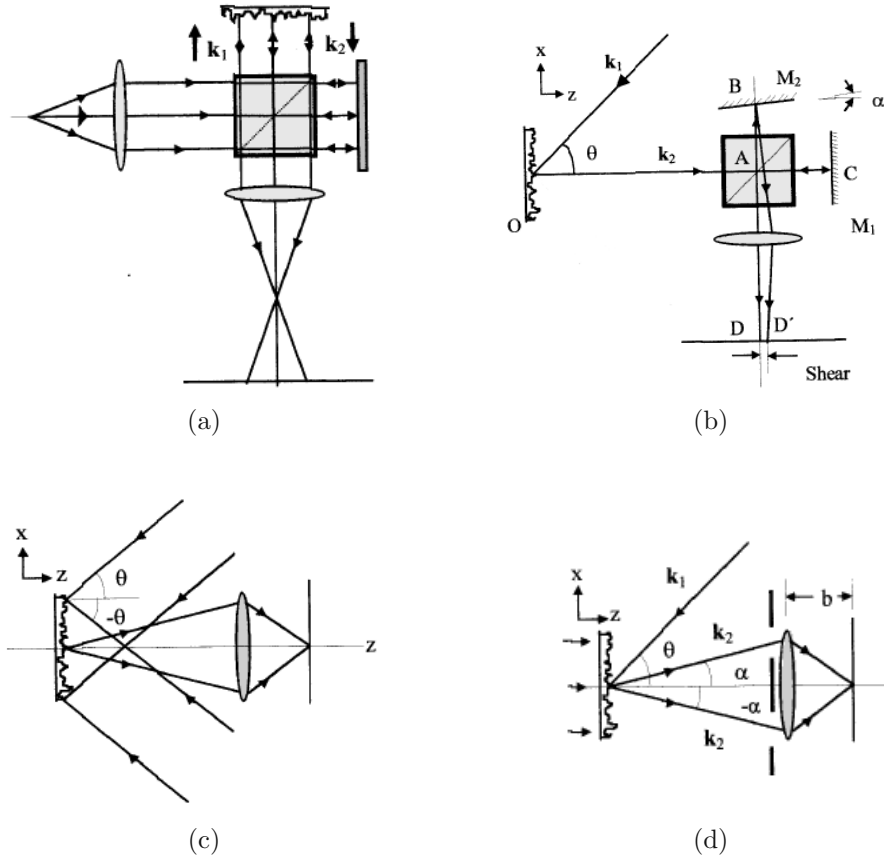
Figure 1.3: Different optical arrangements for SI and ESPI. (a) out-of-plane displacements measurements, with correlation fringes observed in the image plane. (b) shear measurement. (c) in-plane displacements measurement. (d) another configuration for in-plane displacements measurement using a double-aperture arrangement, and providing reduced sensitivity, compared to 1.3c. Schematics are taken from [30].

Where $I_{1,2}$ are the intensities of the wavefronts and $\Psi_{1,2}$ the randomly varying phase of the individual image plane speckles. The displacement of the observed surface by a distance d_1 in the direction of the surface normal will result in a phase change of $\Delta\phi = 4\pi d_1/\lambda$, and the intensity will become,

$$I_t'(x, y) = I_1 + I_2 + 2\sqrt{I_1 I_2} \cos\left(\Psi_1 - \Psi_2 + \Delta\phi\right) \tag{1.5}$$

Correlation is maximum when $I_t = I_t'$. Correlation fringes can be observed if the interferograms corresponding to the two different states of the object are acquired during the same acquisition time of the camera. If single shot measurement is not required, it is also possible to simply record the two interferograms sequentially, and compute $|I_t - I_t'|$.

In order to measure the effective shape of the surface, and not only deformations, two wavelengths techniques can be applied. Actually, if two smooth in-line wavefronts of

different wavelengths are used as references, $\Delta\phi = 4\pi\Delta d\cos\theta\left(\lambda_1 - \lambda_2\right)/\lambda_1\lambda_2$, where Δd is the normal distance between the smooth reference wavefronts and the object wavefronts, and $\cos\theta$ is the angle of incidence of the illumination wavefront. Thus correlation fringes occur at intervals of,

$$\Delta d = \frac{\lambda_1\lambda_2}{2\left(\lambda_1 - \lambda_2\right)\cos\theta} \tag{1.6}$$

Jaisingh and Chiang obtained surface of a regular light bulb [33], using a setup with double exposure. Joenathan *et al.* have used a setup containing a Fourier-filtering part to extract the information from a specklegram [34]. Rodriguez *et al.* have used a fibered setup for out-of-plane sensitive ESPI [35]. Velasquez Prieto and Garcia-Sucerquia reported contouring of macroscopic object with a phase-difference method [36].

As mentioned above, one way to access tri-dimensional measurement is to achieve phase change by using at least two wavelength[37], or a source emitting an extended spectrum, which gives rise to what Takeda and Yamamoto called the Fourier-transform speckle profilometry [38]. Two-wavelength methods were also applied using a dye-laser and an acousto-optic modulator [39]. Considering the time phase-shifting approach, several acquisitions are needed to achieve reasonable reliability, and phase retrieval algorithms specifically adapted to ESPI are reported in literature[40; 41; 42; 43]. Another possible method for phase extraction from a specklegram is to use spatial phase shifting (SPS), in which the phase of a pixel is estimated from the intensity of the surrounding pixels, instead of the values of the same pixel at different times [44; 45; 46; 47]. Kemper *et al.* reported a study on the optimization of SPS for endoscopic ESPI [48].

To combine endoscopic vision and depth information retrieval, attempts were made to use pulsed ESPI, reporting measurements on porcine stomach [49]. Matham extensively described the theoretical formulation, regarding speckle fringes formation in case of the deformation analysis of curved surfaces in a fibered setup with two illumination beams [50].

Coherence gating sectioning and profiling

The interference of two waves coming from a light source with finite temporal coherence length can be expressed as (see [51], chapter 10):

$$I = I_1 + I_2 + 2\left(I_1 I_2\right)^{1/2} g\left(\Delta r\right)\cos\left(k_0\Delta r\right), \tag{1.7}$$

where $k_0 = 2\pi/\lambda_0$, with λ_0 the central wavelength of the emission spectrum of the light source, and Δr is the optical path difference (OPD) for a point considered on the interferogram. g is the coherence function, its width is inversely proportional to the bandwidth

of the emission spectrum, and it has the effect of attenuating the visibility of the interference term with respect to the time delay between the two interfering waves, providing a so-called "coherence gating" effect. In such low coherence interferometry configurations, extracting g on an interferogram is an efficient way of achieving an optical sectioning or profiling. In this case the depth resolution is directly determined by the coherence length of the source.

The already mentioned OCT method is based on this concept, an extensive review of the available OCT techniques is beyond the scope of this thesis, huge amount of literature in this field of interest exists, a starting point for the interested reader could be references [4; 8; 52]. When using a broadband light source in a typical out-of-plane sensitive ESPI interferometer, the process of extracting the location of the coherent superposition of two waves is referenced in the literature as the "coherence radar" technique. Dresel *et al.* used a simple Michelson configuration identical to the one presented on fig. 1.3a, with a piezo-electric actuator to take three phase-stepped acquisitions in order to extract a contour depth [53]. It is also possible to use short light pulses, in this case the method is called "light-in-flight holography" [54]. Carlsson *et al.* further modified the technique using a blazed grating to introduce a spatially varying delay across the reference beam profile [55; 56]. Balboa *et al.* reported 3D measurements using superluminescent diodes and multimodes laser diodes in a fibered interferometer [57], using a five step algorithm for fringe amplitude extraction.

Low coherence interferometry is quite well known in microscopy to achieve optical sectioning, and in this case is also called coherence probe microscopy [58; 59; 60; 61; 62]. It has to be mentioned that, as opposed to the other methods described in this paragraph, here the information encoded in the phase is effectively evaluated, and the short coherence length is used to filter out-of-focus signal. Oh *et al.* adapted this technique to endoscopy to achieve high resolution endoscopic imaging [63]. Another possibility is to acquire several phase stepped images on the same sensor [64]. Recently, Hrebesh *et al.* proposed a system for the record of three phase-stepped interferograms and a reference image at the same time, allowing single-shot low-coherence time-domain profilometry [65].

In DHI and ESPI, the sensitivity can be varied from fraction of micrometers up to several millimeters, using the two wavelength techniques with a suitable choice of wavelength interval. In this approach, the phase difference is computed from two interferograms at two different wavelengths. Indeed, the synthetic beat wavelength created with a two-wavelengths approach is given by $\lambda_s = \lambda_1 \lambda_2 / (\lambda_1 - \lambda_2)$ [66]. This shows that the smaller the difference between the two wavelengths, the larger the synthetic wavelength will be. As an example, when using the green lasing line (543.4 nm) and the usual red lasing line (632.8 nm) of an He-Ne laser, a synthetic wavelength of 3.8 μm is obtained. Anyway, in

order to use DHI for contouring of macroscopic objects, one must ensure that the depth to be observed is smaller than the depth of field of the imaging optic. If very "deep" objects are observed, the aperture of the imaging lens must be low, in order to have a long depth of field. But then it may comes that the observed slope induces fringes equal to the speckle size, in such a case contouring fringes could not be obtained and the depth signal would vanish. For ESPI, the same restriction applies in order to ensure speckle correlation between two acquired states and thus observe correlation fringes. This shows that it is not always possible to observe a whole object in one view, and moreover, that these techniques provide good results when the specimen under observation is quite shallow, which is not the case for human upper airways.

Compared to DHI or ESPI, coherence radar and light-in-flight holography techniques are based on the detection of the envelope of the interference signal rather than the phase itself, and thus are less sensitive to phase fluctuations. The counterpart is that they often require scanning, and therefore are less adequate for applications where fast imaging is required, unless very fast scanning design can be achieved. Most of the time, several acquisitions are taken to extract the fringes amplitude of the speckle interferogram. Another solution is to use rather complicated optical systems in order to either record multiple acquisitions on the same detector, or use multiple cameras on the same setup. In this case single shot profiling is possible, but fine alignment procedure are needed and very good images registrations with sub-pixel performances have to be implemented [67].

Another keypoint is that with the different ESPI and DHI techniques, mostly wrapped phase differences are measured, and not absolute distances. With a coherence gating approach, an absolute measurement is intrinsically obtained, providing that a simple calibration procedure has been applied in order to relate motor positions to sample coordinates. Moreover, the depth resolution is directly given by the coherence length of the laser source, which gives a lot of flexibility for our macroscopic application, where a resolution of a few tenth of millimeter is sufficient. By getting rid of the multiple acquisitions per contour lines, a coherence gating technique can potentially be used to dynamically acquire and observe contour depth on living material, and this for a wide field of view. Fig. A.1 (appendix A) is an attempt to classify the different methods enumerated in this chapter in order to give to the reader a "quick look" at the numerous possibilities to achieve optical 3D contouring, along with some key features.

1.3 Structure of the dissertation

The main content of this thesis is included in the chapters 2 to 4, each chapter has its own introductory section, which recall the main contents specific to the chapter. Chapter 5 gives a global conclusion with a discussion about the perspectives.

Chapter 2 presents the method used to achieve 3D profiling, discussion of differences between our method and the so-called "coherence radar" technique is presented. The simulation of the system is carefully described, and simulated results are compared to measurements.

The chapter 3 is focused on the filtering process involved to provide contouring of the specimen, different filters were implemented and compared. A procedure has been developed to remove non-significant output points remaining after filtering. Finally, 3D visualization of the measured surface has been achieved by the use of radial basis functions.

Chapter 4 covers the modification of the basic interferometer described in chapter 2 with the introduction of a rigid endoscope as imaging system. Section 4.3 is dedicated to the description of the optical design of standard rigid endoscopes, while section 4.4 is dedicated to the presentation of the constructed prototype. It contains a comparison of two fibered designs used to illuminate the sample, one using diverging optics at the tip of the fiber to enlarge the illuminated area, the other one using multiple fibers for illumination.

In appendix B, results of absorption and diffusion coefficients measurements on pig bronchus samples are presented. Appendix C contains snapshots of the constructed prototype. Appendix D presents the evaluation of the hazards that can be potentially encountered during the use of the prototype. An application note on the software development associated with the device can be found in appendix E.

Before going on with the next chapter, the interested reader will find hereafter a first implementation of the so-called *coherence radar* method that has been investigated as a possible solution for the endoscopic application.

1.4 Time domain interferometry: the phase shifting approach

Eq. 1.7 expresses the ability of a wave to interfere with a time delayed version of itself. The coherence time (τ_c) is a characterization of this ability. For a delay time between two interferring waves below τ_c, an interference with a contrast larger than 0.5 can be observed. The coherence time is observed on the autocorrelation signal of the laser source, which can either be obtained with a direct measurement with an interferometer, or through the

calculation of the inverse Fourier transform of the emission spectrum of the source. A quite simple but handy approximation is that for a light source of a bandwidth of $\Delta\nu$, the visibility of the fringes for two waves delayed by $\tau_c \approx 1/\Delta\nu$ is reduced to fifty percent. The path that light has travelled during τ_c is called the coherence length (L_c). Therefore, the interference term will be present only for points on the image for which the optical path difference (OPD) between R and O is below L_c (in eq. 1.7, when $\Delta r < L_c$).

To achieve phase shifting measurements, the mirror (M) depicted on fig. 1.4b is moved with a piezo actuator (PA). This way, fine phase adjustment of the reference is possible. The contrast of the speckle pattern on the image is modified by the reference wave only when there is coherent addition of the two waves. In other words, between 2 phase-shifted images, speckle grains contrast is modified only for points in the image for which the optical path difference between the object and the reference wave is smaller than the coherence length of the laser source. Fig. 1.4a presents the typical signal that is obtained if the intensity of a specific point is recorded while the object or the reference arm mirror is continuously moved along the optical axis.
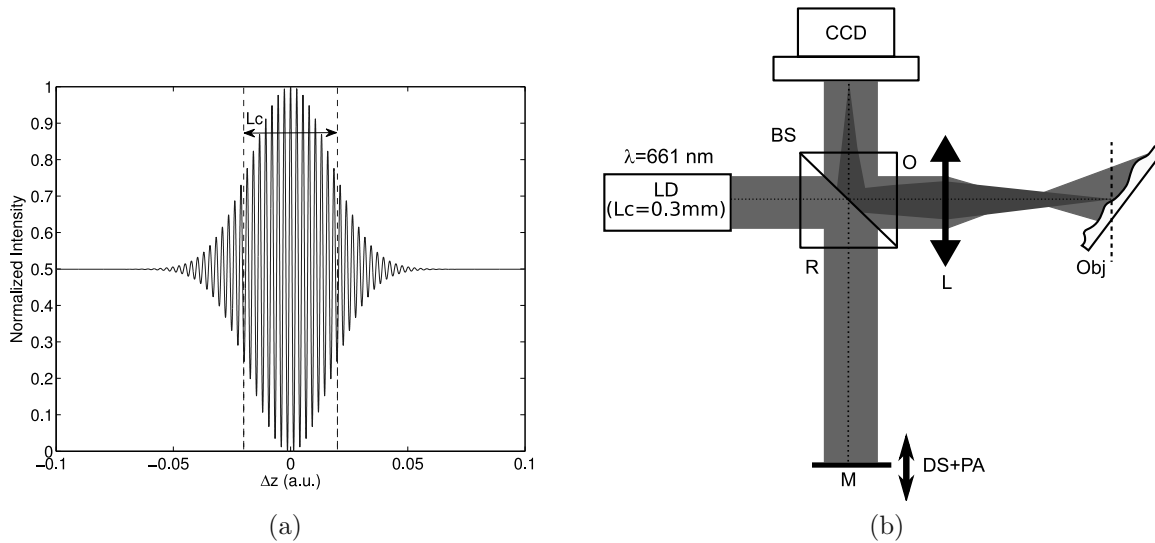
Figure 1.4: (a) typical correlogram with a reduced coherence source. (b) Low coherence inline interferometer. LD: low-coherence laser source. BS: beam splitter. L: lens. CCD: camera. M: mirror. DS: delays stage. PA: piezo actuator. O: object arm. R: reference arm.

Detection of this depth signal is equivalent to detecting the envelope of the acquired correlogram. As an example, if between two acquisitions the phase of the reference wave is shifted by π using the PA, then a simple substraction of the two acquisitions will extract the location of maximum correlation, giving access to the depth information. However, there will always be differences between two speckled images acquisitions, due to CCD noise and vibrations. Thus it is impossible to guarantee that a phase shift of π will occur

for every speckle grains. For this reason, 5 images are acquired with the phase of the reference wave shifted by steps of $2\pi/5$. One obvious way to evaluate the envelope of the correlogram is to calculate a time varying contrast map based on the 5 acquisitions: for each pixels in the stack of acquired images, only the maximum and minimum value are kept, then the contrast map is calculated as:

$$C_{map} = \frac{max(I_{ij}^{1:5}) - min(I_{ij}^{1:5})}{max(I_{ij}^{1:5}) + min(I_{ij}^{1:5})},$$

(1.8)

where $I_{ij}^{1:5}$ represents the value of the pixel ij through the 5 images. A drawback of eq. 1.8 is that for weak signals, the numerator and the denominator tends to be small, and thus C_{map} tends to take undetermined values, which spuriously promotes these noisy signals. This could potentially happen if the considered pixel corresponds to a place where the sample is highly absorbing, or to a place where there is no illumination and "shadowing" occurs. Dresel *et al.* proposed a more reliable method to extract the envelope of the correlogram [53]:

$$A\left(z\right) = \left[\sum_{i}^{N} \left(I_i - \overline{I}\right)^2\right]^{1/2},$$
$$\overline{I} = \frac{1}{N}\sum_{i}^{N} I_i.$$

(1.9)

Indeed, pixels that are situated in a region where there is coherent superposition will have a much greater standard deviation, while pixel that outside this region will have a null standard deviation. This prevents eq. 1.9 from inadequately highlighting weak signals. As a sidenote, it has to be mentioned that the depth signal can also be obtained by calculating the magnitude of the cross-interference term with the well known 5-images phase-shifting algorithm, such as for example the one described in [68]. It has been observed that compared to eq. 1.9, the use of such a phase shifting algorithm does not bring better results and need more complex calculations.

Fig 1.4 presents the results obtained on a surrogate of bronchial tree made of silicon and doped with Al_2O_3 which reproduces the optical characteristics of the biological tissues [69]. Fig. 1.5a is one of the five acquisitions needed for the procedure, fig. 1.5b is the contrast map obtained with eq. 1.8, fig. 1.5c is the contrast map after thresholding. Notice the unwanted remaining pixels in the border of the image. Fig. 1.5d is the result obtained after using eq. 1.9, as it can be seen, after thresholding (fig. 1.5e), there is no remaining pixels but the ones corresponding to the maximum of the envelope of the correlogram.

This method has the advantage of computational simplicity, and is rather independent

(a)

(b)   (c)   (d)   (e)
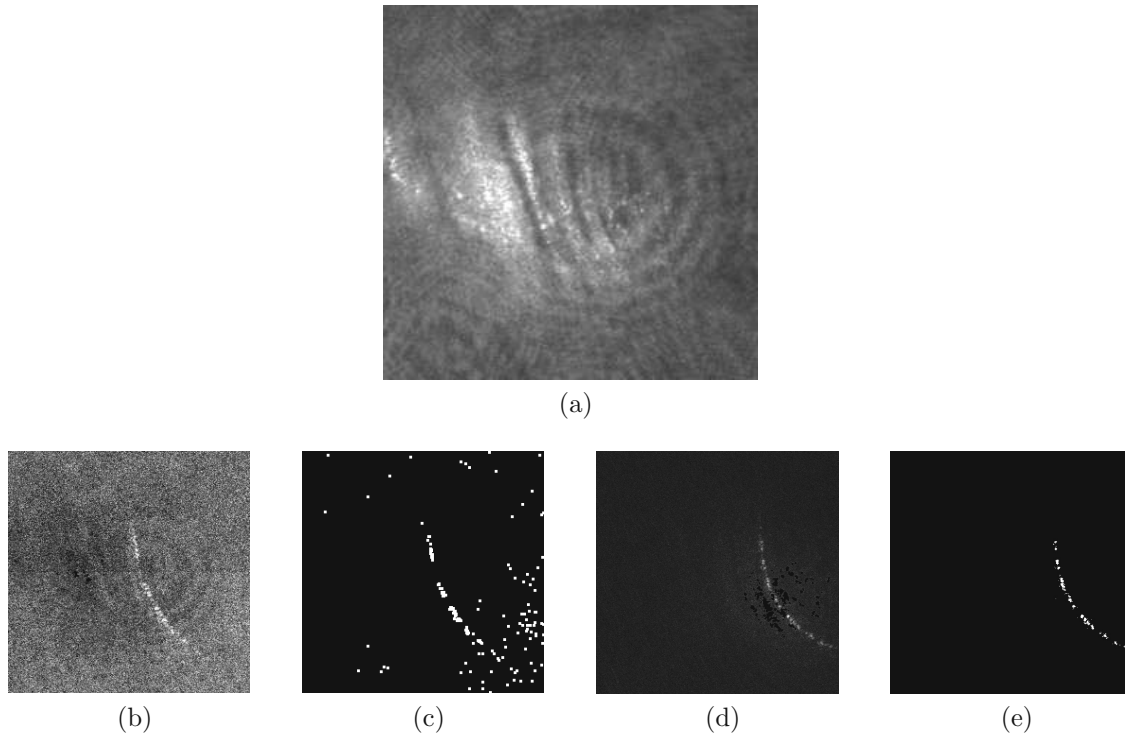
Figure 1.5: Time phase shifting detection: (a) 1 of the 5 acquisitions, (b) calculated contrast map (eq. 1.8), (c) thresholded contrast map, (d) correlogram envelop detection calculated with eq. 1.9, (e) thresholded correlogram envelop.

of the speckle size. The lateral resolution is defined by the aperture size, which in turn also defines the speckle size. So it can be stated that for this method, the best configuration is when the aperture allows for fully developed speckle on one pixel. Although this phase shifting method is quite robust for retrieving the depth signal, it requires moving the object or the delay stage with very fine steps. Thus, it cannot be regarded as a realistic solution for a system that should work in a highly noisy environment such as the surgical room. The approach developed further in this thesis requires only one acquisition per contour level. In this sense it was shown to be a more realistic approach and it potentially places the technique in direct concurrence with long range OCT [3], when the latter is used for topological inspection of biological cavities.

Chapter 2

Low-coherence interferometry single shot contouring

2.1 Introduction

Interferometric measurements are widely used to obtain contouring of macroscopic objects, in particular the Electronic Speckle Pattern Interferometry technique (ESPI). Jaisingh and Chiang obtained surface of a regular light bulb [33], using a setup with double exposure. Joenathan *et al.* used a setup containing a Fourier-filtering part to extract the information from a specklegram [34]. Rodriguez-Vera *et al.* have used a fibered setup for out-of-plane sensitive ESPI [35]. Velasquez Prieto and Garcia-Sucerquia reported contouring of macroscopic object with a phase-difference method [36]. All these techniques require at least a double exposure procedure by either changing the object position or reference path length, inducing or acquiring object deformation, or using multiple wavelengths. To enhance reliability, usually algorithms using more than 2 phase shifted interferograms (typically 4 or 5) are used [43; 68]. Balboa *et al.* reported 3D measurements using superluminescent diode and multimodes laser diodes in a fibered interferometer [57], using a five step algorithm for fringe amplitude extraction. One way to access tri-dimensional measurement is to achieve phase change by using at least two wavelength, as Tatam *et al.* reported [37], or a source emitting an extended spectrum [38]. Another possible method for phase extraction from a specklegram is to use spatial phase shifting (SPS), in which the phase of a pixel is estimated from the intensity of the surrounding pixels, instead of the values of the same pixel at different times, as it is the case for time phase shifting. Bhaduri *et al.* achieved SPS with the use of a double aperture mask [43; 45]. In order to overcome the limitation of multiple acquisitions, many efforts were done to build interferometers allowing to record multiple interferograms at the same time. Recently, Hrebesh *et al.* proposed a system for the record of three phase-stepped interferograms

and a reference image at the same time, allowing single-shot low-coherence time-domain profilometry [65].

Contouring by extracting the location of the coherent superposition of two waves is possible by using short light pulses, with the so-called light-in-flight holography technique [55]. When using a continuum of light with an extended spectrum instead of pulsed light, the method is called coherence radar [53; 70].

Here the idea is to use a novel arrangement for low-coherence interferometry. Similarly to the coherence radar technique, the goal is to achieve contouring by isolating the zone on the acquired image where coherent superposition of the reference and object waves occurs. Fringes are intentionally created using a well chosen off-axis arrangement with an imaging system with limited aperture, and the correlation signal between the two waves is evaluated by extracting the location of these fringes, thus providing a depth signal. It will be shown that it is possible to achieve contour extraction in only one acquisition, providing a realistic configuration for measurement in rude environment or on dynamic samples, and much better suited for endoscopic applications.

First, the optical arrangement and the procedure used for fringes extraction are carefully described. The performance of the optical system has been totally simulated, taking into account the broadened emission spectrum of the light source, as well as the statistical speckle effect induced by the illumination of a rough surface with partially coherent light. Results of the simulation are compared with measurements, they show good agreement. Finally, several measurements are presented, amongst them one was realized on a tilted plane and used for technique validation and precision evaluation.

2.2   Setup

Curve level extraction is achieved with the use of the smooth reference wave speckle iterferometer depicted on fig. 2.1. The source is a low-coherence laser-diode (LD), with a coherence length of about 0.3 mm. A beam splitter (BS1) separates the collimated beam generated by LD into the reference beam (R) and the object beam (O). The reference beam is directed to a delay stage (DS), composed of two mirrors (M1 and M2) mounted on a motorized axis. A lens (L1) is placed in the object arm of the interferometer. It is used to widen the illuminated area of the object and to form an image at the CCD plane. The adjustable diaphragm (D) is an essential part of the setup: indeed, it is used to limit the aperture of the system, thus allowing to create interferences composed of fringes modulated by a slow varying speckle pattern. L2 is used to adapt the spherical reference wave in order to match the illumination geometry.

Extracting on the image the positions where these interference fringes are situated
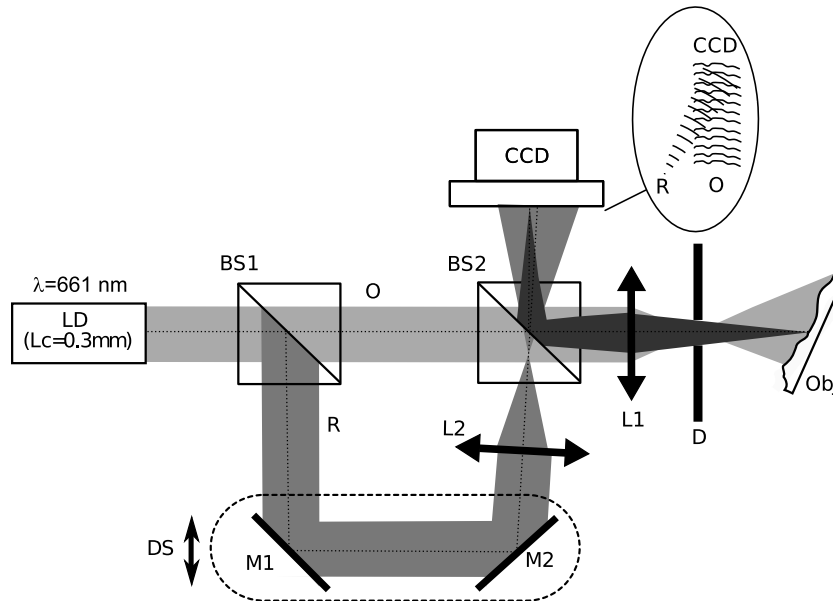
Figure 2.1: Experimental smooth reference wave speckle iterferometer. LD: laser-diode with low coherence length. BS1, BS2: beam splitters. L1, L2: Lenses. D: adjustable diaphragm. Obj: Scattering sample. DS: delay stage. CCD: charge-coupled device camera.

provides a depth signal for macroscopic object (with height much greater than L_c), and an easy contouring procedure by either shifting R or O. On the setup depicted on fig. 2.1, the DS is used first to adjust the length of the reference arm in order to match the length of the object arm, then the DS can be used to scan the object for different curve levels.

M2 is placed so that there is an angle between the optical axis of R and O. This creates "carrier fringes" on the interferogram. In the Fourier spectrum, this separates the interference terms and the zero-order term. Detecting the presence of these fringes becomes then possible and provides a simple but efficient way of extracting the area on the image where coherent superposition of the two waves occurs, thus extracting a curve level in only one acquisition. In this chapter a filtering procedure using a local calculation of the Fourier spectrum corresponding to the signal composed of the neighborhood of the processed pixel is exposed. In chapter 3 other possible filters will be presented in order to extract the fringes location.

2.2.1 Contour lines extraction

As pointed out in the previous subsection, it is possible to create fringes that are discernable with a small mismatch between the optical axis of R and O. Let us take the example of a plane wave propagating along an axis forming an angle θ with respect to the normal of the detector plane, and an object wave. The interference between these two waves can

be expressed as:

$$I = I_R + I_O(x, y) + \sqrt{I_R} \exp(-ik \sin \theta x) O + \sqrt{I_R} \exp(ik \sin \theta x) O^*, \qquad (2.1)$$

where I_R is the intensity of the plane reference wave, I_O is the intensity of the object wave, and O is the complex field backscattered by the object. Taking the Fourier transform of eq. 2.1 gives:

$$\mathscr{F}\{I\}(p_x, p_y) =$$
$$\mathscr{F}\{I_R + I_O\}(p_x, p_y) + \mathscr{F}\left\{\sqrt{I_R}O\right\}(p_x + p_0, p_y) + \mathscr{F}\left\{\sqrt{I_R}O^*\right\}(p_x - p_0, p_y), \qquad (2.2)$$

with p_x, p_y the spatial frequencies and $p_0 = \sin\theta/\lambda$. Eq. 2.2 shows that in off-axis configuration the two interference terms are centered around $\pm p_0$. In our case, a local evaluation of the signal energy enclosed in a bandwidth around these two frequencies provides a mean to discriminate between coherent and incoherent area on the acquired image.

The interferogram is processed with a sliding window filter, defined by evaluating the Fast Fourier Transform (FFT) over a neighborhood. Practically, good results are obtained with a window filter size of 8×8 pixels, allowing a trade-off between computational complexity and sampling of the different spatial frequencies. The output value of the pixel (p, q) that is processed is then the maximum value of the local spectrum components, after zero-order removal:

$$y(p, q) = \max_{m,n \in [1, N-1]} |h_{m,n}| \quad \text{,where:}$$
$$h_{m,n} = \sum_{k=0}^{N-1}\sum_{l=0}^{N-1} x(p+k, q+l) e^{-i(mw_0(p+k)+nw_0(q+l))} \quad \text{,with:} \qquad (2.3)$$
$$p, q \in [0, M-1]$$

Eq. 2.3 corresponds to a local measurement of the high frequencies contribution, with $x(p, q)$ the input interferogram, w_0 the slowest signal pulsation considered, $h_{m,n}$ the window filter and $y(p, q)$ the filter output value. It is also possible to evaluate the mean value or the cumulative sum in a certain bandwidth of spatial frequencies. It was observed that taking as output the maximum value is sufficiently selective, providing that there is no sinusoidal variation of the intensity induced by the object itself that falls into the frequency calculated by the FFT. This is due to the coarse sampling of the local FFT calculation.

Indeed, if the Fourier Transform window is calculated on a greater number of frequency components, more than one pixel will have a high value, and in this case, one better has to output the sum of the cumulative energy in a given bandwidth.
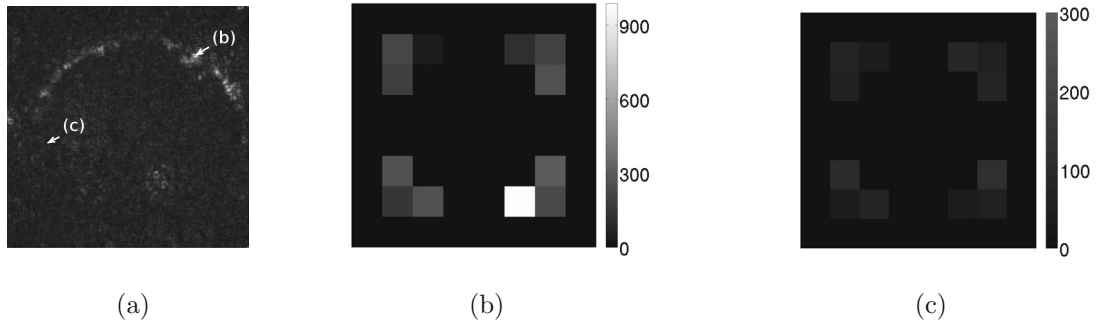

(a)   (b)   (c)

Figure 2.2: (a) extracted signal using the "local FFT" principle on a metallic cylinder with a source with $L_c = 0.3$ mm. (b) and (c) are the amplitude of the Fourier spectrum calculated in a neighborhood of 8×8 pixel around the pixel marked with an arrow on (a) (after zero-order removal) for a pixel inside and outside the curve to be detected, respectively.

Fig. 2.2a shows the obtained signal for the extraction of a meridian on a metallic cylinder. Fig. 2.2b and 2.2c shows the different components of the FFT (after zero-order removal) calculated over a neighborhood of 8×8 pixels, when the pixel of interest belongs to an area where OPD is smaller than L_c and greater than L_c, respectively. Notice the drastically different scales on the graylevel colorbars.

The extraction in the Fourier domain is made possible because of the small aperture of the optical system, which is needed in order to have a slow varying speckle pattern, preventing the fringes to be drowned under high frequency speckles. This aspect will be assessed through simulation in the next section.

2.3 Simulations

The imaging part of the optical system of fig. 2.1, consisting of the imaging lens L1 and the diaphragm D are approximated by a thin lens and a small aperture, as it can be seen on fig. 2.3.

Given an optical field $U_0(x', y')$ in the object plane, the optical field in front of the aperture $Up(x, y)$ can be easily calculated with:

$$U_p(x,y) = \frac{1}{i\lambda d_o} e^{\frac{i2\pi d_o}{\lambda}} \iint U_0(x',y') e^{-i\pi \frac{(x-x')^2+(y-y')^2}{\lambda d_o}} dx' dy'. \tag{2.4}$$

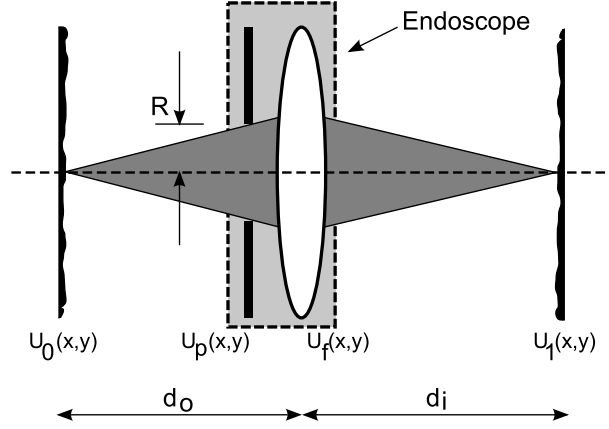Eq. 2.4 is the convolution formulation of the free space propagation in the Fresnel

Figure 2.3: Simulation of the imaging part of the setup on fig. 2.1. d_o and d_i: object-lens and lens-image distances, respectively. R: radius of the diaphragm used to limit the aperture of the optical system. U_0: input object optical field, U_p: field after propagation over a distance d_0 (before the diaphragm), U_f: field after the diaphragm/lens system, U_1: image field on the CCD plane (propagation over a distance d_i).

approximation. Formulated in the spatial frequencies domain it becomes:

$$U_p(x,y) = \frac{1}{i\lambda d_o} e^{\frac{i2\pi d_o}{\lambda}} \mathscr{F}^{-1} \left\{ \mathscr{F}\left\{U_0(x,y)\right\} \cdot e^{-i\pi\lambda d_o \left(p_x^2 + p_y^2\right)} \right\}(x,y), \qquad (2.5)$$

where $\mathscr{F}$ represents the Fourier transform operation, and (p_x, p_y) are the spatial frequencies.

Discrete formulation of eq. 2.5 for numerical implementation is expressed as [71]:

$$U_p(m,n) = \frac{1}{i\lambda d_o} e^{\frac{i2\pi d_o}{\lambda}} FFT^{-1} \left\{ FFT\left\{U_0(m,n)\right\} \cdot e^{-i\pi\lambda d_o \left(p_k^2 + p_l^2\right)} \right\}_{m,n}, \qquad (2.6)$$

where $p_k = k/(N\Delta x)$, $p_l = l/(N\Delta y)$. N is the number of sampling points along one dimension, Δx and Δy are the sampling steps for directions x and y. It is important to denote that in the convolution formalism, the sampling steps are the same for the input plane and the output plane.

The influence of the small aperture can be easily calculated by the multiplication, in the spatial frequencies domain, of the field after propagation with a circular function. Thus, the field right after the aperture becomes [51]:

$$U_p'(x,y) = \mathscr{F}^{-1} \left\{ \mathscr{F}\left\{U_p\right\} \left(\frac{x}{\lambda d_o}, \frac{y}{\lambda d_o}\right) \cdot circ\left(\frac{R}{\lambda d_o}\right) \right\}(x,y), \qquad (2.7)$$

where $circ(R/\lambda d_o)$ has value 1 when $x^2 + y^2 < R^2$ and 0 elsewhere. The lens bends the field $U_p'(x,y)$ with a quadratic phase term. The field $U_f(x,y)$ is calculated with the thin

lens formula, with f the focal length of L1 on fig. 2.1:

$$U_f(x,y) = U_p'(x,y) \cdot e^{\frac{i2\pi}{\lambda}\frac{1}{2f}\left(x^2+y^2\right)}. \tag{2.8}$$

The field $U_1(x,y)$ is then obtained by propagating the field $U_f(x,y)$ using eq. 2.5 remplacing d_o by d_i. The distances d_o and d_i are chosen so that the CCD plane corresponds to the image plane, thus satisfying the condition $1/d_o + 1/d_i = 1/f$.

Considering a coherent light backscattered by a rough surface, the field on a point in space can be seen as the sum of all the contributions of the illuminated points:

$$A(x,y,z) = \frac{1}{\sqrt{N}} \sum |a_k| \exp(i\phi_k), \tag{2.9}$$

where N is the number of illuminated points considered, in our case the sampled values of the input field used in the simulation. a_k and ϕ_k are the amplitude and the phase of the kth contribution, respectively. Taking the assumption that the amplitude and phase of each contribution are independent between them, and that the roughness of the object is greater than the wavelength, it follows that the different phases contributions ϕ_k are uniformly distributed on $[0, 2\pi]$ [15; 16].

Based on these considerations, the speckle pattern induced by the illumination of the object was simulated by adding a random phase term uniformly distributed on $[0, 2\pi]$ to the field $U_0(x,y)$, on the object plane. It has to be noted that if the roughness of the sample is below a wavelength, or if the number of scatterers is small, the assumption of an uniformly distributed speckle phase probability does not stand anymore. For a random phase term in the object below π (which means a roughness below half the wavelength), the speckle phase probability tends to be confined in a narrow distribution with a Gaussian form [72]. Let us also mention here the model developed by Equis and Jacquot, in which they also study the second order statistics of the numerical speckle field [73].

The statistic of the intensity of the simulated speckle pattern in the acquisition plane in the absence of spatial integration of the detector is compared with eq. 1.2b, result is presented on fig. 2.4. Crossmarks are the probability density function (PDF) values obtained from the histogram of a simulated image with an input field with constant amplitude and a random phase, through an optical system with f=5 cm, object and image plane are placed so that the transverse magnification is unitary ($d_o = d_i = 10$ cm), the aperture diameter is 0.6 mm. Plain curve is the probability density function calculated with eq. 1.2b. Measurement on the simulated interferogram are in close agreement with analytical formulation, which proves that the introduction of a random phase term in the input field is a realistic process to simulate the speckle induced by the backscattered field. This term could be modified in order to account for different roughness or diffusing

properties, for example if the roughness of the surface is smaller than the wavelength, the possible range of value for the random distribution could be modified accordingly.
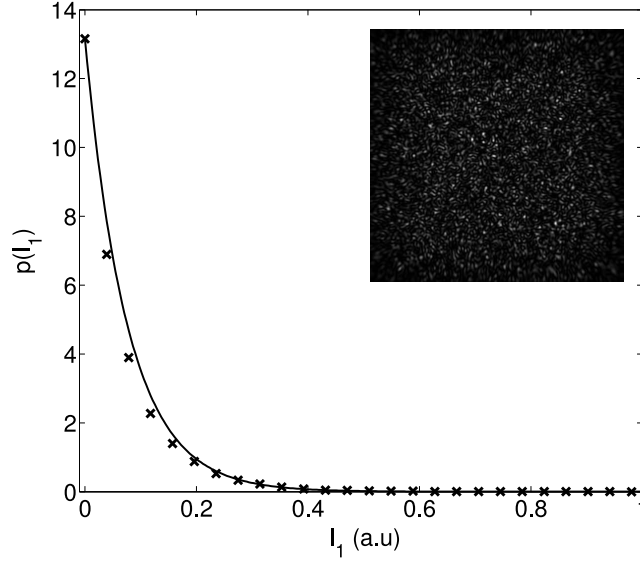

Figure 2.4: Probability distribution function (PDF) of the speckle intensity in the image plane. Crosses: measurement on the simulated interferogram, curves: PDF calculated using eq. 1.2b. Inset: simulated speckle pattern at the CCD plane.

The speckle size is a key factor, for if the speckle size is of the same size than the fringes periodicity that we want to detect, the extracted meridian will be highly noisy, as it will be demonstrated further. For an optical system, the speckle size is a value derived from the statistic of the field that can be approximate by (see [74], chapter 6):

$$s \approx 1.2 \left(1 + \frac{d_i}{d_o} \right) \frac{\lambda f}{D}, \tag{2.10}$$

where $D = 2R$ is the diameter of the aperture. Indeed, the speckle size is inversely proportional to the aperture size. This imposes an upper limit on the aperture of the optical system, and thus a limit on the lateral resolution. That means in turn that the missmatch between the optical axis of R and O, and the diameter of the diaphragm have to be chosen so that the fringes can be resolved, and at the same time that the mean speckle size is sufficiently large in order to achieve good meridian extraction.

On the CCD plane, the object wave $U_1(x, y)$ interfere with a spherical reference wave $U_r(x, y)$, with (x_0, y_0, z_0) the origin of the spherical reference wave, described by:

$$U_r(x, y) = \frac{1}{\rho(x, y)} e^{\frac{-i2\pi}{\lambda} \rho(x,y)}$$

$$\rho(x, y) = \sqrt{(x - x_0)^2 + (y - y_0)^2 + z_0^2}. \tag{2.11}$$

All the formalism above is developed using only a scalar value for wavelength, and thus a pure monochromatic light. The laser diode used in the setup described in fig. 2.1 has typically an emission spectrum of a width of 1.5 nm, the interference pattern due to the superposition of R and O is thus partially coherent. The intensity resulting from the interference of the two partially coherent waves is calculated with:

$$I(x, y) = |U_1(x, y)|^2 + |U_r(x, y)|^2$$
$$+ 2 |U_1(x, y)| \cdot |U_r(x, y)| \cdot |g_{1r}(x, y)| \cdot \cos(\Delta\varphi), \quad (2.12)$$

where $\Delta\varphi = arg\{U_1(x, y)\} - arg\{U_r(x, y)\}$ and g_{1r} is the complex degree of temporal coherence between the object and the reference waves, also called the normalized autocorrelation function. To simulate the effect of the reduced coherence, knowledge of the width of the emission spectrum is sufficient. $|g_{1r}|$ is approximated by a gaussian function with $FWHM = L_c$:

$$|g_{1r}(x, y)| = e^{-\frac{OPD(x,y)^2}{2\sigma^2}}, \quad (2.13)$$

with $OPD(x, y)$ representing the optical path length difference between U_1 and U_r for a point (x, y) on the CCD plane, and $\sigma = L_c/(2\sqrt{2 \ln 2})$. The coherence length of the source can be deduced from the width of the emission spectrum with the evaluation: $L_c \approx \lambda_0^2/\Delta\lambda$. By introducing the partially coherent nature of the light emitted by the laser diode at the end of the simulation, the speckle pattern is approximated as created by a totally coherent illumination. Nevertheless, errors introduced by this approximation are negligible. Indeed, the optical path difference induced by each scatterer considered as a source of a small spherical wave contributing to the creation of the speckle pattern on the object is considerably smaller than Lc.

Fig. 2.5 shows interferograms obtained from the simulation (left side), along with experimental verification with the setup depicted on fig. 2.1 (right side), each time the Fourier spectrum is presented as inset. Parameters for the simulation are: $\lambda = 661$ nm, $d_o = 7.56$cm, $d_i = 14.75$ cm, $\Delta x = \Delta y = 4$ μm, N=1024, $x_0 = 700$ μm, $y_0 = 200$ μm, $z_0 = 47.35$ mm. Fig. 2.5b and 2.5d were obtained observing a flat lightly diffusing object (a sheet of standard white paper) perpendicular to the optical axis. Amplitude of the input field for the simulation is constant ($|U_0(m, n)| = 1$), and an uniformly distributed random phase term was added to simulate for the roughness of the object. To obtain results on fig. 2.5a and 2.5c, R was set to 0.5 mm and 2.5 mm, respectively. Experimental results on fig. 2.5b and 2.5d were obtained for aperture diameters of about 1 mm and 5 mm, respectively.

As in off-axis holography [18], the introduction of carrier fringes separates the two image terms (R^*O and RO^*) and the zero order term ($|O|^2+|R|^2$) in the Fourier spectrum.
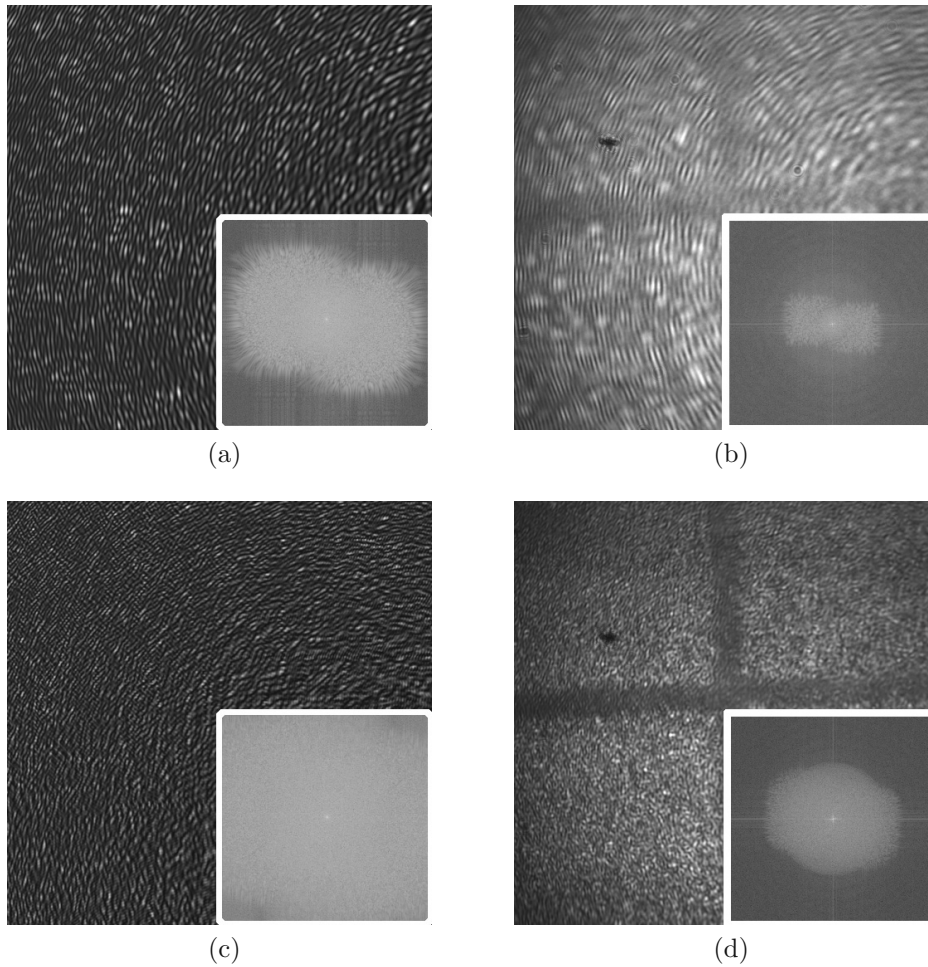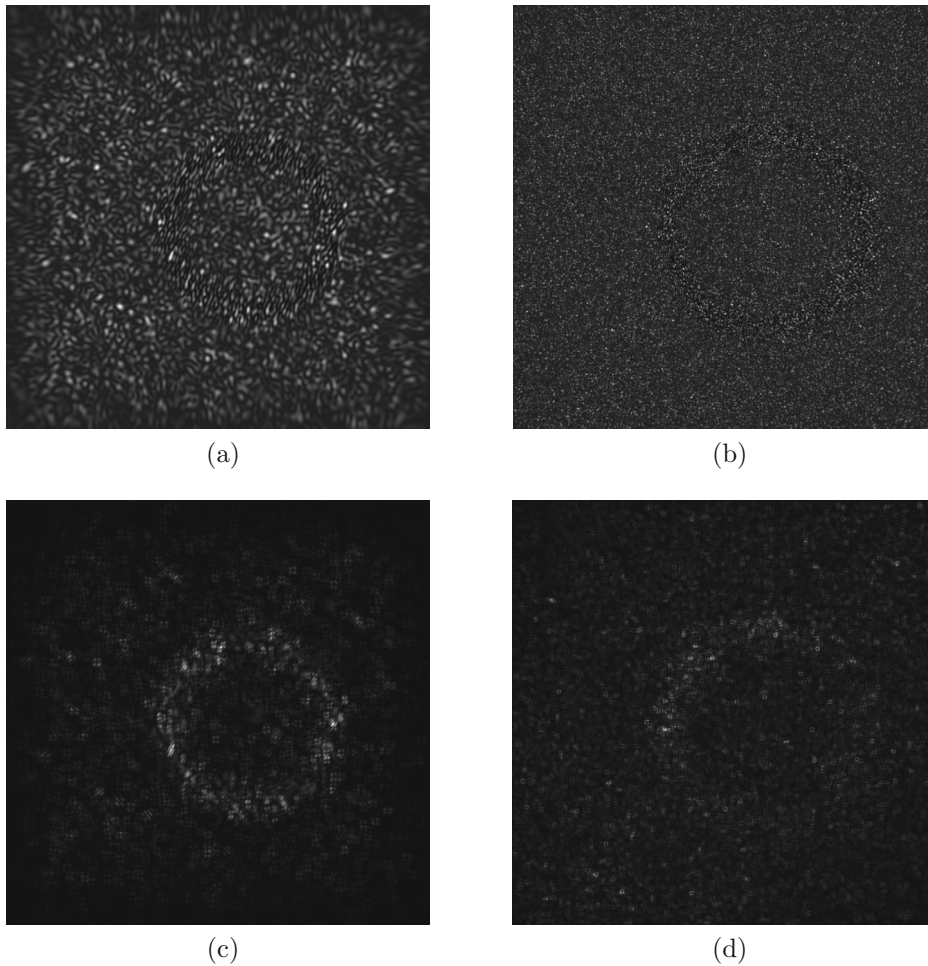
Figure 2.5: (a) simulated interferogram with a diaphragm diameter of 1 mm. (b) Experimental interferogram with a diaphragm diameter of 1 mm. (c) Simulated interferogram with a diaphragm diameter of 5 mm. (d) Experimental interferogram with a diaphragm diameter of 5 mm. Corresponding Fourier spectrum are presented as insets.

Due to the roughness of the sample, there is an almost homogeneous contribution of all the spatial frequencies, up to the cutoff frequency of the optical system, which is in turn determined by the aperture size. A system with a large aperture will create a fine speckle pattern (fig. 2.5c and 2.5d). For plane waves, if the angle between the reference and the object wave is not large enough, the interference terms will then overlap with the zero order term in the Fourier spectrum. For spherical waves, it is the relative distance between the origins of the waves that has to be considered. In such cases it is impossible to detect the fringes on the image and at least two states of the system must be acquired to obtain the depth information, which requires the use of either multiple wavelengths, or time phase shifting techniques. On the other side, due to the inherent discrete nature of the Fast Fourier Transform (FFT), a large aperture might propagate spatial frequencies higher than half the Nyquist frequency, and the spectrum might be squeezed in the border

of the FFT. For spherical waves, for each points on the detector, the angle between the propagation vector of the reference wave and the object wave must be below 3 degrees, this limit is imposed by the pixel size of the CCD to guarantee adequate sampling of the fringes [75].

(a)

(b)

(c)

(d)

Figure 2.6: (a) and (c): Simulated interferogram and extracted signal with short coherence length and diaphragm diameter of 0.6 mm. (b) and (d): Simulated interferogram and extracted signal with short coherence length and diaphragm diameter of 3 mm.

On real signals, most often there is not a high contrast difference between the zone where there is coherent superposition of the object and reference wave, and the incoherent area of the signal. Fig. 2.6a and 2.6b present simulated interferograms obtained with the same parameters as those used to obtain fig. 2.5a and fig. 2.5c, except that the coherence length was shorten down to 10 μm and that the ratio between the reference and object waves was adapted in order to create low contrasted fringes. Fig. 2.6a and 2.6b were obtained with a simulated optical system having an aperture diameter of 0.6 mm and 3 mm, respectively. On fig. 2.6c and fig. 2.6d are shown the results of the filtering

with the "local FFT" principle. Points on the image for which OPD is below L_c are correctly isolated on fig. 2.6c, but it is not the case on fig. 2.6d. Indeed, the speckle has a high contrast, and it is modulated by the fringe pattern only in the coherent area. This modulation is efficiently filtered only when the relative size of the speckle grains is large enough with respect to the fringe periodicity. This shows the need to find an optimum balance between pupil size (or speckle size), and reference beam angle (or fringe periodicity).

2.3.1   Simulated results

This section gives results examples, with an emphasis on the effect of the roughness of the sample on the Fourier spectrum in the image plane. The input optical field consists of a pure amplitude object, which simulates a plane perpendicular to the optical axis, with reflexion coefficient varying in function of the position (x, y) in this plane. This creates a plane target with vertical and horizontal stripes. A random phase uniformly distributed between 0 and 2π is added to take in account the roughness of the sample and its associated speckle effect.

The center wavelength for simulation is 661 nm, each pixels correspond to 4 μm. The distance between the object plane and the thin lens is 10 cm. Placement and focal length of the thin lens is chosen to obtain a transverse magnification $M_T = 1$, so distance between thin lens and image plane is also 10 cm and equivalent focal length of the imaging system is 5 cm. To obtain the interference pattern, a spherical reference wave with parameters $(x_0, y_0, z_0) = (700\ \mu\text{m}, 700\ \mu\text{m}, 47.35\ \text{mm})$, as described in eq. 2.11, is added to the optical field of the image. To observe the effect of the reduced coherence, L_c is set to 10 μm and the interference pattern is finally obtained following eq. 2.12.

Fig. 2.7 shows the simulated results when there is no speckle pattern (i. e. without adding the random phase term to U_0). The fringes appear as straight lines because the source point of the spherical reference wave is set so that the curvature of its wavefronts in the image plane matches the mean curvature of the image field. The area on the image where coherent supperposition of the reference and object waves occurs is delimited by two circles, corresponding to the points for which $OPD = L_c$. Differences between fig. 2.7a and 2.7b shows, as expected, that a diminution of the aperture size affects the image resolution. Nevertheless, it is always possible to distinguish the interference fringes on the image. This is due to the fact that the carrier frequency corresponding to the fringes is a well defined point in the Fourier spectrum. This point has a high amplitude compared to the rest of the frequencies that form the total spectrum of the image, and thus the filtering completes in both cases, as it can be seen on the insets of fig. 2.7a and 2.7b.

Figure 2.7: Interference pattern without speckle: (a) with aperture diameter of 1 mm, (b) with aperture diameter of 0.4 mm. (c) and (d) Fourier spectrum of respectively (a) and (b).

On the other hand, when the random phase term is added to the input field, and thus that a speckle pattern can be observed, the fringes carrier frequency becomes blurred (see fig. 2.8). This blurring is due to the propagation of the uniformly distributed phase term of the object, which introduces nearly homogeneous spatial frequencies in the spectrum, up to the cutoff frequency of the optical system. Table 2.1 summarizes the considerations highlighted throughout this section.
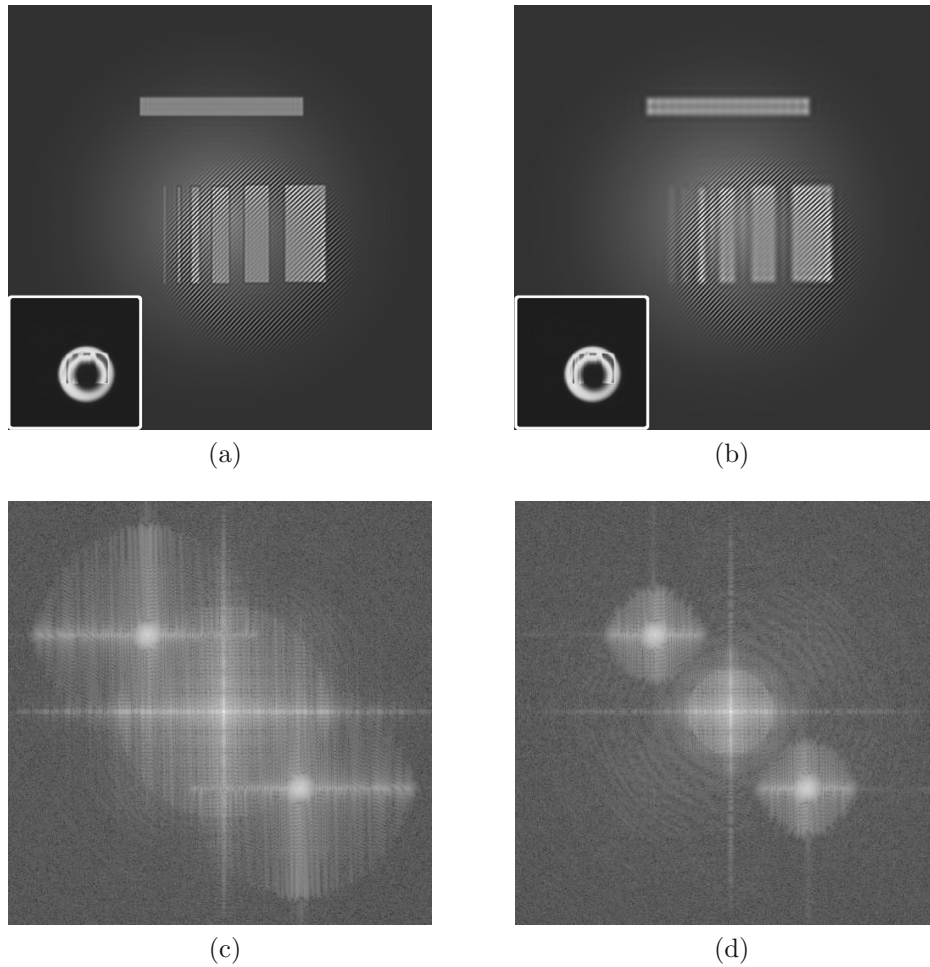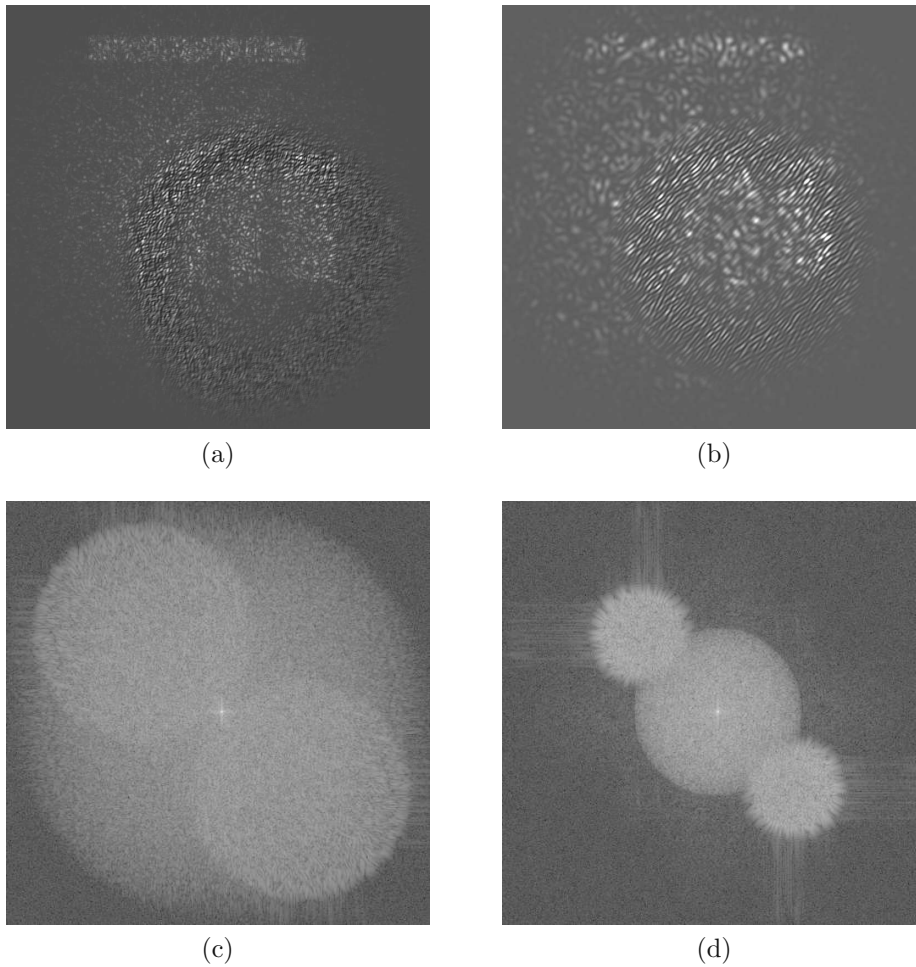
Figure 2.8: Interference pattern with speckle effect: (a) with aperture diameter of 1 mm, (b) with aperture diameter of 0.4 mm. (c) and (d) Fourier spectrum of respectively (a) and (b).

	Specular sample	Scattering sample
Aperture size	Transverse resolution	Transverse resolution
		+ Speckle size
Reference angle	Fringes period	Modulation discernment
Impact on filtering	None	Relative size must match

Table 2.1: Signal detectability considerations.

2.4 Experimental results

First measurement was made on a tilted plane made of standard white paper. Scanning was achieved by translating M1 and M2 mirrors on fig. 2.1, with steps of 1 mm. A threshold was applied on the filtered results. 3D positioning of all the extracted contour lines is

represented on fig. 2.9b. Fig. 2.9a shows a typical interferogram, with a zoom on fringes as inset, along with the results of the filtering as described by eq. 2.3, before thresholding. Measurement has been repeated for different orientations of the tilted plane with respect to the optical axis. Root mean square error (RMSE) between the poi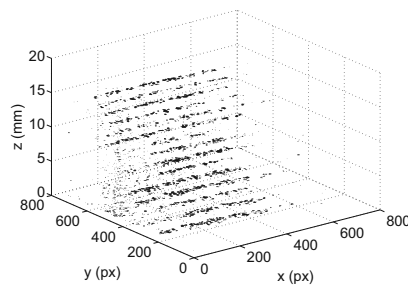nts actually on the plane and the measured coordinates was 0.4 mm. Compared to the coherence length of the source (0.3 mm), which represents the physical limit for the precision of the method, the error introduced by the fringes extraction procedure is acceptable for macroscopic objects contouring.
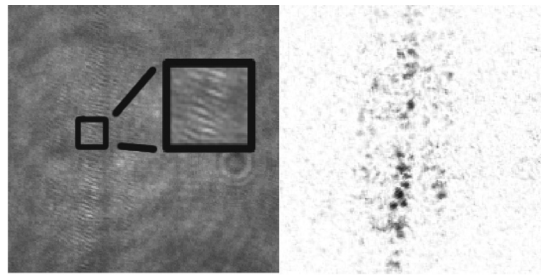

(a)

(b)

Figure 2.9: Tilted plane measurement. (a) Typical signal, zoomed fringes as inset, along with the output of the "LocalFFT" filter before thresholding. (b) 3D view of several extracted level curves.

Example of measurement on the inner side of a 13 mm diameter cylinder made of standard white paper is presented on fig. 2.10. The extracted curves are superimposed to a classical image. To obtain these contours, the DS was translated by 8 mm, which is also the height difference between these two isovalue lines. It has to be noted that, due to the inherent magnification dependence on the z position of the object, the meridians seem to have different diameters. Indeed, the z dependant magnification of the optical system has to be taken into account to obtain true tri-dimensional rendering of the object. An alternative could be to use object space telecentric optics, as they are not affected by object position magnification change.
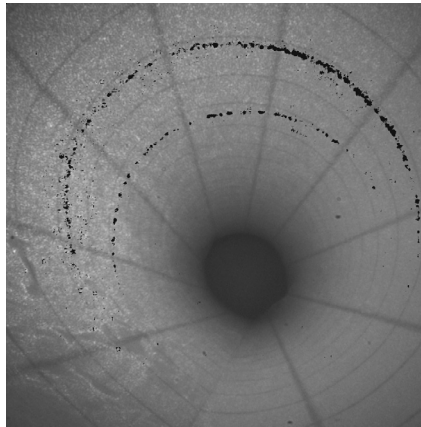
Figure 2.10: 2 level curves (in red) extracted on the inner side of a 13 mm diameter cylinder. Contour lines are separated along the z direction by 8 mm.

Fig. 2.11 presents results obtained on a ceramic statuette of a pig. Fig. 2.11a shows a camera snapshot of the statuette, with the measured area delineated in black. 11877 points were acquired, and the 3D surface was interpolated using 2375 of these points, with the method described in section 3.4. The minimum variance axis normal estimation (hereafter denoted MVANE) method was used for off-surface points creation (see section 3.4.1 for a description), with a radius of 3 mm and a variance threshold of $6 \cdot 10^{-3}$. Off-surface points have been added at a distance of 1.2 mm. γ parameter has been set to 1.5. It is a smoothing factor used during the surface fitting procedure, its impact will be discussed in detail in sect. 3.4. The fitted set of radial basis function has been evaluated on a box of 75×75×75 voxels.

Fig. 2.12 shows the obtained mapped surface when observing the wooden tip of a pencil. 74'633 3D coordinates were acquired, and $1/25th$ of these points were used to map the surface for visualization. The set of radial basis function was again evaluated on a box of 75×75×75 voxels. The blacks dots represent the set of measured points. As it can be seen from results depicted on fig. 2.9−2.12, low coherence off-axis interferometry can be used on a wide variety of samples with different surface properties and geometries.
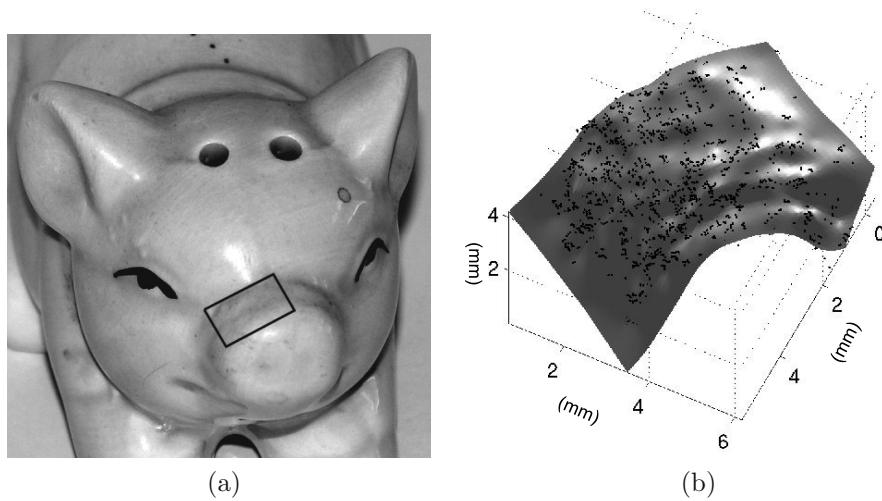
Figure 2.11: (a) Grayscale camera snapshot of the pig ceramic statuette observed, with underlined measured area. (b) Measurement on the delineated snout part, with black dots representing the points used for the surface mapping (1/5 of the total number of acquired points).
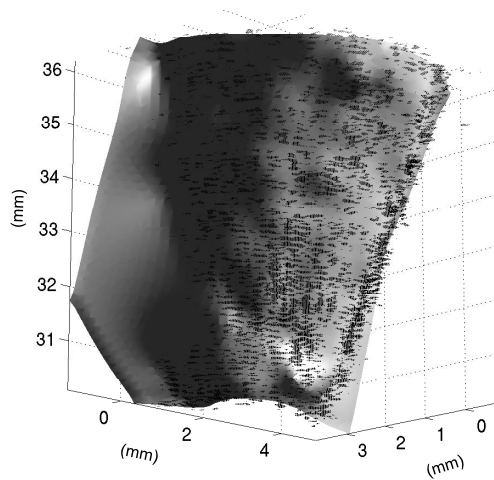
Figure 2.12: Acquisition of 74633 3D points on a pencil tip (black dots). Surface interpolated using 1492 points. MVANE method, radius 3 mm, variance threshold 0.01, distance of off-surface points 0.5 mm, $\gamma = 1$.

2.5   Conclusion

The method used for optical contouring of macroscopic objects has been presented. This system is based on a smooth reference wave speckle iterferometer using short coherence laser diode.

Using an off-axis configuration, it is possible to create a fringe pattern superimposed to the speckle pattern. Locating the position of the fringes has been done with an evaluation of the Fourier spectrum in the neighborhood of the processed pixel, to extract a contour line in only one acquisition. This approach has been shown to be a more realistic approach for endoscopic contouring than the classical coherence radar method, where several acquisitions are needed to extract one contour depth. The technique has been described mathematically and simulated, including the speckle pattern created by the partially coherent illumination of rough or diffusing samples. The importance of the diaphragm size has been clearly highlighted. It has been proved that to achieve robust contour map extraction, a small aperture is needed. This could be a limitation of the technique for application where a high lateral resolution is needed. Simulation results have been presented and compared to observations made with the lab setup. Achieving single shot contour depth extraction offers great potential in terms of measurements on dynamic samples.

Results have been presented on different samples, especially an evaluation of the precision of the method had been achieved by tilting a plane and calculating the RMSE of the measurement. It showed up a precision of 0.4 mm when using a source with a coherence length of 0.3 mm. Moreover, these different measurements showed that the technique can be applied successfully to achieve topography on a wide range of material with different properties, from mainly specular reflective objects (example of the ceramic statuette), to rough surface producing scattering (example of the wooden pencil tip).

Chapter 3

Signal processing

3.1 Introduction

This chapter specifically describes the image processing steps involved in the extraction of the depth signal. An entire section is dedicated to the problem of surface rendering, based on the extracted coordinates, in order to obtain true 3D rendering of the observed topography.

For one acquisition, the goal is to isolate points in the image for which the optical path difference (OPD) between the object and the reference wave is lower than the coherence length of the laser source (L_c), which is defined as the Full Width at Half Maximum (FWHM) of the laser source autocorrelation signal. These points define a contour depth. Roughness of the observed surface and backscattering induce random intensity pattern distribution, known as speckle effect, in the image. The camera records the addition of the object and reference waves. For points in the image satisfying the condition $OPD < L_c$, the image contains a speckle pattern modulated by the interference of the reference and object beams, as there is coherent superposition. On the other hand, for points outside the coherence length, no modulation is observed. This is the principle that was extensively described in chapter 2 to isolate a contour depth. In this chapter a set of filters that are applied on the image in order to detect the fringes are presented. These filters are designed according to a "pattern matching" approach. Typically, window filters representing a set of possible fringes shape are created. The convolution between the window filters and the acquired interferogram then isolates fringes locations, and thus returns the intended depth information. Generally speaking, iso-phase lines due to the interference of two spherical waves have an hyperboloidal shape, and thus the orientation and the periodicity of the fringes cannot be considered as constant over the whole interferogram. These variations have to be taken into account in order to enhance filtering efficiency.

In section 3.2, different filters specifically chosen with regards to the design of the

device are compared in term of sensitivity, specificity and speed. Randen and Husoy provided an extensive comparative study of filters dedicated to texture classification [76]. Based on his classification, discrete-cosine transform filters (DCT filters) and Gabor filterbanks were evaluated with regards to the endoscopic application. In particular the *a priori* knowledge of some features of the fringes to be extracted, such as local orientation of the pattern, was used to create "matched" filters. They appeared to be intrinsically more sensitive and faster, with the drawback that they need a calibration procedure. Then, the nonlinear aspects of the procedure are carefully described. Filters output is not perfect, and in many cases there is a few isolated points that have a high output responses but do not correspond to a point lying in the coherence zone. A reliable procedure to remove these noisy points is extremely important, as they induce erroneous surface mapping during the 3D rendering process.

Section 3.4 concentrates on the interpolation of the data points to obtain a surface mapping of the measurement for visualization. It is a challenging task as the data collected are sparse and non-uniformly sampled. Many different techniques exist to represent 3D surfaces, such as natural neighbor interpolation [77], or with the use of a signed function, where off-surface points are created in order to define a volume function. Particular isovalue of this volume function can then be used to find the desired implicit surface. General approach to surface fitting by a signed function is well described by Hoppe *et al.* [78]. Among these signed functions, Radial Basis Functions (RBF) are commonly used since quite a long time. Carr *et al.* achieved surface interpolation of computed tomography (CT) data with the use of RBF [79]. In case of compactly supported RBF, interpolation with RBF can be approximated by the use of two-scale B-Splines [80; 81]. Nowadays, fast fitting algorithms exist in order to solve the RBF interpolation equations [82; 83; 84; 85; 86]. RBF were proved to be also a good choice for the visualisation of data acquired with our device. Of particular concern is the problem of off-surface points generation, requiring to estimate surface normals. Mitra and Nguyen described a method based on least square estimation [87]. Induced unwanted deformations of the surface representation due to normal estimation is evaluated for two different normals estimation methods.

Processing of signals acquired by the low-coherence endoscopic setup described in chapter 4 mainly consists in 3 steps. First the different signals have to be filtered. Then post-processing jobs are performed in order to obtain a set of tri-dimensional coordinates. Finally, a surface interpolating the set of points is calculated. Fig. 3.1 shows a block diagram of this approach.
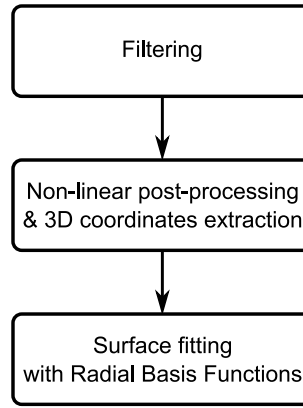
Figure 3.1: Block diagram of the main steps involved in the 3D visualization of the measured points.

3.2 Interference pattern filtering

Investigations were made to perform the detection either in the spatial frequency domain, or in the space domain. In the following, the filters that have been retained are presented and compared.

Local Fourier spectrum estimation (LocalFFT)

In the frequency domain, as described in chapter 2, the detection of the coherent zone is based on the calculation of a local spectrum. A sliding window filter is constituted by calculating the Fast Fourier Transform (FFT) in a neighborhood of N×N pixels in an image of M×M pixels, the retained output value is then the maximum amplitude of the local spectrum, which corresponds to a local measurement of the high frequencies contribution. This method is hereafter denoted as "'Local FFT"', and is defined as:

$$
\begin{aligned}
y\left(p,q\right) &= \max_{m,n\in[1,N-1]} \left|h_{m,n}\right| \quad \text{, where:} \\
h_{m,n} &= \sum_{k=0}^{N-1}\sum_{l=0}^{N-1} x\left(p+k,q+l\right)e^{-i(mw_0(p+k)+nw_0(q+l))} \quad \text{, with:} \\
p,q &\in [0,M-1]\,.
\end{aligned}
\tag{3.1}
$$

In eq. 3.1, it is necessary to compute the 2D formulation of the FFT, which is very time consuming. Thanks to the separability of the FFT, it is possible to calculate the different $h_{m,n}$, corresponding to the frequency components of the transform, first along the rows, and then along the columns. Moreover, an incremental formulation of this filter

is possible, in which the kth value of the filter is calculated with the $(k-1)^{th}$ value. This is possible because the FFT forms a geometrical serie of the form $a(l) = a(0) \cdot q^l$, with $q = e^{-i \cdot w_0 n}$. Eq. 3.2 represents a column-wise (or line-wise) version of an incremental implementation of the filter h defined in eq. 3.1:

$$h_n(k) = (h_n(k-1) - x(k-1)) \cdot e^{i \cdot w_0 n} + x(k+N-1) \cdot e^{-i \cdot w_0 n(N-1)} \qquad (3.2)$$

Discrete cosine transform (DCT) filters

Convolutions based on widely used filter for pattern matching or texture analysis have also been investigated. Mainly, a N×N matrix is defined with a set of basis functions. The filtering process is then achieved by calculating the convolution of this matrix with the input signal [88].

One possible way of defining these basis functions is to calculate a set of N discrete cosine vectors of the form:

$$\boldsymbol{x_n}(k) = \sqrt{\frac{2}{N}} \cos\left(\frac{2\pi n}{2N} \cdot k\right) \quad , \text{with:}$$
$$k, n \in [0, N-1].$$
$$\qquad (3.3)$$

A set of matrix defining a set of N^2 filter masks is created by calculating $H_{k,l} = \boldsymbol{x_k} \cdot \boldsymbol{x_l}^T$ [88]. It has to be noted that these filters do not exhibit a sinusoidal variation (Fig. 3.2a), so strictly speaking they cannot be regarded as optimal choice for fringe patterns extraction. Anyway, as in our case the pattern to detect is a speckle pattern modulated by a fringe pattern, these filters show reasonable results. For N = 4, we get 16 different $H_{k,l}$ matrices. Among these matrices, M (in our case we chose M = 4) of them returning the highest results from our test samples are kept. The output is then the sum of the squared result from the convolution between these matrices and the input signal:

$$I_{out} = \sum_{i=0}^{M-1} (I_{in} \otimes H_i)^2 \quad , \text{where:}$$
$$H_i \in H_{k,l}, \quad k, l \in [0, N-1].$$
$$\qquad (3.4)$$

Fig. 3.2a depicts the window filters obtained with $N = 4$, with the four chosen window filters returning the highest results surrounded by black boxes.

Gabor filterbank

With the idea of adapting the filter to the shape of an interference pattern modulated with a slow varying speckle pattern, another filterbank that has been tested consists of Gabor masks of the form [89]:

$$H\left(\boldsymbol{x}, \sigma, \theta, f\right) = \frac{1}{\sigma^2} \exp\left(\frac{|\boldsymbol{x}|^2}{2\sigma^2}\right) \cdot \exp\left(i2\pi\boldsymbol{f}^T R\left(\theta\right)\boldsymbol{x}\right) \quad, \text{ with:}$$

$$\theta \in [0, \pi],$$

(3.5)

where $R(\theta)$ is the rotation matrix about the angle θ, $\boldsymbol{f} = [f_c \ 0]^T$ is the frequency of the complex sinusoidal variation to detect and σ is the standard deviation of the Gaussian envelope of the filter. This creates a window filter composed of a sinusoidal variation with a Gaussian envelope, and oriented along an axis with an angle θ, which can be seen as an adaptation of the exponential basis functions of the Fourier transform operation. Again, a set of matrices is constructed by calculating eq. 3.5 for different f_c and θ, and the output of the filter is calculated according to eq. 3.4. In practice, the filter length along one dimension of the otherwise infinite response is limited to 2σ and the sampling step $\Delta\theta$ is set to $20°$. Filter H is complex valued, the real part has a cosine variation and the imaginary part a sine modulation: this allows to detect every possible shift of a sinusoidal intensity variation with frequency f_c along the corresponding axis. Fig. 3.2b shows the real part (cosine modulation) of a set of 7 pixels wide Gabor filter masks obtained for nine different orientations θ with constant frequency. As it can be seen, the intensity variation of the pixels of these window filters is very similar to the local intensity distribution of the modulated speckle pattern, thanks to the gaussian envelope of the filter.
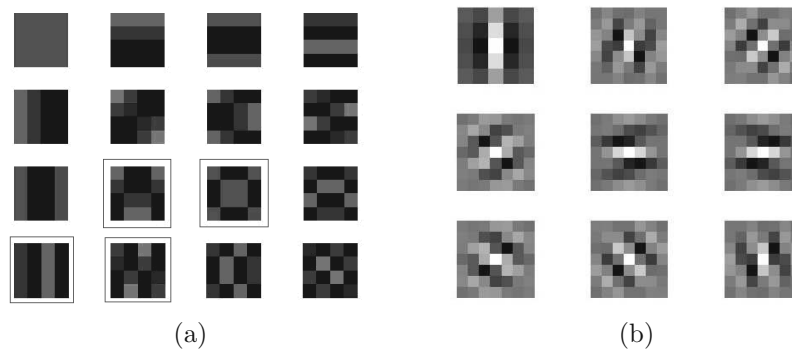

(a)   (b)

Figure 3.2: (a) discrete cosine masks, calculated according to eq. 3.3, box sourrounded masks are the ones returning the highest output and used in eq. 3.4. (b) Example of a set of Gabor filter masks, only the real part of the filter is depicted.

Calibration and "matched" filtering

The set of filters defined with eq. 3.4 did not use any *a priori* knowledge of the local fringe pattern. However, knowledge of either the orientation or the frequency of the fringes to detect can be used to minimize the calculation cost of the procedure. The calibration procedure consists in several acquisitions with a plane perpendicular to the optical axis being shifted between acquisitions, such that we observe interference pattern on the whole image. Based on this measurement, a map matching every pixel to a known frequency f_c and orientation θ is then calculated. In such a case, the filter output for a given pixel is directly determined by the convolution of the input image with eq. 3.5: no need to calculate the sum of the output of several filters with spanned values for f_c and θ, as the values for frequency and orientation returning the highest output are already known, thanks to the calibration procedure. Moreover, the use of a filterbank is not optimum anymore, as each filter contributes with its own noise response. To this, the output of a filter chosen accordingly to a calibration map is smaller for zones without fringes than the output of a filterbank, thus leading to a better signal-to-noise ratio. In the following, these filters are referenced as "matched" filters.

3.2.1   Filtering efficiency

To estimate which filter to chose for a given application, the efficiency of each filter, namely, the local FFT, discrete cosines, Gabor's filters, and their version using a calibration procedure, has been estimated. A typical signal has first been simulated, using the model described in chapter 2, section 2.3 (see Fig. 3.3a, a full description of the whole figure can be found in sec. 3.3).

An intensity variation based on a Poisson noise distribution was then added to this signal, and the different filters were applied. To quantify the filtering efficiency, a quality factor is defined as:

$$QF = \frac{\frac{1}{M} \sum_{k=0}^{M-1} I_{filt_k}^{ROI}}{\frac{1}{L} \sum_{n=0}^{L-1} I_{filt_n}^{\overline{ROI}}}, \tag{3.6}$$

where I_{filt} is the normalized filtered signal. ROI is a region of interest locating the pixels where the contrast of the fringes in the noiseless synthetic image is higher than 0.5. M and L are the number of pixels inside and outside the ROI, respectively. Numerator of QF is the mean intensity value in the region where the fringes are supposed to be, which is an estimator of the strength of the extracted signal. The denominator represents the mean intensity outside this region, and is an estimator of the noise amplitude. Computing of QF was made for different amount of noise, which forms a set of input images with
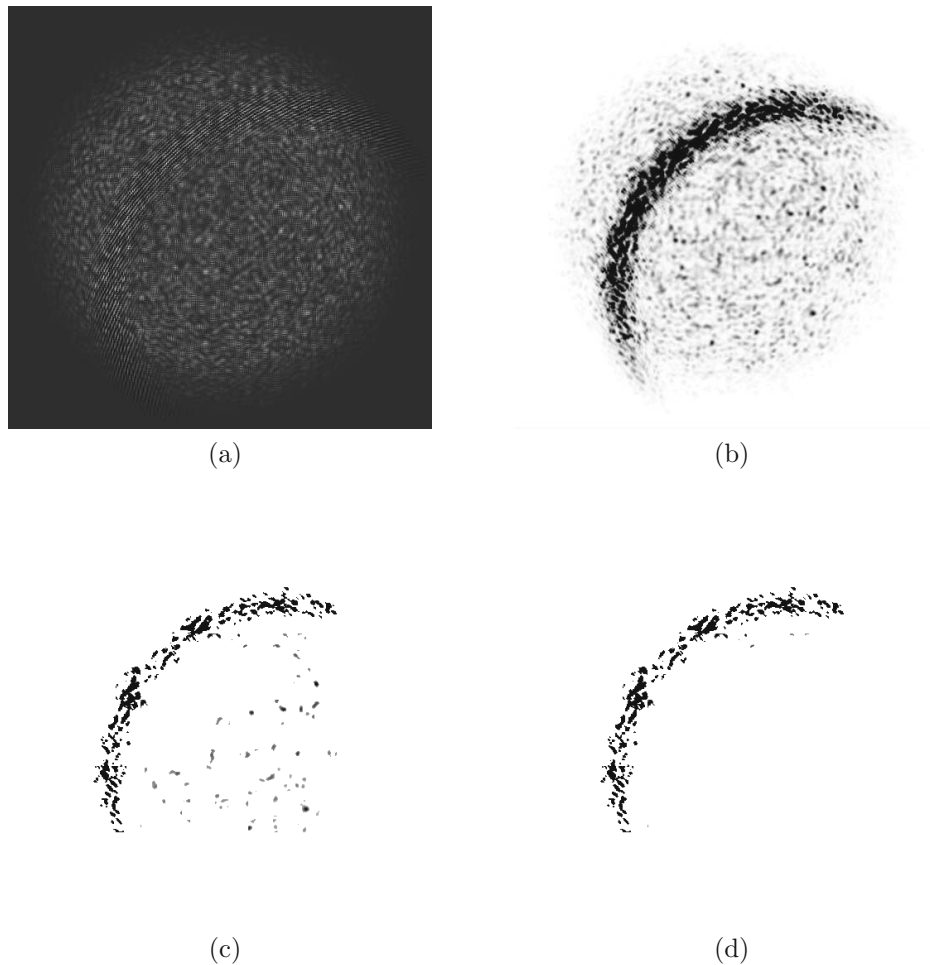
(a)

(b)

(c)

(d)

Figure 3.3: (a) Base signal used for quantifying the efficiency of the different filters. (b) filtering results obtained with a Gabor filterbank. (c) Signal after local thresholding procedure. (d) Pixels finally kept after the non-linear procedure and matched to a known depth.

distinct signal-to-noise ratio (SNR), Fig. 3.4 shows the obtained results. SNR for input images is calculated with $SNR = 10 \cdot \log \left(\sum P_o^2 / \sum (P_n - P_o)^2 \right)$, where P_o and P_n are the pixel values in the simulated interferogram and in the simulated interferogram with a certain amount of Poisson noise, respectively.

Matched Gabor algorithm always performs best in term of extracted signal quality. However, matched Gabor and matched DCT filters need a calibration step. Gabor filterbank comes right after when processing images with SNR higher than 15 dB. When processing images with SNR lower than 15 dB, matched DCT filter is better suited. For images with SNR higher than 30 dB, the local FFT filter outperforms the matched DCT filter, but is still less efficient than the Gabor filterbank. For every filters described here, there is a maximum efficiency that cannot be overtaken, as the QF value tends to saturate for every filters. This can be explained by the speckle pattern, which in turn is a
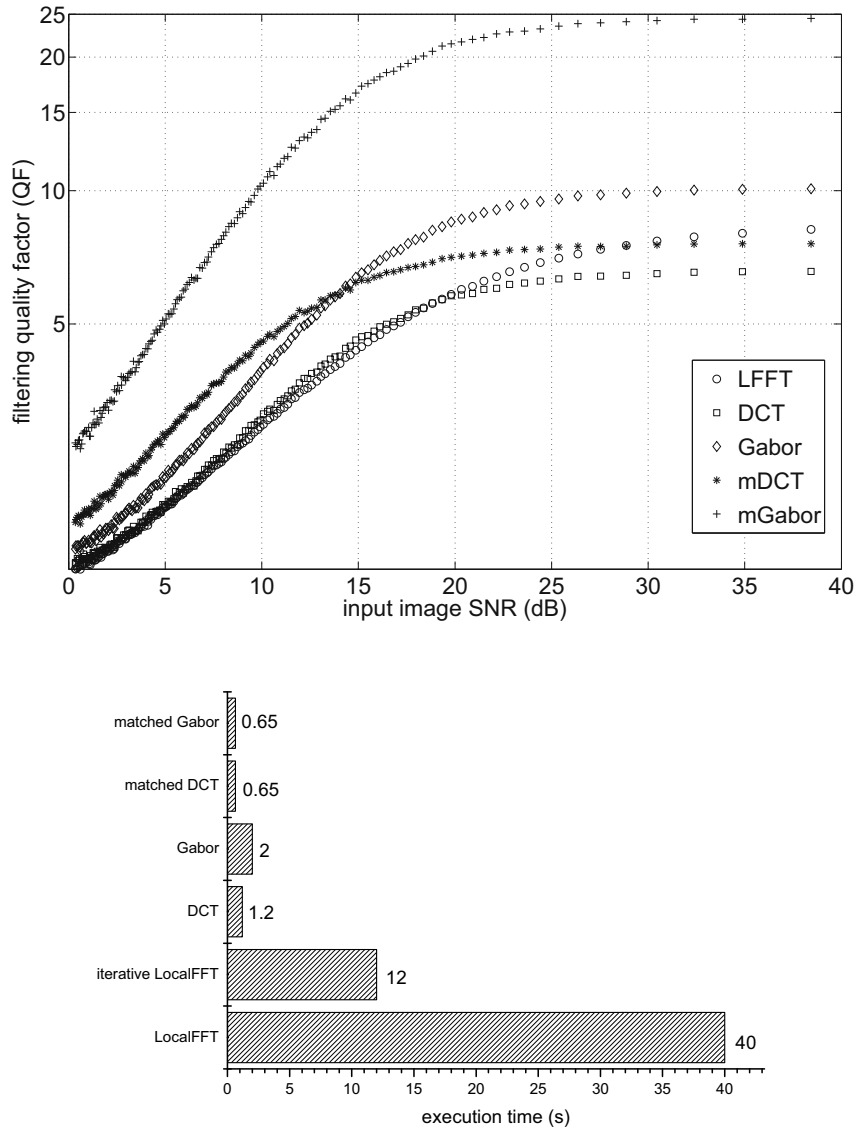
Figure 3.4: (a) Quality factor parameter (QF) for the different filters as function of the input image SNR. mDCT and mGabor are the "matched" versions of the DCT and Gabor respectively. (b) summary of the execution time of the different filters tested.

statistical modulation of intensity distribution, modeled as a random contribution at a macroscopic scale. Thus the speckle inherently degrades the filtered result and induces this saturation effect.

The execution time was compared for each filter, using a 512×512 px image, on an Intel Pentium® 4 processor at 3.4 GHz. The algorithms were implemented in the Matlab™ computing environment. The localFFT algorithm processes the image in more than 40 s. The incremental formulation of this filter consequently reduces the computation time down to 12 s, calculating the FFT on a 8×8 neighborhood in each case. The Gabor filterbank technique, with 9 different matrices H defined as in eq. 3.5 computes in about

2 s. DCT filterbank defined as in eq. 3.3 computes in 1.2 s when using 4 different masks. Finally, the "matched" versions of the DCT and Gabor filterbank are the fastest, with 0.65 s for both. Fig. 3.4b summarizes these different results.

3.2.2 Optimum object/reference wave ratio

Referring to eq. 2.12, it is obvious that the maximum interference pattern contrast is obtained when $|U_1(x, y)|^2 = |U_r(x, y)|^2$, in other words when the mean intensity of the reference and object wave on the CCD plane are equal. Nevertheless, as here the detection procedure involves filtering, it is important to study whether this condition is the same regarding the amplitude of the filtered signal.

A set of simulation has been run, varying the ratio between the mean intensity of the object and reference wave (parameters for the simulation are: $\lambda = 661$ nm, $d_i = d_o = 12$ cm, $f = 6$ cm, $dx = 4$ μm, diaphragm radius $R = 0.35$ mm, $z_0 = 47.3475$ mm, $x_0 = y_0 = 1$ mm, $L_c = 10\mu$m, $U_0(x, y) = 1$). For each simulated interferogram Gabor filterbank filtering using eq. 3.5 has been applied and the QF defined with eq. 3.6 was calculated. Fig. 3.5a presents the results without adding a random phase term to the input field, whereas to obtain results on fig. 3.5b, a random phase term has been added. For this second case each interferogram has been simulated 25 times to obtain a mean QF for each object/reference wave ratio.

(a)   (b)
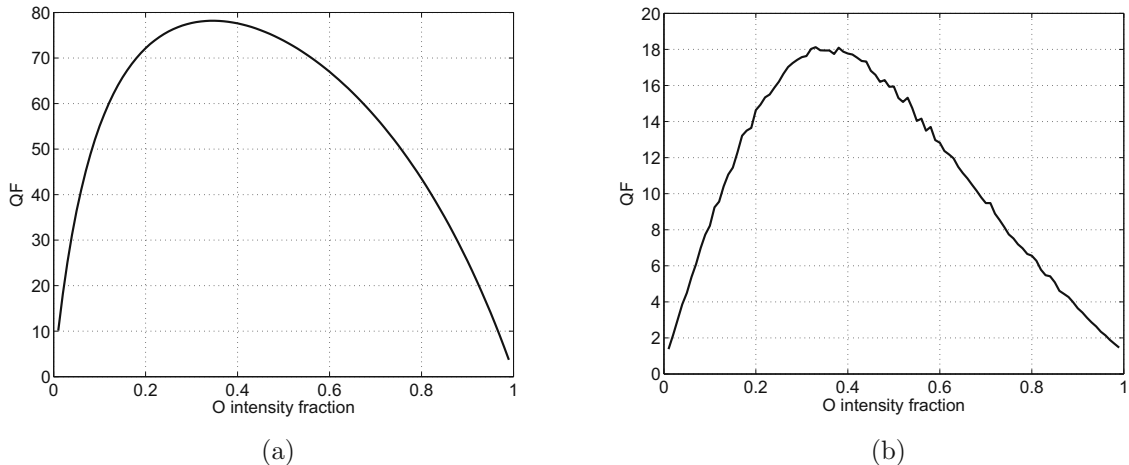
Figure 3.5: Optimum object/reference wave ratio. (a) without speckle, (b) with speckle (25x averaging).

As expected, QF values tends to zero when either the reference or the object beam intensity tends to zero. More surprisingly, the curves are not symmetric: the optimum fringe pattern detection does not occur when mean object and reference wave intensity are

equal. Maximum detection efficiency is reached when the mean reference intensity represents 65% of the total mean intensity ($\langle I_{ref} \rangle = 1.86 \langle I_{obj} \rangle$). This observation concords with the results obtained by Charrière *et al.* [90], when studying the SNR evolution on phase signal reconstructed with DHM. Moreover, it clarifies the fact that the filtering procedure is optimum when, at the CCD plane, more power is coming from the reference arm than from the object arm, which is in fact also observed practically during interferograms acquisition. One explanation of this phenomenon could be that the intensity distribution of the reference wave if more homogeneous than the one of the object wave: by promoting the signal coming from the reference, an interference term with smaller dependence on the variations induced by the object is obtained, which gives a cleaner signal and thus a better filtering.

3.3   Filter output cleaning

This section presents the two steps involved in the cleaning of the filtered interferograms. As it is presented on fig. 3.3b, filters can sometimes output high values also for points that are not lying in the coherence zone (in other words, where there is no fringes). This is the case even on simulated images, and it is due to the inherent statistical properties of the speckle pattern, which can potentially create local patterns that appear as the fringes to be detected. For measured data, another cause of these noisy high output values are the inhomogeneities of the sample reflectivity, or unwanted fringes due for example to parasitic reflexions on optical elements of the system.

The first step of the procedure is to locally threshold the signal. The filtered image is typically divided in blocks of 80×80 overlapping pixels. Fig. 3.6 shows a block diagram of the thresholding process.   This technique has the advantage to keep the intensity information of the pixels, and minimize the effect of local variance in intensity.

The curve to extract is characterized by an accumulation of high intensity data points and the points after thresholding are not necessarily interconnected. The apparent width of the curve cannot be assumed to be constant, and after thresholding, there often remains very isolated points that do not correspond to any data, so that the thresholded image has to be processed further.

A disk is moved through the points to extract successively the meaningful data, the disk radius is typically of 35 pixels. A starting point is found by sliding the disk along the rows of the image. Once the mean intensity in the disk reaches a threshold empirically determined as 4 times the mean intensity calculated over the entire image, it is assumed that the points within the disk belong to the curve to extract. First, the disk center is placed on the gravity center of the non-zero pixels within the disk. The neighborhood in
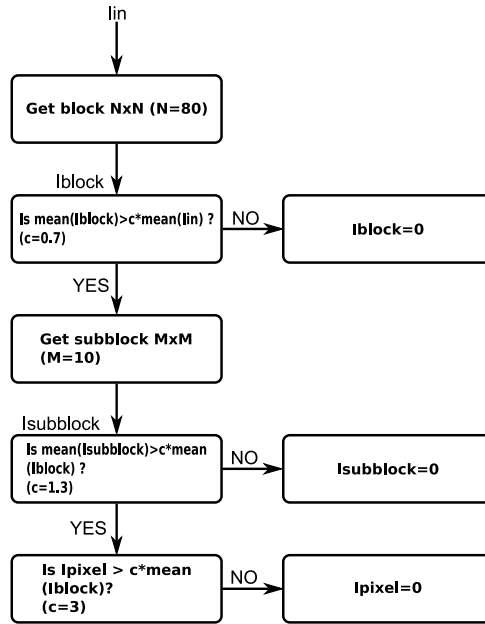
Figure 3.6: *Block diagram of the local thresholding method, typically used values for c, N and M are in parentheses.*

the sliding disk is extracted and the coordinates of the gravity center are also recorded.

A local estimation of the variance is then used to find the direction of the curve. The covariance matrix $C_x = \sum \boldsymbol{x} \cdot \boldsymbol{x}^T$, where $\boldsymbol{x}$ is the coordinates vector of the pixels weighted by the pixel intensity, is calculated, and expressed in its eigen basis.

$$C_x = [\boldsymbol{\nu_1}\ \boldsymbol{\nu_2}] \cdot \begin{bmatrix} \lambda_1 & 0 \\ 0 & \lambda_2 \end{bmatrix} \cdot \begin{bmatrix} \boldsymbol{\nu_1}^T \\ \boldsymbol{\nu_2}^T \end{bmatrix} \tag{3.7}$$

In eq. 3.7, the eigenvector $\boldsymbol{\nu_i}$, $i = 1, 2$ associated with the maximal eigenvalue defines the direction of the maximal variance, corresponding to the direction toward which the next points belonging to the curve have to be extracted. The sliding disk is translated on a distance that equals its radius in that direction. This procedure is repeated until at least one of these conditions are fullfilled:

- Two successively extracted gravity centers are too close to each others (distance between the two gravity centers is smaller than the disk radius), so that the disk is stuck in place. That mean that, either the curve is closed, either the end of a non-closing curve has been reached.

- The sum of pixels intensities in the neighborhood is smaller than a given threshold.

- A maximal number of iteration is reached.

For one acquisition, the result is a binary depth map, containing either zero, or the

depth value of points situated in the coherence zone (see fig. 3.3d). The non-zero coordinates in the map are then extracted and converted into real values in millimeters with the use of the transverse magnification characteristic described in section 4.3. At the end of the process for the complete stack of interferograms, the tri-dimensional information is stored in 3 vectors $\boldsymbol{x}$, $\boldsymbol{y}$ and $\boldsymbol{z}$. The length of these vectors corresponds to the number of acquired points.

3.4   Surface fitting

We now have 3 vectors $\boldsymbol{x}$, $\boldsymbol{y}$ and $\boldsymbol{z}$ containing the points detected to be on the surface. In this section the problem of representing sparse and non-uniformly distributed data is addressed. For a typical acquisition procedure with the setup described in chapter 4 on a surface contained in a volume of $20 \times 7 \times 5$ mm^3, a subset of about 1210 points lying on the measured surface are located in 3D. Uniformly distributed, this would give a points density of 1.73 points per mm^3, which would be sufficient to obtain direct surface visualization. However here we have to deal with scattered data with completely non-uniform sampling. As an example, to obtain valuable surface rendering based on these 1210 points, interpolation on 8011 points is required.

A parametrization of a tube-like surface can be expressed as $r = r(\boldsymbol{\theta}, \boldsymbol{z})$, but very strict continuity condition imposed by the periodicity of $\boldsymbol{\theta}$ often prevents to achieve adequate fitting for noisy data. In our case we chose to implicitly define the surface as $f(\boldsymbol{x}, \boldsymbol{y}, \boldsymbol{z}) = 0$.

To achieve correct surface interpolation, off-surface points are synthetically generated. They are defined as points situated at a distance $\pm d$ from the surface, in the direction of its normal. By adding these points, we create a numerical distance function $d_i = f(x_i, y_i, z_i)$. This function is then interpolated with RBFs defined as [79]:

$$s(\boldsymbol{x}) = p_m(\boldsymbol{x}) + \sum_{i=1}^{n} \lambda_i \cdot \Phi(|\boldsymbol{x} - \boldsymbol{x}_i|)$$
$$, \ \boldsymbol{x} \in \mathbb{R}^3, \ \lambda_i \in \mathbb{R}, \tag{3.8}$$

where p_m is a low-degree polynomial, here we typically use a *1st* order polynomial, and Φ is a radially symmetric function from $\mathbb{R}^+$ to $\mathbb{R}$. Thus the problem is to find the polynomial coefficients and the λ_i in eq. 3.8 satisfying:

$$s\left(\boldsymbol{x}_i\right) = f\left(\boldsymbol{x}_i\right), \qquad i = 1, 2, \ldots, n$$
$$\sum_{i=1}^{n} \lambda_i p\left(\boldsymbol{x}_i\right) = 0, \tag{3.9}$$

where $f\left(\boldsymbol{x}_i\right)$ are the sparse and generally non-homogeneously dispatched values of the distance function created from the measurement and the numerically added off-surface points. The second equality in eq. 3.9 corresponds to side conditions. This leads to a linear system that has to be solved in order to find the different coefficients defining the RBF:

$$\begin{pmatrix} A - \gamma I & P \\ P^T & 0 \end{pmatrix} \begin{pmatrix} \lambda \\ c \end{pmatrix} = \begin{pmatrix} f \\ 0 \end{pmatrix} \tag{3.10}$$

Where A and P are matrices containing the values of the radially symmetric function Φ and of the low-degree polynomial basis (i.e. $P_{i,j} = p_j\left(\boldsymbol{x}_i\right)$, with p the polynomial basis), respectively. γ is a factor added to smooth the fitted surface. For a high value of γ, a very smooth surface is obtained, but of course in this case the fitting accuracy is lower. The size of A in eq. 3.10 is N×N, with N the number of sample. If a *1st* order polynomial of the form $p\left(\boldsymbol{x}\right) = c_1 + c_2 x + c_3 y + c_4 z$ is used, this leads to a system of N+4 equations. It is thus clear that the direct resolution of eq. 3.10 is not suitable for measurements with a big number of samples. However, it has to be mentioned that fast methods exists [82; 83; 84; 85; 86].

Fig. 3.7 shows an example of measurement on a cylinder of 9 mm diameter along with the mapped surface for visualization. As data are most of the time noisy, the parameter γ in eq. 3.10 is typically chosen between 1 and 3 to obtain a relatively smooth surface without introducing to much artifacts. 572 data points were acquired to obtain results depicted on fig. 3.7, RBF was then evaluated in a box of 50×50×50 voxels. The basis function here is $\Phi\left(\boldsymbol{r}\right) = \boldsymbol{r}$, and the degree of the polynomial was set to 1. The last step of the surface fitting procedure is to find points satisfying $f\left(\boldsymbol{x}, \boldsymbol{y}, \boldsymbol{z}\right) = 0$ by isosurfacing.

In the following of this chapter, a survey of the reconstructed surface quality and fidelity is conducted. The study is based on the extracted points used to obtain the visualization of the 9 mm diameter cylinder presented on fig. 3.7. Two different methods for off-surface points generation are investigated, as well as the influence of the smoothing factor γ.
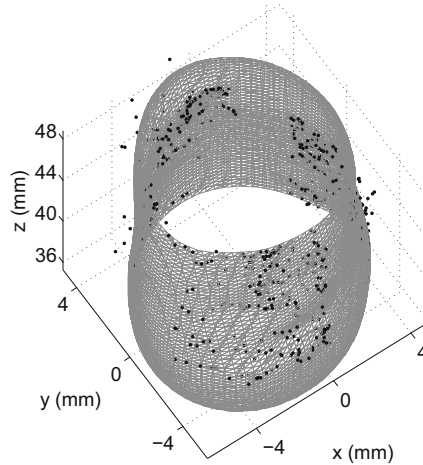
Figure 3.7: Example of measurement on a 9 mm diameter cylinder. Black dots represent acquired data, mesh is the fitted surface with $\phi\left(\boldsymbol{r}\right) = \boldsymbol{r}$, $\gamma = 1.5$.

3.4.1   Surface normals

Surface normals estimation is of utmost concern to achieve correct 3D representation. One way is to estimate a local tangential plane by computing the covariance matrix of the points positions within a ball of radius r [87]. The covariance matrix is defined as $C = \frac{1}{n}\sum_{i=1}^{n}\left(\boldsymbol{p_i} - \overline{\boldsymbol{p}}\right)\left(\boldsymbol{p_i} - \overline{\boldsymbol{p}}\right)^{T}$. The normal direction to the locally fitted plane corresponds to the eigen-vector associated to the smallest eigen-value. This Minimum Variance Axis Normal Estimation (MVANE) solution often provides good results but sometimes may fail due for example to lack of data or poor sampling. To achieve correct rendering, it is not necessary to associate normals with every measured point. Here, the smallest eigen-value is compared to a threshold variance, and off-surface points in the direction of the surface normal is added only if the smallest eigen-value is below this threshold. By doing this, normals to the surface are computed only if the local measurements are sufficiently lying on the same plane. This limits false normals creation that can arise if we are considering a steep inflexion point, or if noisy data are corrupting the plane estimation.

Another way to estimate normals is to take advantage of the fact that the different sets of points are situated on planes perpendicular to the optical axis of the endoscope, which is more or less also the axis of the tube-like structure. If off-surface points are created at distances close enough from the acquired points (in the order of 1 mm), this assumption is correct and will not induce large errors. The normal vector to the surface is then simply defined as $\boldsymbol{n} = (x, y, 0)/\sqrt{x^2 + y^2}$. This method for normal direction calculation is hereafter referenced as Cylindrical Shape Normal Estimation (CSNE). It is important to be aware that this method constrains the fitted surface to be cylindrical, and indeed,

it is a convenient *a priori* when dealing with surface mapping on "full view" of tube-like structures such as trachea or bronchus. Anyway, for observation of non cylindrical samples, one has better to choose MVANE method, in order not to introduce artifacts due to a falsely imposed shape.

In the following, the root mean square error (RMSE) between the radius of the fitted cylinder and the actual radius of 4.5 mm is taken as an estimator of the correctness of the measurement:

$$RMSE = \sqrt{\frac{1}{N-1}\sum_{i=0}^{N-1}(4.5 - r_{fit})^2}. \qquad (3.11)$$

The radius RMSE calculated on the measured points before fitting is 0.73 mm. For the two normal calculation methods, the surface mapping procedure was repeated for different values of the variance threshold used to determine if a normal should be calculated for a specific point. Each time, the covariance matrix was calculated within a ball of 3 mm radius. Results are presented on fig. 3.8a and 3.8b. The obtained surfaces for threshold values labelled from a to d on each graphs are presented in table 3.1. Off-surface points were created at a distance of 2 mm in the direction of the calculated normal and γ was set to 2.

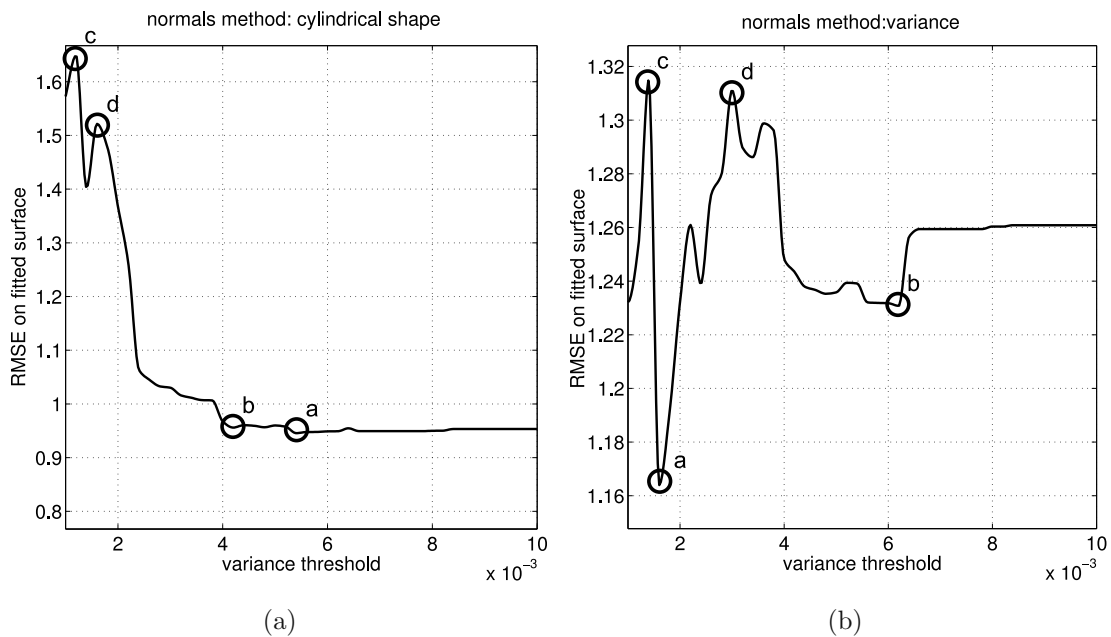(a)   (b)

Figure 3.8: Fitted surface radius RMSE as function of variance threshold, with covariance matrix calculated within a ball of 3 mm radius. (a) Radius RMSE evolution when imposing a cylindrical shape for surface normals calculation. (b) Radius RMSE evolution with normal direction determined by Minimum Variance Axis Normal Estimation (MVANE).

For low values of the variance threshold, RMSE values are the highest. This can be

explained by the small number of off-surface points, which prevents correct rendering. On the other hand, RMSE is more or less constant for variance threshold values above $4 \cdot 10^{-3}$ when using the CSNE method. For MVANE method, RMSE is minimal when variance threshold is set to $1.6 \cdot 10^{-3}$, but it is an isolated point surrounded by high values of RMSE. This choice for variance threshold is optimum for this set of measurement, but it cannot be stated that this would be the case in general. To obtain reliable surface mapping, variance threshold values should be chosen between $5.6 \cdot 10^{-3}$ and $6.2 \cdot 10^{-3}$, on this range this produces a reconstructed surface with quite low constant RMSE. After this point, a degradation in term of the RMSE of the mapped surface is observed. Lines 3 and 4 of table 3.1 shows the shape of the mapped surface, letters in the lower-right corner of each case in the table correspond to the highlighted points in fig. 3.8.

3.4.2   Gamma parameter

To study the influence of γ, the surface mapping procedure was repeated for different values of this parameter, for the CSNE and MVANE methods. The covariance matrix was calculated within a ball of 3 mm radius and variance threshold was set to $5.4 \cdot 10^{-3}$ for CSNE method and $1.6 \cdot 10^{-3}$ for MVANE method, which corresponds to the minimum of fig. 3.8a and 3.8b, respectively. Off-surface points were created at a distance of 2 mm for every case.
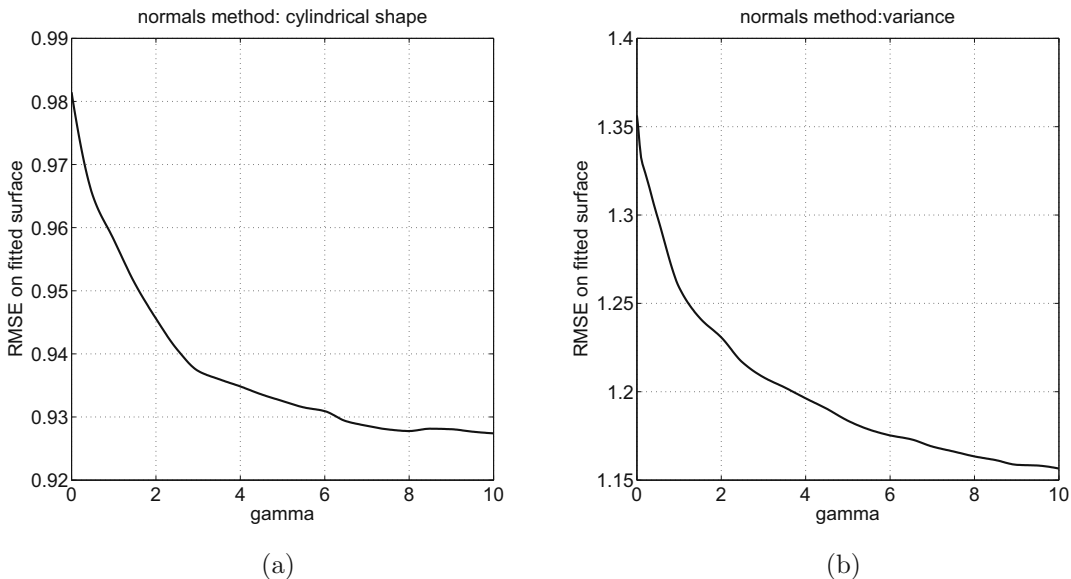

Figure 3.9: *Fitted surface radius RMSE as function of γ, with covariance matrix calculated within a ball of 3 mm radius. (a) Radius RMSE evolution when imposing a cylindrical shape for surface normals calculation. (b) Radius RMSE evolution with normal direction determined with the MVANE approach.*

When comparing results on fig. 3.9a and 3.9b, we first observe that the radius RMSE is always bigger when using the MVANE method. It is important to remember that CSNE imposes a cylindrical shape to the mapped surface, and as the measured sample is indeed a cylinder, it seems normal to obtain smaller RMSE with this method. Nevertheless, *a priori* knowledge of the global surface shape is not always available, and in the general case, only the MVANE method can be applied.

For $\gamma = 0$ the mapped surface always passes exactly through the measured points. However, even with low noise data, this can possibly result in eq. 3.10 being badly conditioned and prevents its numerical resolution. For both method, a rapid drop in term of radius RMSE is observed for $\gamma < 4$. Lines 1 and 2 of table 3.1 show the shape of the obtained surface for γ values ranging from 0.1 to 8.0. With an optimum variance threshold, the mapped surface using the cylindrical shape normal estimation is always closed, while it is not the case for the minimum variance axis normal estimation method. For CSNE, setting γ between 1 and 3 provides good results without too much smoothing of the surface, while for MVANE, an higher γ value has to be set as to ensure that there are no "bumps" on the fitted surface.
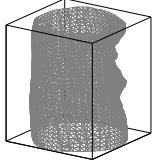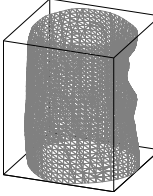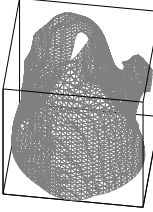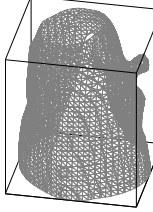
3.4.3   Study summary
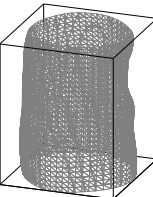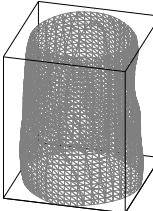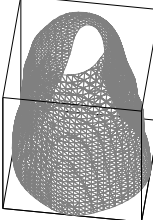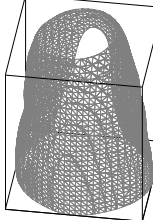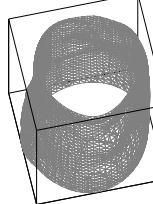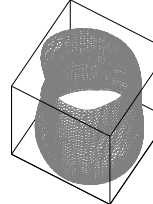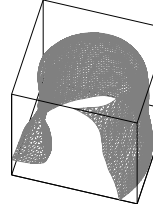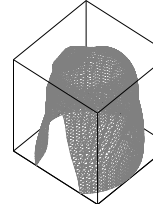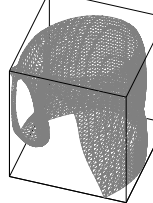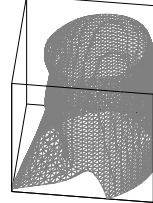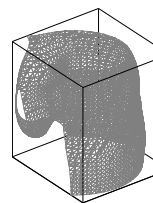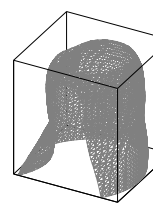
	CSNE		MVANE	
gamma: radius: 3 mm dist: 2 mm var. thresh.: $5.4 \cdot 10^{-3}$ (CSNE) $1.6 \cdot 10^{-3}$ (MVANE)	0.1	1.0	0.1	1.0
	4.0	8.0	4.0	8.0
var. thresh.: radius: 3 mm dist: 2 mm gamma: 2	a	b	a	b
	c	d	c	d

Table 3.1: Summary of the surface fitting parameters study. Lines 1 and 2: Numbers in the lower-right corner correspond to different values of γ. Lines 3 and 4: letters in the lower-right corner correspond to the highlighted points in fig. 3.8.

Selected standard values

Table 3.2 presents the typical parameters that have been chosen for surface mapping, for the two normals calculation methods, along with a preview of the result on the measurement of the cylinder. Off-surface points distance is shortened, and variance threshold as well as γ value are increased when using the MVANE method compared to the CSNE method. The root mean squared error on the measured radius is about 1 mm in each case, and corresponds to the precision of the measurement on this cylinder.
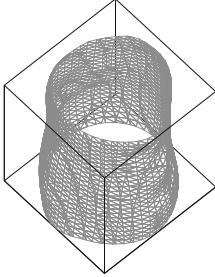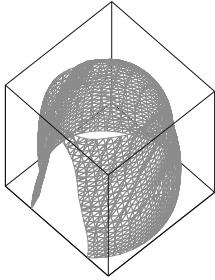
Configuration	radius RMSE (mm)
Measured points	0.73
CSNE method: variance ball radius: 3 mm variance threshold: $5 \cdot 10^{-3}$ off-surface points distance: 2 mm γ: 2.5	0.95
MVANE method: variance ball radius: 3 mm variance threshold: $6 \cdot 10^{-3}$ off-surface points distance: 1.2 mm γ: 3.5	1.03

Table 3.2: Selection of commonly used parameters.

To obtain correct rendering of the surface, the basis function $\phi(\boldsymbol{r})$ has to be well chosen in order to accommodate for the particular tube-like shape of the specimen. It was observed that infinite support basis function are better suited. Compared to finite support functions, they induce less artifacts for cylindrical shapes. Moreover, infinite support functions are more likely to fill holes due to lack of data in certain regions. We typically used $\Phi(\boldsymbol{r}) = |\boldsymbol{r}|$ as basis function. The use of the 3D linear basis function also has the advantage of computational simplicity, thus reducing the 3D reconstruction time. Fig. 3.10 shows the isosurfacing result when using a gaussian shaped radial basis function with 0.4 mm FWHM (fig. 3.10a), compared to the result obtained when using the 3D linear $\Phi(\boldsymbol{r}) = |\boldsymbol{r}|$ (fig. 3.10b), respectively. Off-surface points were generated using the CSNE method at a distance of 2 mm, with a threshold set to $5.4 \cdot 10^{-3}$ and γ was set to 0.1. Due to the sparse sampling of the measurement, the surface cannot be interpolated with the compactly supported gaussian basis function, and the isosurfacing procedure completely fails to isolate the points where $f(\boldsymbol{x}, \boldsymbol{y}, \boldsymbol{z}) = 0$.
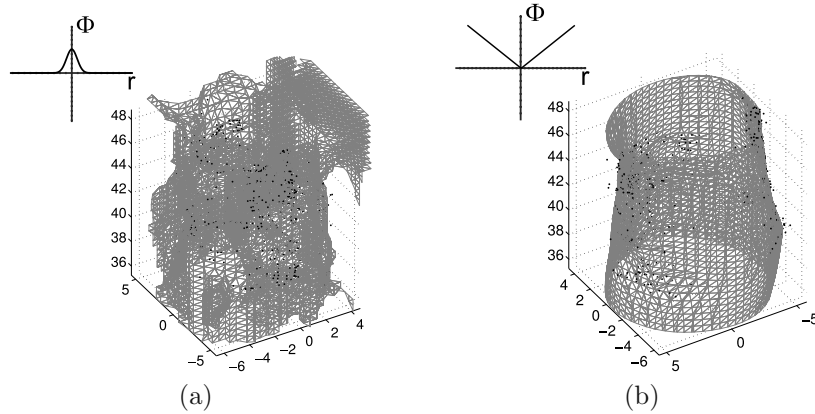
Figure 3.10: Compactly vs non-compactly supported basis function (a) Gaussian shaped RBF defined as $\Phi\left(\mathbf{r}\right) = \exp\left(-15.4\left|\mathbf{r}\right|^2\right)$. Compactly supported RBF cannot fills holes and prevents isosurfacing of finding an implicitly defined surface. (b) 3D linear RBF $\Phi\left(\mathbf{r}\right) = \left|\mathbf{r}\right|$ with infinite support. Here the holes are filled and isosurfacing procedure completes.

3.5 Conclusion

In this chapter the different filters investigated to extract the coherence zone on the interferograms have been compared. Gabor filters have shown best efficiency to process the acquired signal. The possibility to create "matched" versions of the filters, taking advantage of some *a priori* knowledge on the fringes patterns, has been exposed, and has shown that the computation time could be reduced by an order of magnitude compared to local Fourier spectrum calculation. Moreover, the use of these "matched" filters gives access to a better SNR in the filtered signal, compared to the generic approach of creating a filterbank. Local estimation of the filter output intensity variance has been used to enhance selectivity, and has been successfully applied to remove non-significant remaining pixels, thus providing a robust method for the extraction of the tri-dimensional data points cloud. The problem of surface rendering has been solved by the use of radial basis functions, which are particularly adequate for surface mapping on sparse and non-uniformly distributed data points. The simple 3D linear radial basis function has shown best results. Necessary normal estimation for RBF fitting has been achieved with two different methods. When constraining the surface to be cylindrical, errors between the measured points and the fitted points can be reduced when representing tube-like structures. Parameters that have to be set during the interpolation procedure have been studied in order to find typical values. For both normal estimation methods, an overall resolution in the order of 1 mm has been achieved on the fitted surface.

Chapter 4

Endoscopic setup

4.1 Introduction

Size of the lumen and length of the stenosis are critical values to determine the appropriate stent dimension to use, thus optimizing chances of recovery. Quantitative measurements of human upper airways can be performed by either direct or indirect means. Indirect techniques, such as radiology, computed tomography (CT), virtual bronchoscopy (VBS) and magnetic resonance imaging (MRI) provide accurate results, but are very expensive, time consuming and more importantly cannot be performed at bedside just before or after an operation.

On the other hand, direct measurement techniques can be used to achieve *in situ* diagnostics of upper airways. They are performed with rigid endoscopes, fibroscopes, and with specifically designed probes, such as the Optical Coherence Tomography (OCT) method [3; 4], and more recently, the Fourier Domain Optical Coherence Tomography (FD-OCT) [5], which surpasses the classical OCT in term of both speed and signal-to-noise ratio. Similarly, Yelin *et al.* used a polychromatic light source and a grating as spectral dispersing element. The depth dimension can then be spectrally encoded by illuminating distinct locations with different wavelengths [7].

To combine endoscopic vision and depth information retrieval, attempts were made to use pulsed ESPI, Kemper *et al.* reported measurements on porcine stomach [49]. Rodriguez-Vera *et al.* have used a fibered setup for out-of-plane sensitive ESPI [35]. Schedin *et al.* published an extensive comparative study of different endoscopes that can be used for pulsed digital holographic Interferometry (pulsed DHI) [22]. Pedrini *et al.* used pulsed DHI with a fibered endoscope [23]. With a scope on miniaturization, Kolenovic *et al.* achieved endoscopic digital holography by placing the reference beam and the detector inside the endoscopic sensor body [26]. Two-wavelengths methods were also applied to endoscopy [39]. Endoscopic pulsed digital holography with 3 different object

illumination was recently achieved by Anaya *et al.* [24; 25], with measurements on a metallic cylinder excited at 2.18 kHz. In low-coherence speckle interferometry (LCSI), or other coherence gated techniques, the location of the coherent zone on an image is usually detected by calculating the correlation signal of many phase-stepped images, thus providing contouring. Balboa *et al.* reported 3D measurements using superluminescent diode and multimodes laser diodes in a fibered interferometer [57], using a five step algorithm for fringe amplitude extraction. Another possible method for phase extraction from a specklegram is to use spatial phase shifting (SPS), in which the phase of a pixel is estimated from the intensity of the surrounding pixels, instead of the values of the same pixel at different times, as it is the case for time phase shifting. Kemper *et al.* reported a study on the optimization of SPS for endoscopic ESPI [48].

This chapter is devoted to the endoscopic setup used to obtain endoscopic 3D contouring of upper airways. It is based on an interferometer using a short coherence laser diode. Similarly to the coherence radar technique, the goal is to detect the location of the coherence gate on the image. With this device, only one acquisition is needed to obtain a contour depth. Usually, interferometric measurements are highly sensitive to phase fluctuations. However in our case, as the interferometric approach is used to detect wether there is coherent superposition or not, the setup is intrinsically not affected by phase fluctuations between acquisitions. This provides a sufficiently robust method to operate under medical environment.

Each component of the endoscopic setup is thoroughly described. Section 4.3 describes the optical design of rigid endoscopes. The endoscope used is characterized in term if its modulation transfer function (MTF). Section 4.4 presents the prototype that has been built, as well as the approach used to create an all-in-one software environment for data acquisition, signal processing, and tri-dimensional results visualization. Finally, results on hollow samples, both metallic and biological, are presented in section 4.6.

4.2   Setup Design

Fig. 4.1 shows a schematic of the device. The source is a low-coherence laser diode (LD), with a coherence length of about 0.3 mm. The setup mainly consists in a smooth reference wave speckle iterferometer. To illuminate the specimen, a monomode fiber (MF1) is placed in the object arm. Two realizations were investigated to enhance the diameter of the illuminated area: one with a diverging optic adjusted right after the fiber tip, giving access to a field of view of a diameter of 20 mm. This solution has the drawback that the maximum intensity point is situated slightly off-axis, which gives rise to good illumination conditions for one area, but not for the remaining circumference of the observed hollow

surface. This asymmetrical configuration showed good results when observing a side-wall, but is not optimum for signal detection on tube-like samples. The retained solution to achieve measurements on all the circumference of tube-like samples was to put a 1x3 optical coupler after fiber MF1, providing a more symmetrical configuration. The fibers MF11, MF12 and MF13 are equally spaced around the tip of the endoscope, as depicted on the detailed view of the fig. 4.1, which gives 3 illumination zones, with their maximum intensity centers located away from the optical axis. Distance between the optical axis of the endoscope and the fibers is chosen so that the illuminated areas do not overlap, assuring that there is no unwanted interference fringes, which could potentially result in misleading depth signal extraction. MF1 and MF2 are polarization maintaining fibers. Unfortunately, polarization maintaining optical couplers are high-tech custom parts, and it would have drastically increased the device cost to use one. Nevertheless, it has been observed that using polarization maintaining fibers at the beginning of the paths of the reference and object arm enhance the interference pattern stability.

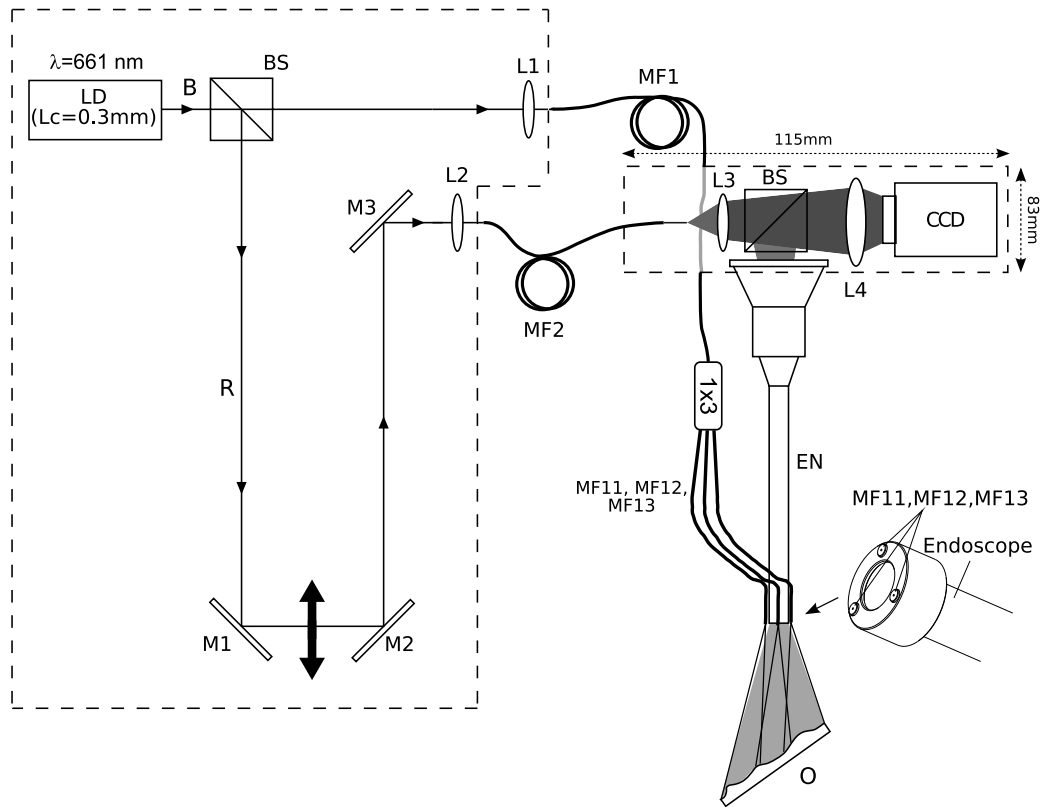*Figure 4.1: Schematic of the setup. LD: laser diode. BS: beam splitter. M1-M3: mirrors. L1-L4: lenses. CCD: charged-coupled device camera. EN: Rigid endoscope (Karl Storz 10320A). MF: monomode fibers. R: reference wave. O: object.*

A beam splitter (BS) separates the collimated beam (B) generated by the modulated laser diode (LD) into the reference beam and the object beam, which is injected into MF1

and then split in 3 parts, before illuminating the object (O) . The speckled light scattered by the object O is collected by the endoscope EN (Karl Storz 10320A).

The reference wave (R) is first directed to a delay stage (DS) formed by two mirrors (M1 and M2) mounted on a motorized axis. This way it is possible to adjust the time delay between R and O. The reference wave is then injected in another monomode fiber (MF2) so that the light can be transmitted to the part of the device attached to the endoscope eyepiece. It also provides a simple way to adjust the system to any other rigid endoscope, by simply updating the length of MF2 with respect to the length of the endoscope. MF2 also serves as spatial filter for reference beam cleaning. The object wave interferes on the CCD plane with the reference wave projected on the camera through a second beam splitter BS. A lens is placed at the end of the reference fiber to match the divergence and the size of the reference and object beam (L3). A lens (L4) is placed in front of the CCD to form a real image on the detector from the virtual one coming from the eyepiece of the endoscope. The end of the reference fiber is placed on a XY stage, in order to set the reference beam slightly off-axis, thus adapting the fringes frequency on the interferogram.

Fig. 4.2 shows the typical Fourier spectrum of an interference pattern obtained with the setup of fig. 4.1 when observing a plane perpendicular to the optical axis with only one fiber for illumination. The interference pattern itself is shown as inset. The carrier fringes clearly separate the interference terms from the zero order term, without any overlapping. As stated in chap. 2, section 2.3, the extraction of the fringes is possible with the procedures described in chap. 3, section 3.2. As an indication, the size of a subjective speckle grain when observed through the optical system consisting of the endoscope and of the lens L4 is about 5 pixels wide, which corresponds to more or less 30 μm, and the periodicity of the fringe pattern is on the order of 2-3 pixels.
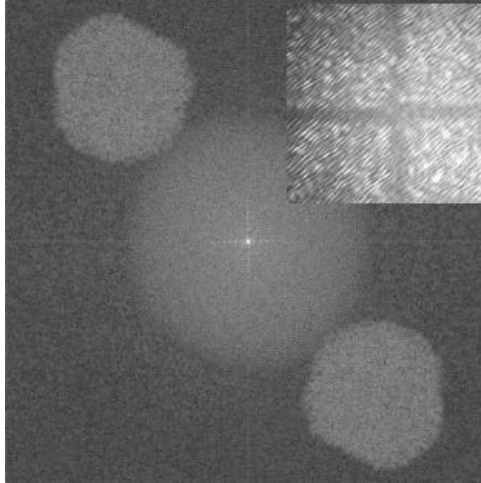
Figure 4.2: Typical Fourier spectrum of an interference pattern obtained with the setup of fig. 4.1, when observing a plane perpendicular to the optical axis with only one fiber for illumination. Inset: interference pattern.

4.2.1 Laser source

Fig. 4.3 shows the emission spectrum of the laser diode depicted in fig. 4.1 and its measured coherence length. To be more precise, a Fabry-Perot laser diode has typically several narrow longitudinal modes and the spectrometer cannot resolve them, so fig. 4.3.a only shows the envelope of the emission spectrum. The wider emission characteristic was obtained by modulating the current supplied to the laser diode with a sinusoidal command current of 40 mA amplitude at 40 kHz with a 90 mA DC component. As there is a current-wavelength dependency, this modulation shifts the central wavelength of the emission spectrum, which induces the broadening observed on fig. 4.3a. Practically, the modulation period is chosen to be at least ten times smaller than the acquisition time of the CCD. This produces an averaging effect, and during an acquisition time, a broadened spectrum is captured by the CCD. fig. 4.3b shows the evolution of the visibility of an interference pattern produced when modulating the laser diode current. The fringes visibility is reduced by 50% for an optical path difference (OPD) of 0.3 mm. This virtually reduced coherence length directly corresponds to the physical depth resolution of the system. Two side-lobes remain for OPD of -9 mm and +9 mm, having a maximum of 17% compared to the contrast of the central lobe. Modulating the laser diode also minimize temperature induced emission spectrum fluctuation, preventing mode-hopping and instabilities.

(a) Dashed: unmodulated. Plain: sinus modulated 40 kHz with $i_0 = 90mA$, $\Delta i = 40mA$

(b) Fringes visibility as function of OPD
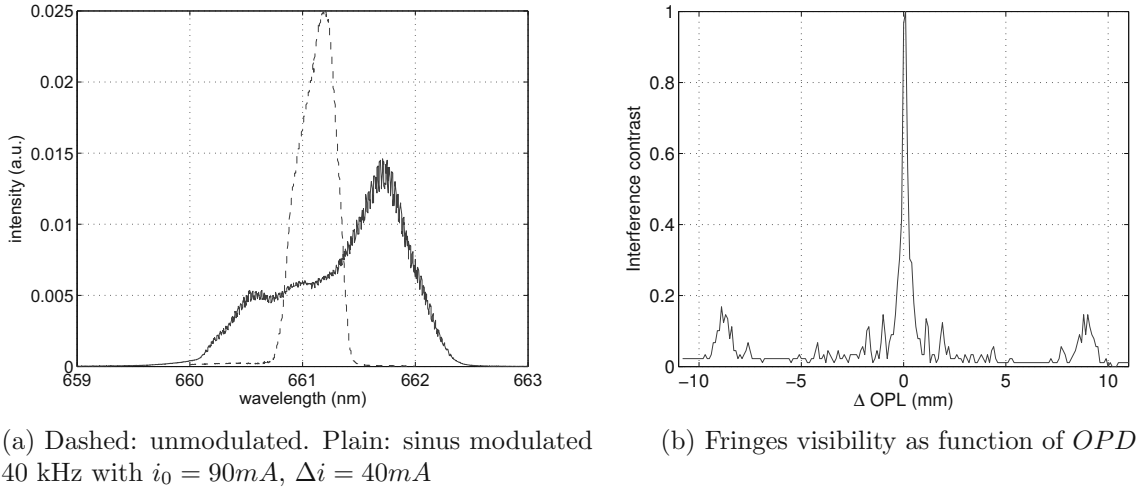
Figure 4.3: Spectrum (a) and coherence length (b) of the Opnext HL6526 laser diode.

Typical intensity on the CCD

12 mW optical power is typically delivered by the source to illuminate the sample (see subsec. 4.4.2 for a detailed description of the illumination designs). The backscattered light coming from the sample is collected through the rigid endoscope, passes through the recombining cube and the imaging lens and then the interference is recorded on the CCD. Indeed, the object beam encounters many refractive index changes before being recorded. Especially, there are numerous air/glass and glass/air interfaces in the endoscope, and, even with anti-reflective coating, losses are unavoidable. Moreover, half of the beam power is lost due to the recombining cube. This explains why when observing a flat aluminum surface perpendicular to the optical axis, the object beam power measured at the CCD plane is only about 230 nW! When observing hollow sample most of the time the incidence angle on the object is almost grazing, and thus the typical power coming back from the observed surface should be considered as even lower.

Practically, optimum detection condition has been observed when setting the reference beam power to 320 nW, which corresponds to 58% of the total intensity for lightly tilted samples. This result is slightly below the one calculated in subsec. 3.2.2, where an optimum of 65% has been expected. This difference can be explained by the inherent difficulty of measuring precisely such a low optical power. Anyway, this simple evaluation corroborates the fact that it is advantageous to put more power in the reference beam than in the object beam.

4.3 Endoscope

As a minimally invasive medical device, an endoscope is used to relay an image of an object situated in an area difficult to reach. There exists rigid and flexible endoscopes. Flexible endoscopes include fiber optics or electronics to relay the image to the camera. Rigid endoscopes provide superior imaging quality compared to flexible ones, and thus, are preferred whenever it is possible. An endoscopic system can be broadly divided into three distinct parts: the objective, the relay system and the eyepiece or imaging system for camera. This section describes these different subsystems for rigid endoscopes. The endoscope used in fig. 4.1 is also characterized in term of its modulation transfer function MTF, as well as the transverse magnification of the setup.

4.3.1 Optical design of rigids endoscopes

Typical rigid endoscopes mainly consist in 3 parts: the objective lens, the relay optics and the eyepiece, which in the case of imaging on a camera can be either replaced or followed by an imaging optic.

The objective forms an inverted image of the observed internal part. The entrance pupil of the endoscope is located at the front focal plane of the objective lens. To increase the field of view, a negative lens is added to the tip of the endoscope. An aperture stop is generally included in the endoscope objective. It has the drawback of limiting the lateral resolution of the system, but on the other hand, it extends the depth-of-field. Fig. 4.4a shows a schematic of a typical endoscope objective. Particularly, first element is a plano-concave lens, used to enhance the field of view. Next element is the aperture stop, limiting the accepted ray-bundle and making the chief-ray parallel to the optical axis. Folowing are the imaging elements, providing an inverted image to be passed to the relay optics.

Until 1960, relay optics consisted of doublet relay objectives and singlet field lenses. Then, H. Hopkins came with the idea of using rod-lens relays system [91]. Efforts on the improvement of relay optics were then going on both in term of manufacturing constraints and aberrations minimization [92; 93]. There also exists relay systems based on one block gradient index (GRIN) rod. Nowadays, Hopkins rod relay systems are most of the time used, they have numerous advantages over conventional relay systems: light throughput optimization, vignetting minimization, achromatization, mechanical stability. Endoscopes manufacturers have a wide combinations choice for the design: singlet or doublet glass/plastic rod lenses, and the so-called "modified Hopkins" design, which uses three glass rods in one relay stage. An extensive comparison of these relay stages can be found in [94]. Fig. 4.4b shows a typical design of Hopkins relay optic using doublet rod lenses. Relay systems are then cascaded in order to achieve the desired length for the

(a)

(b)

(c)

(d)
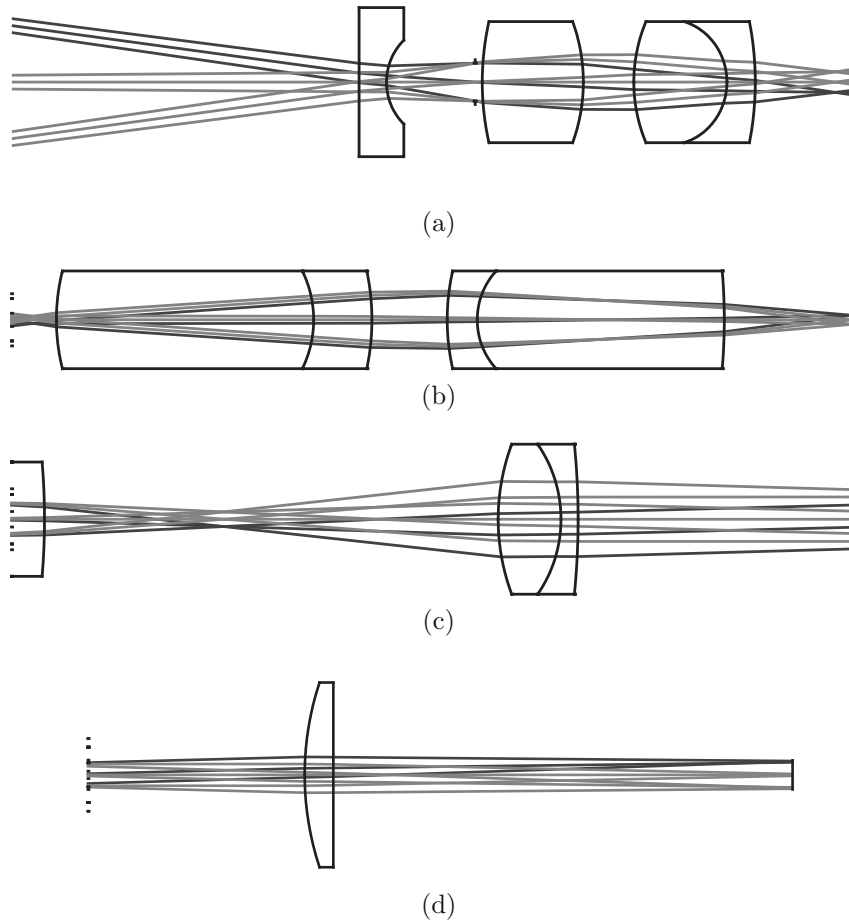
Figure 4.4: Main optical components of a rigid endoscope. (a) endoscope objective, (b) endoscope Hopkins relay system, (c) endoscope eyepiece, (d) lens used in the endoscopic setup of fig. 4.1 for imaging on the CCD.

endoscope. By correctly choosing the length and number of rods, it is possible to balance the dispersion, thus providing an achromatization stage directly in the relay system.

Very little informations were found about the eyepiece contained in the endoscope used in the setup of fig. 4.1 (Karl Storz 10320A). As a general design hint, conventional eyepieces are manufactured such that they provide a magnified image to be focused by the observer's eye. The eyepiece is placed at a distance from the image plane of the last relay system corresponding to its equivalent focal length. The magnification factor of the eyepiece is thus purely determined by its equivalent focal length. This design is presented on fig. 4.4c, with a simple doublet representing the eyepiece. As we wanted the system to be compatible with standard endoscopes commonly used in surgical facilities, it was decided to add a lens after the eyepiece (L4 on fig. 4.1), and not to remove the eyepiece from the available endoscope. A plano-convex lens with a focal length of 75 mm was used (see fig. 4.4d). This design provides a field of view of about 20°.

4.3.2 Modulation transfer function

A system is said to be linear shift-invariant when a weighted linear combination of inputs produces a weighted linear combination of outputs, and if a shift of the input signal produces an equal shift of the output signal. In a first approximation, optical systems are considered as linear shift-invariant [51; 95; 96; 97]. This reasonable approximation allows then the use of Fourier techniques. For sake of clarity and without any limitation, we consider here a 1-D treatment, which can be straightforwardly extended to a 2-D formulation. Eq. 4.1 represents the impulse response *h(x,y)*, with $f_1\left(x'\right)$ and $f_2\left(x\right)$ being the input signal and the output signal of the system, respectively. *h(x,y)* is in fact the response of the system to a perfect point source, and is a key characteristic for an optical system, it is commonly named *point spread function (PSF)*:

$$f_2\left(x\right) = \int_{-\infty}^{\infty} h\left(x - x'\right) f_1\left(x'\right) dx'. \tag{4.1}$$

Mathematically, a perfect point source can be described by a Dirac function, which is a function that tends to infinity for $x = 0$ and is 0 elsewhere, it is defined by,

$$\delta\left(x\right) = \lim_{N \to \infty} \exp\left(-N^2 \pi x^2\right) \tag{4.2}$$

with the main property,

$$\int_{-\infty}^{\infty} \delta\left(x - x_0\right) f\left(x\right) dx = f\left(x_0\right) \tag{4.3}$$

This means that the output produced by a Dirac function situated at one object point is equal to the value of the impulse response at the corresponding image plane. As the system is shift-invariant, it follows that the convolution between $h(x, y)$ and the object distribution is equal to the image distribution[1].

So one way to characterize an optical system would be to image a point-source, and this image would be the *PSF*. As it is really a challenging task to achieve point-source imaging, an easier way is to use the convolution theorem and measure the *optical transfer function (OTF)*, defined as:

$$OTF\left(k\right) = \mathscr{F}\left\{h\right\}. \tag{4.4}$$

Practically, for incoherent imaging systems, the *modulation transfer function (MTF)* is

---

[1]$h(x, y)$ links the object intensity distribution to the image intensity distribution for incoherent imaging, and the object field to the image field for coherent imaging.

measured, which is the modulus of the OTF. The response to a sinusoidal input is also sinusoidal, so if $f_1(x) = A_0 \sin(k_0 x)$, then $f_2(x) = A_m \sin(k_0 x + \Delta\Phi)$. Taking the Fourier transform of eq. 4.1 in this case gives:

$$A_m(-\delta(k+k_0) + \delta(k-k_0)) = A_0(-\delta(k+k_0) + \delta(k-k_0)) \cdot OTF(k) \qquad (4.5)$$

Multiplying the OTF by a Dirac centered at k_0 is equivalent to evaluating the OTF at k_0, and thus can be seen as a sampling. It follows that the MTF at k_0 can simply be evaluated by:

$$MTF(k_0) \propto \frac{A_m}{A_0} \qquad (4.6)$$

So the MTF can be measured by imaging successively sine patterns with different frequencies and observing the contrast in the image.

To characterize the rigid endoscope (Karl Storz 10320A), a transmission sine pattern with varying periods is back illuminated and imaged through the endoscope. The light source is a green filtered halogen lamp ($\lambda = 540$ nm). A lens of focal length f=100 mm is placed right after the eyepiece to form a real image on the CCD. Every sine pattern corresponds to a different spatial frequency, thus measuring the contrast for every imaged sine patterns and this for different distances between the target and the distal end of the endoscope evaluates the MTF, fig. 4.5 shows a schematic of the setup.

Practically, a region of interest (ROI) for both the border and the center of the imaged sine pattern was selected, then these ROI were line-scanned to extract the minimum and the maximum value of each line. The contrast value ($C = (I_{max} - I_{min})/(I_{max} + I_{min})$) was then calculated for each line and the mean contrast value of the ROI was retained.
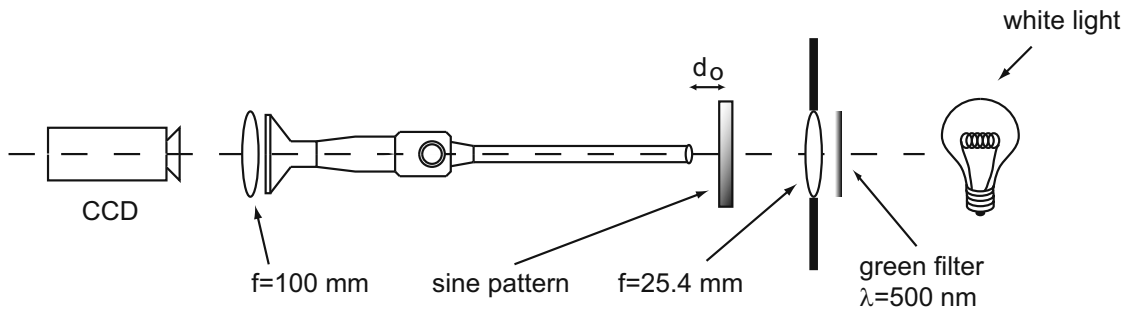

Figure 4.5: MTF measurement setup.

The elements depicted on fig. 4.4 have been introduced using the *Zemax* ® optical design software, such as to obtain the same image size as with the setup on fig. 4.1. The MTF for an object situated at 30 mm from the distal end of the endoscope has then been

calculated, fig. 4.6 shows the result, along with the MTF measured for the same object distance.
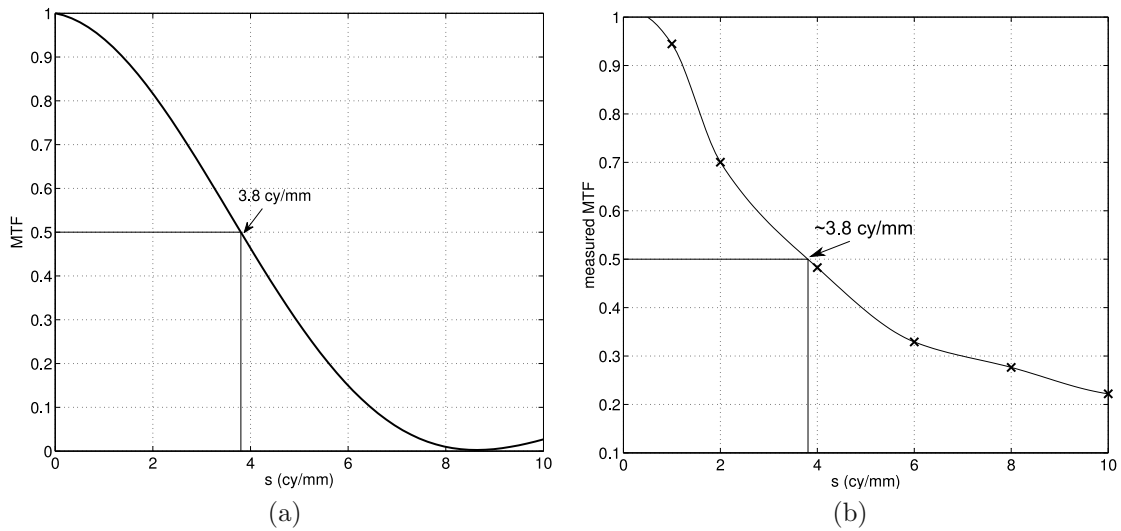

Figure 4.6: (a) MTF of the Zemax design at 30 mm, (b) measured MTF at 30 mm.

Measured MTF and *Zemax* MTF match for sines below 5 cy/mm. Above this value, measured imaged sines have a low contrast, but remain discernables, while software design predicts a very sharp contrast drop with a null contrast (gray image) for a 8.5 cy/mm sine.

Strictly speaking, the total MTF of the system described in fig. 4.5 should be influenced by the lens f=100 mm MTF. Nevertheless, as the aperture of the endoscope is clearly smaller than the aperture of the lens, and considering that the lens has a long focal length, it can be assumed that the lens MTF does not limit the total optical system MTF, and thus it can be stated that the measured MTF is the endoscope own MTF.

With the help of these MTF measurements, the cutoff frequency was reported for each object distance d_o. The cutoff frequency is defined as the sine pattern frequency for which the contrast is reduced to fifty percent, which is almost equivalent to the Rayleigh criterion, stating that two points are resolvable if the first diffraction minimum of the image of one source point coincides with the maximum of another. This gives a practical way of evaluating the lateral resolution of the endoscope as a function of the object distance. Fig. 4.7 shows cutoff frequencies as a function of object distance (d_o). Points marked with '+' correspond to the MTF in the border of the field of view, and points marked with 'o' correspond to the MTF for the center.

Based on the measurement on fig. 4.7 we observe that for the designed working distance of 30 mm, the cutoff frequency for regions in the border of the image is 3.375 cy/mm which gives a lateral resolution of about 0.3 mm. For the center of the image, a better
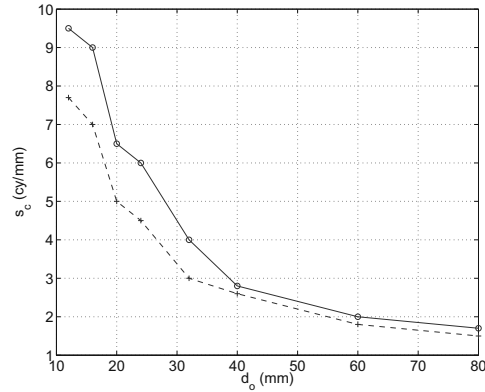
Figure 4.7: Measured MTF of the Karl Storz 10320A rigid endoscope. 'o': center of the field of view, '+': border of the field of view.

resolution is achieved, with a cutoff frequency of 4.5 cy/mm and thus a lateral resolution of 0.22 mm. In conjunction with the 0.3 mm coherence length of the laser source, it can be stated that the achievable measurement resolution is 0.3 mm along both the lateral and axial direction, for a plane of interest situated 30 mm away from the tip of the endoscope.

4.3.3   Transverse magnification of the setup

The transverse magnification of the setup has been measured, in order to account for scale changes of level curves acquired at different depths, and thus achieve true tri-dimensional repositioning of the extracted points. Simply, a test target made of millimeter paper has been moved along the optical axis, and the magnification factor has been reported for several positions of the test target. Fig. 4.8 shows the result. The left curve is the measurement, whereas the right curve presents a linear fit of the inverse of the transverse magnification as a function of the distance between the object and the tip of the endoscope. The linear fit can then be used to compute the magnification factor for every extracted level curves with respect to the position of the delay stage.
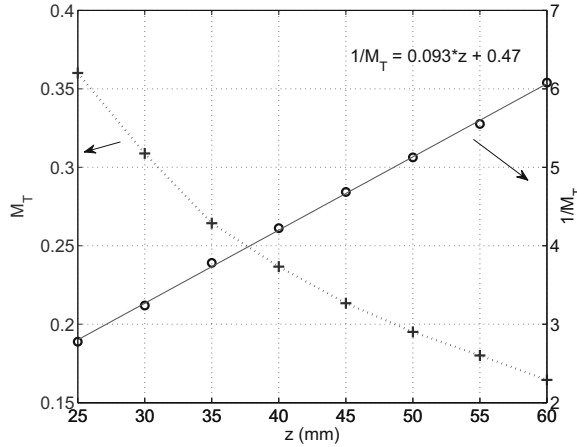
Figure 4.8: Left curve: transverse magnification of the endoscopic setup as a function of the object distance. Right curve: inverse of transverse magnification as a function of object distance, along with a linear fit. The linear fit can then be used to compute the magnification factor for every extracted level curves with respect to the position of the delay stage.

4.4 Prototype

4.4.1 Opto-mechanics

For our system to be usable in an operating room, it must be compact and very handy. The medical staff do not have time to adjust or tighten a screw. The designed prototype fits into a box of $115 \times 83 \times 94$ mm. A separated bench that could be situated on a table aside the patient bed includes the laser source and the delay stage, as well as two fiber injection systems, one for the illumination fibers, and the other one for the reference fiber. Fig. 4.9 shows a 3D CAD exploded view of the device attached to the endoscope.

A spring-locked standard adapter from $Storz^{®}$ is included so that the endoscopist can rapidly change the endoscope. A double XY tilt adjustment is included to finely tune the optical axis of the endoscope in the interferometric setup during the assembly, eventually prior to the measurement. The connector for the reference wave fiber, as well as the lens used to enlarge and adapt the reference beam to the object beam are placed on XY stages, so that the the off-axis position of the source point of the reference wave can be set up in order to create easily detectable fringes. Snapshots of the prototype can be found in appendix C.
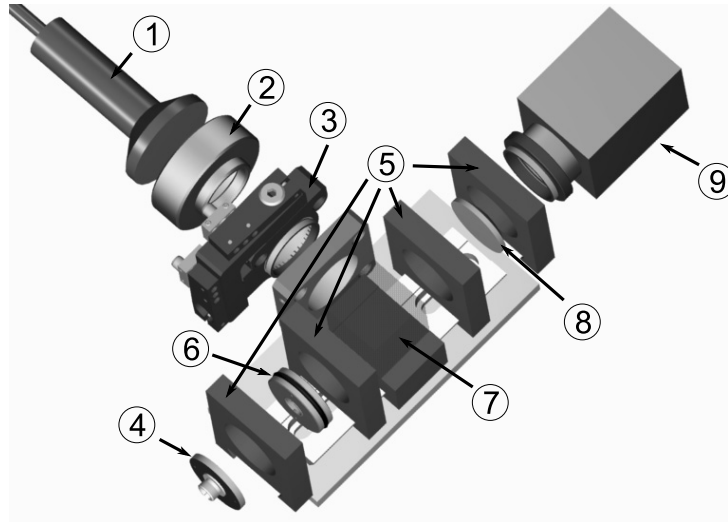
Figure 4.9: Exploded view of the prototype. (1) rigid endoscope, (2) spring-locked adapter for easy connection of the endoscope, (3) double XY axis tilt adjustment, (4) connector for reference wave fiber, (5) XY stages, (6) lens for reference beam adjustment, L3 on fig. 4.1, (7) BS for object and reference wave recombination, (8) lens for imaging on CCD, L4 on fig. 4.1, (9) CCD camera.

4.4.2   Illumination tip

Good, wide illumination at the distal end of the endoscope is needed in order to obtain a full view of the observed bronchial zone. It is not possible to use the built-in fiber bundle for illumination, as the different fibers are not of the same length, and their output would mutually interfere to create a very noisy illumination pattern. It has been decided to illuminate the sample through an external monomode fiber, put alongside the bronchoscope. The typical numerical aperture of a monomode fiber is in the order of 0.13, which is clearly not sufficient to obtain a large enough illumination cone with respect to the endoscope field of view. Two different realization have been investigated in order to widen the illuminated area: in the first one, a diverging optic has been positioned after the fiber end, and in the second one, multiple fibers have been used. The two solutions are discussed hereafter.

Ball lens design

Fig. 4.10a shows the arrangement for the first illumination design using a ball lens as diverging optic. The fiber was first passed through the ferrule and then inserted into a small cap of 3.5 mm outer diameter. On the other side of the cap, the ball lens was inserted until it firmly fit. Then, the position of the fiber end was adjusted to obtain the desired illumination area. Finally, the ferrule and the fiber were cemented together using an UV curable epoxy resin. With this geometry, an illumination area of about 20 mm

diameter is available at distance of 30 mm from the endoscope objective. The intensity pattern outputted with this arrangement is not high enough for points far from the optical axis of the fiber, and the intensity pattern is asymmetrical with respect to the optical axis of the endoscope, thus the algorithm fails on measurements on the whole circumference of cylindrical objects. Nevertheless, this design gave good results when observing only a part of a tube-like structure (see fig. 4.13). This shows that this configuration could be a good choice for 3D laparoscopic procedures. It has the advantage of using only one fiber, thus reducing system complexity and unavoidable power losses incoming at each fiber coupling or connecting system.

Multiple fibers design

To overcome the poor intensity available far from the optical axis of the illumination fiber, it was decided to distribute 3 illumination zones, spread each 120°. At the distal position of 30 mm from the endoscope objective, this gives 3 non overlapping areas of about 7 mm diameter. Monomode fibers packed with ferrules of 1.25 mm diameter were used and inserted in a small mount designed to be adapted around the metallic housing of the endoscope (see fig. 4.10b). The mount has an overall diameter of 9 mm and thus can fit into the surrounding tube used as an instrument channel during usual procedure. To split the object beam in 3, a 1×3 coupler is connected to the illumination fiber of the bench module. The overall optical path length of the reference arm is adapted, with respect to the length of the endoscope and illumination fibers, with a suitable patchcable to obtain reference arm and object arms length equalization within the scan range of the delay stage.

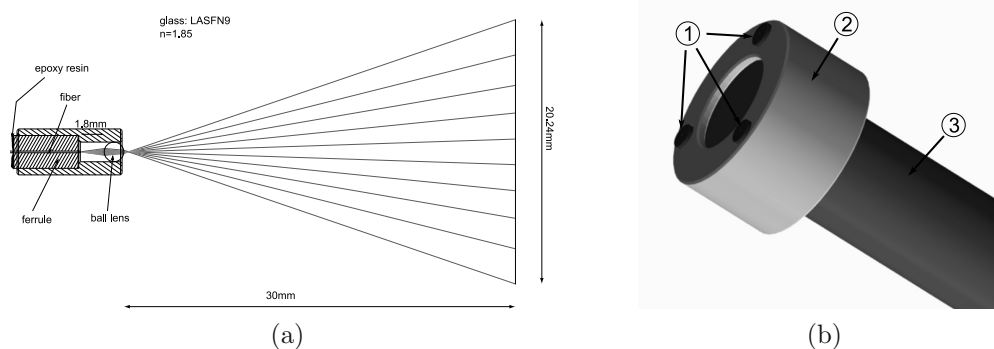(a)   (b)

Figure 4.10: (a) Zemax design of the ball lens illumination system. (b) Multiple fibers layout: (1) Illumination fiber end ferrule, MF11, MF12 and MF13 on fig. 4.1, (2) ferrules mount, (3) endoscope.

As said before, after filtering the signal is thresholded and remaining noisy points are removed. A starting point of the curve to be isolated is first found, and then the significant

data points shaping the curve are retained by following the maximum of variance of the data points cloud. It is technically difficult and really expensive to ensure that MF11, MF12 and MF13 are exactly of the same length. Consequently, for one position of the DS, the signal coming from the 3 illuminated zones corresponds to 3 different depths. However, we bypass this difficulty by a simple calibration procedure and the application of 3 efficient digital masks, so that the algorithms used to retain the significant data points can be applied sequentially to the filtered signal corresponding to each illuminated area, for one acquisition. First the lengths of the 3 fibers are measured. With this calibration procedure the absolute depth value for each extracted points is known with respect to the position of the DS. Then, a digital mask is used to set to zero pixels that correspond to object points that are not illuminated with the fiber currently processed. The procedure is repeated for each fibers, each time with a different mask. For each acquisition, we obtain 3 sets of measured points, each associated with a different depth.

Despite the need of repeating the procedure, the time needed to obtain the 3 sets of points is quite comparable to the time needed to obtain one set of points. Indeed, the number of pixels to take into account for each fiber is roughly the third of the number of pixels on the whole image, the only additional operation is the multiplication of the acquired interferogram by a digital mask, which is not a demanding task in term of computational cost.

4.5 Outline of the measurement procedure

Fig. 4.11 presents a flow chart of the measurement procedure associated with the endoscopic setup. For each acquisition, the signal is first filtered with one of the filters defined in eq. 3.2 to eq. 3.5, or their "matched" version. Then, the non-linear procedure described in section 3.3 are applied. Extracted pixels are converted to 3D coordinates in the object referential with respect to the positions of the delay stage and/or endoscope and are accumulated during the whole measurement. After all acquisitions are performed, a data cloud of unorganized and non uniformly distributed points corresponding to coordinates situated on the surface of the measured sample is obtained. Finally, surface fitting as described in section 3.4 is computed offline, in order to obtain a 3D model of the object.[2]
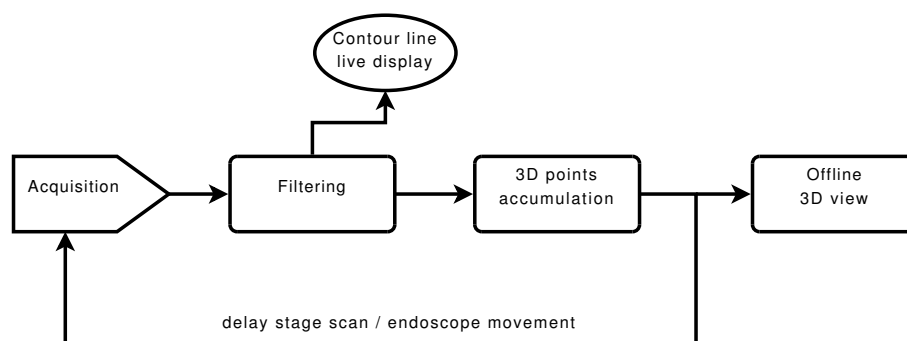
Figure 4.11: Flow chart depicting the different steps of the measurement procedure.

It has to be mentioned that scanning by moving the delay stage is an adequate procedure for stationnary object, and when the endoscopic part of the device can be kept in the same position during the scanning process. This is a big issue regarding the application of the system for routine bronchoscopic inspection, as windpipe and bronchial tubes are clearly not stationnary, and an endoscopist cannot manually maintain the endoscope in the same postion during a scan time. In order to overcome this problem and thus head toward clinical testing of the setup, an envisaged solution would be not to change the length of the reference path, but to record the position and orientation of the endoscope by embedding a magnetic sensor with the endoscopic system[3], and acquire the interferograms "on the fly" at the same time as the endoscopist inspects the cavity.

---

[2]Detailed software implementation can be found in appendix E.

[3]NDI Company commercialize medically compliant magnetic tracking devices (Aurora® system).

4.6   Results

In this section different measurements that have been achieved are presented. They have been made on samples of different materials (paper, metal, and biological tissue), either with one fiber for illumination, or with the 3 fibers approach. In particular, results on *ex vivo* pig bronchi, presumed to be highly representative of the signal that will be obtained on human upper airways in a clinical environment are presented. Results obtained using one fiber for illumination and a diverging optic are first exposed, then results achieved with 3 illumination fibers are discussed.

One fiber illumination

Inclined plane

As a first try, measurements were made on a tilted plane, as illustrated on Fig. 4.12. The field of view is 5 mm. 3D reconstruction was achieved by scanning with the delay system (see mirrors M1 and M2 on fig. 4.1) with steps of 0.2 mm. The measured plane is made of a standard white paper, which provides an homogeneous diffusive sample, but with a small mean free path. The filtering was made with the local FFT technique (eq. 3.1). The measured 3D points are indicated with black dots, and the mesh corresponds to the surface interpolating the data points. As it can be seen, the extracted points are sufficiently lying on a plane so that the mapped surface is flat. RMSE between the measured points and a flat plane is 0.4 mm, which is the same value as the one obtained with the measurement presented on fig. 2.9.
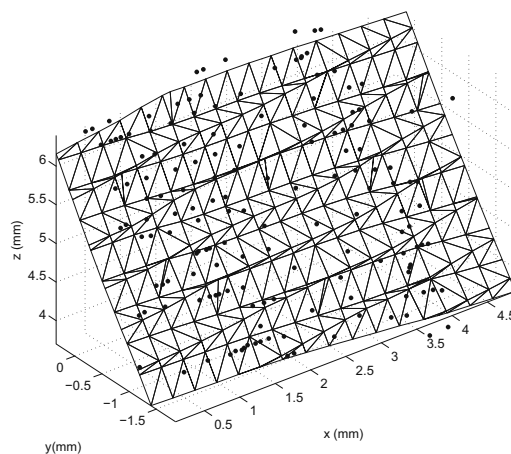

Figure 4.12: Validation measurement on a tilted plane. 3D representation of the measured points (black dots), along with the interpolating surface (mesh).

Metallic cylinder

Fig. 4.13 presents measurements on the inner side of a sanded aluminium cylinder of 16 mm diameter, obtained with the configuration using only one fiber and the ball lens for illumination. Again, the Local FFT approach has been used for filtering. Black dots represent the measured points, and the mesh was obtained by fitting with RBF, with normals estimated with the MVANE method, as defined in section 3.4. Here the delay stage was scanned with steps of 1 mm. Even though the field of view is enhanced with the use of the ball lens, the algorithm fails to extract the signal on all the circonference. This is due to the fact that the intensity is adequate for points in the vicinity of the optical axis of the illumination fiber, but not high enough for points situated further. On this measurement, points situated around x=2.5 mm, y=-3 mm are falsely located, and thus an erroneous dimension of the cylinder in this area is clearly apparent. A possible reason is that these points are situated in the border of the illuminated zone, and thus they receive only a small amount of optical power compared to the others.
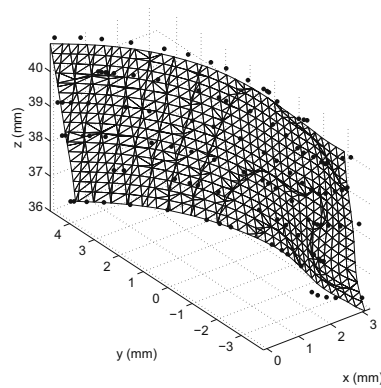
Figure 4.13: Measurement on a metallic cylinder, using the configuration with a single fiber and a ball lens to extend the illuminated area.

Lung optical phantom

Results on fig. 4.14 were obtained using the optical phantom described in Ref. [69]. The sample reproduces the tissues optical properties as well as the geometry of upper airways, it is made of silicone with added scattering particles (Al_2O_3) and dye to adjust for scattering and absorption coefficient, respectively. The delay stage was moved by steps of 1 mm between each interferogram acquisition. Here also, the Local FFT filtering procedure has been applied. Compared to measurements on metallic samples, or even on lightly diffusing material such as white paper, it was necessary to increase the acquisition time and gain setting. High variations of the reflected signal were observed in some points, probably

due to local inhomogeneities of the scattering particles embedded in the phantom. These variations make it difficult to adjust the camera settings in order to avoid saturated pixels.

(a)   (b)
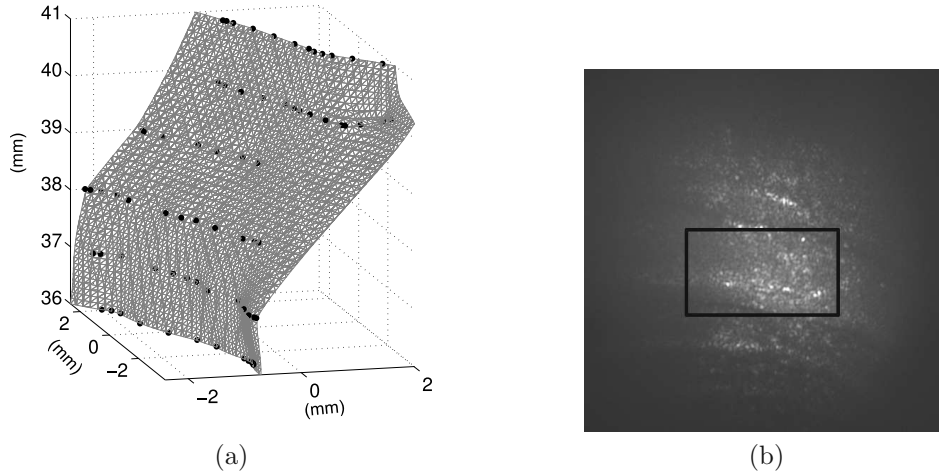
Figure 4.14: Measurement on a surrogate of bronchi [69]. (a) final 3D reconstruction of a part of the model wall. (b) Normal endoscopic view as captured with the system, with the zone of interest delineated.

Pig trachea wall and pig bronchial wall

Fig. 4.15 and 4.16 show results obtained on an *ex vivo* pig trachea sample and a pig bronchus sample, respectively. Here a Gabor filterbank eq. 3.5 has been shown to perform well. The separation between each acquired curve level is 1 mm for both measurements. Contrary to the phantom measurement, there were no high local variations of the intensity, and saturation of pixels was not as problematic.

(a)   (b)

Figure 4.15: Pig trachea measured ex vivo. (a) final 3D reconstruction of a part of the trachea wall. (b) picture of the measured ex-vivo trachea part.
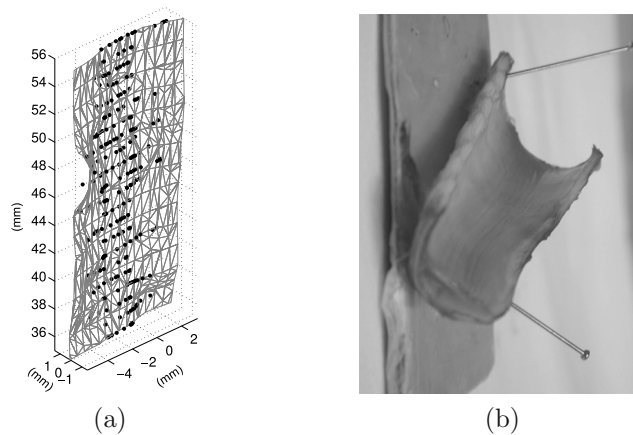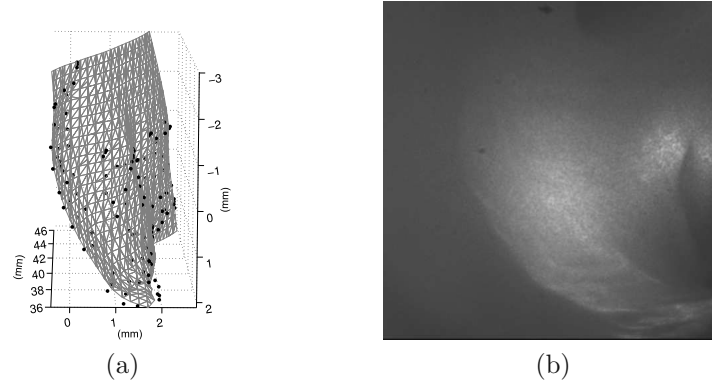
Figure 4.16: Pig bronchial wall measured ex vivo. (a) final 3D reconstruction of a part of the bronchial wall. (b) Normal endoscopic view as captured with the system.

The acquisition time is a critical parameter, as the sample is a dynamic medium. Small deformations of the sample, due for example to water evaporation at the surface, can produce fringes blurring if the integration time of the CCD is too long, thus preventing curve extraction. It has been empirically determined that for acquisition times higher than 2 ms, contrast of fringes becomes too low to be detected. In particular, a limitation of the setup is that it requires long acquisition times (1-2 ms) to achieve imaging with a suitable fringes contrast. This issue also prevents correct contour line extraction on moving samples or when the endoscope is not still during an acquisition. In order to reduce the acquisition time, use of high sensitivity and high speed cameras, such as electron multiplier CCD, could be considered. However, these cameras are most of the time very large and heavy. In such a case the camera cannot be attached directly to the endoscopic part, as it will be much too difficult for the endoscopist to precisely manipulate the device, thus requiring for example to transmit the interferogram or the image through fiber optics next to the vicinity of the sensor plane, and then form an image. Another way to solve this issue would be to use pulsed laser light, thus delivering high power during a short period of the CCD integration time.

Three fibers illumination

Using 3 fibers for illumination gives consequently the advantage of distributing the illumination power more homogeneously on the entire field of view. The signal extraction procedure can be used to obtain 3D information for different points on the circonference, allowing to interpolate a closed surface for a tube-like shape (fig. 4.17) The fibers are placed in a way that the 3 illumination zones are not overlapping, so that it is possible to extract sequentially the signal for every illuminated area.

Paper cylinder

Fig. 4.17 is a measurement on a paper cylinder of 9 mm diameter. The Gabor filterbank convolution filtering has been applied. Surface normals direction have been estimated with the CSNE method. Off-surface points for surface rendering have been created 2 mm away from the measured points, along the normal direction. γ parameter has been set to 2.5.
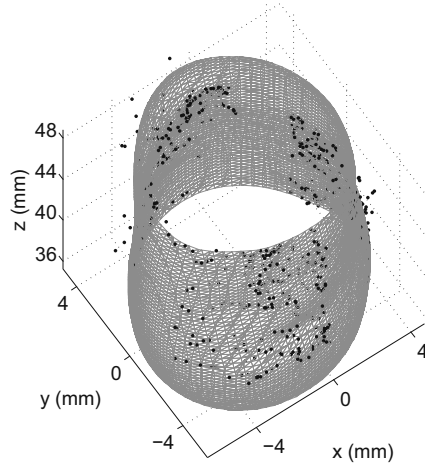
Figure 4.17: Measurement on a paper cylinder, using the setup shown in fig. 4.1, with 3 fibers for illumination.

As a reminder, the precision on this measurement has been extensively investigated in section 3.4, RMSE between the actual radius of the cylinder and the radius of the raw extracted points is 0.73 mm. A RMSE of 0.95 mm and 1.03 mm is achieved on the fitted surface when using CSNE and MVANE method for normal estimation, respectively.

Pig bronchus

Fig. 4.18 presents a measurement obtained on a small *ex-vivo* pig bronchus using 3 fibers for illumination. Separation between each acquired interferogram is 0.2 mm, which results in a data cloud points of 972 tri-dimensional coordinates. RBF interpolation has been made over 30×30×30 voxels, and 2240 vertexes are obtained after isosurfacing. Artefacts are clearly present on the tri-dimensional reconstruction in the lower right corner, around coordinates $(0, 2, 36)$. The measured diameter of the bronchus is about 8 mm, which is in agreement with the evaluation of the diameter that can be made with a calliper.

A source of imprecisions on biological samples is related to the light penetrating the sample: part of the photons encounter scattering. After a few scattering event, these
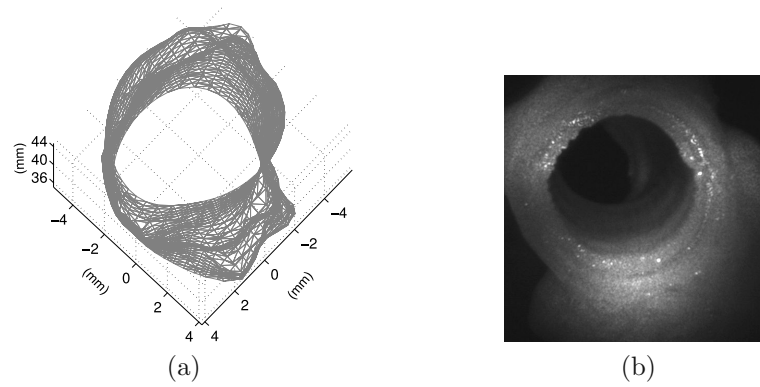
Figure 4.18: Pig bronchus measured ex vivo. (a) final 3D reconstruction. (b) Normal endoscopic view as captured with the system.

photons can potentially be back-scattered in the direction of the detector and propagate with a time delay enabling interference with the reference wave. Such photons are coming from positions closer to the endoscope than the one to be isolated, and a wider interference pattern is observed.

4.7   Precision assessments

In the previous section different measurements have been presented. Amongst them, two have been used for precision assessment, namely the measurement on the plane and the measurement on the cylinder that has been thoroughfully used in chap. 3 to chose the parameters for surface fitting, using 3 fibers for illumination. Table 4.1 summarizes the results. For sake of comparison, let just recall the measured physical lateral resolution limit of 0.3 mm obtained in subsec. 4.3.2 through the MTF measurement, and the axial limit given by the coherence length of 0.3 mm.

Object	Measured Value	Value
Plane	RMSE between points and fitted plane	0.4 mm
Cylinder	RMSE on measured radius[4]	0.73 mm
Fitted cylinder 1[5]	RMSE on fitted radius	0.95 mm
Fitted cylinder 2[6]	RMSE on fitted radius	1.03 mm
Lateral resolution	MTF cutoff frequency[7]	center: 4.5 mm^{-1} border: 3.2 mm^{-1}
Axial resolution	Coherence length	0.3 mm
Manually assessed stenosis length by an endoscopist	Landmarks placed on the endoscope	$\pm$ 3 mm

Table 4.1: Precision assessment

For the measurement on the plane, the achieved accuracy is close to the limit imposed by the lateral resolution of the endoscope and the coherence length. The decline in precision between the measurement on the plane and the measurement on the cylinder has to be interpreted very cautiously: indeed, for the plane the RMSE is calculated between the measured point, and a least square fit of a plane on these points. For the cylinder measurement, the RMSE is evaluated between the measured radius (either on the raw extracted points or on the fitted points), and the actual value of 4.5 mm, which has been determined with a calliper. So the two values cannot be compared directly.

---

[4]Real radius: 4.5 mm.
[5]CSNE for normal creation.
[6]MVANE for normal creation.
[7]For a plane situated at 30 mm from the endoscope distal end.

Nevertheless, one source of imprecision for the measurement on the cylinder relates to the procedure used to relocate the points in the referential of the object: in this procedure, the image magnification is taken into account, and as here 3 fibers are used for illumination, it means that 3 different scale changes have to be considered, which increases the impact of the measurement uncertainty of this factor.

4.8 Conclusion

In contrast with indirect imaging techniques, such as magnetic resonance imaging, low-coherence endoscopy allows for measurements directly *in situ*, e.g. within an operating room, and therefore does not require a patient to be moved to an imaging facility.

The endoscope has been characterized in term of its modulation transfer function, and its design has been back-engineered. This has permitted to attest that the inherent small aperture of a rigid endoscope acts as the diaphragm of the simple interferometric setup described in chapter 2, allowing, in an off-axis configuration, for the creation of interference fringes superposed to the speckle pattern. With the use of filters presented in chapter 3, it is possible to acquire the depth information in a single acquisition. However, an issue that has still to be resolved, and prevents to head toward clinical investigation, relates to the question of scan time. A possible solution has been mentioned, in which the interferograms are acquired on the fly as the endoscopist manipulate the device. For this approach to be finalized, the orientation of the endoscope has to be recorded instead of the delay stage position. Impact of the illumination design on the detectability of the signal has been highlighted, and two different systems for illumination have been proposed. Acquisition time can be further shortened by using pulsed light, in order to minimize fringes blurring. A complete software environment has been developed, giving access to interferograms acquisition, signal processing and measured surface visualization in the same application. A compact solution (overall volume $115 \times 83 \times 94$ mm) for the realization of the device has been designed, characterized, and tested. The device is directly adjustable to any rigid endoscope by simply updating the length of the reference fiber, and potentially, can also be adapted to flexible endoscopes. Measurements have been performed on several samples, amongst which *ex vivo* pig sample. It has been demonstrated that our low-coherence endoscopic system can be successfully used to obtain 3D imaging of upper airways.

Chapter 5

Conclusion

This thesis focuses on a novel approach for optical tri-dimensional contouring, requiring only one acquisition to extract a contour depth. It is based on an interferometer, using a reduced coherence light source (a low-cost laser diode), and it is fully adaptable to endoscopic procedure commonly in used in ear-nose-throat medicine. It has been demonstrated that the method can be successfully applied to imaging of porcine upper airways. Although this method uses interferometry to obtain depth range measurement, the phase signal is not directly evaluated, rather the location of the coherent superposition of two waves is extracted, similarly to the coherence radar, or light-in-flight method, and thus provides a robust technique even in harsh environment. The key feature is to extract the coherent area on the image by locating intentionally induced fringes created by off-axis superposition of a smooth reference wave and an object wave coming from an optical system with limited aperture.

A model for the propagation of the light through the optical system has been developed. It takes into account the broadened emission spectrum of the light source, as well as the speckle effect induced by the illumination of a rough surface with the partially coherent light. Simulated results have been carefully compared with measurements, they have been proved to have the same characteristics, both in the spatial domain and in the Fourier domain. This study helped in designing a suitable arrangement for the endoscopic system. The aperture size of the imaging system has been revealed to have a critical impact on the detectability of the depth signal.

Measurements have been undertaken on several different materials and geometries. Namely, from simple paper plane, paper cylinders and cones, wooden samples, metallic and ceramic samples, to *ex-vivo* pig trachea and bronchus parts. It has been proved that the method can be used in a wide set of configurations, from almost totally specular samples to samples with a lot of scattering, as in the bronchus, and also when practically only grazing light travels back to the detector, as when observing "tube-like" structures.

Different filters have been investigated in order to extract the depth information from acquired interferograms. By using Gabor filterbanks, which are in a sense Gaussian modulated and rotated variations of the Fourier basis functions, selectivity of the extracted signal has been enhanced by a factor of 1.3 compared to a simple local Fourier spectrum evaluation, and time of the extraction procedure divided by 6, even when compared to fast iterative calculation in the Fourier spectrum. These filters do not need any *a priori* knowledge of the signal. However, if any knowledge in term of frequency or orientation on the signal to detect is available, it has been demonstrated that the selectivity can be further enhanced by a factor of 2.5, keeping the calculation time as short or even shorter. A simple calibration procedure can be applied in order to determine the local frequencies or orientations of the fringes that have to be extracted.

Radial basis functions interpolation have been used in order to provide a tri-dimensional view of the observed surface, with an emphasis on the adaptation of surface normals calculation for surface mapping on unorganized points measured on tube-like samples. It was shown that the determination of the local least variance axis on a neighborhood of the cloud data points is the most efficient technique when observing only a part of a cavity wall, but that the mapped surface can be more precisely fitted by imposing a cylindrical shape when observing closed pipes.

Taking into account each steps of the procedure up to surface rendering, the precision of the method has been assessed by measurements on well defined samples such as planes and cylinders. The fringe pattern filtering process and the extraction of the 3D points have been characterized with the observation of a tilted plane, for different values of the tilt angle. A root mean square error between the final imaged plane and the measured points of 0.4 mm has been achieved when using a light source with a coherence length of 0.3 mm, which corresponds to the precision of the method. An accuracy of 0.7 mm has been reached when observing a cylindrical geometry with multiple illumination fibers. A survey of the impact of the surface fitting parameters on the final precision has been conducted. This has permitted to choose values for these parameters in order to achieve robust surface mapping. At the end of the fitting procedure, the root mean square error between the interpolated surface and the real object coordinates is in the order of 1 mm.

A compact prototype has been designed and built, with a multiple fibers arrangement for illumination. The system is separated in two parts: the first one that is attached to the rigid endoscope, and contains imaging as well as recombining object/reference wave optics, and the detector, fits into a box with overall dimensions of $115 \times 83 \times 94$ mm. The second part contains the laser source, the scanning arm and the injection optics for the fibered system. It is designed to be left on a small cart. This provides a device that can be potentially brought to the bedside, or used during routine endoscopic check-up.

Associated with the device, a complete framework has been elaborated in order to simplify the acquisition procedure as well as the signal processing. This results in a fully automated environment taking in charge hardware control, data storage and signal processing, up to the tri-dimensional scene rendering.

Perspectives

This thesis project started as a rather practical research problem, as the focus was to investigate and build a first example of a device giving access to quantitative dimensioning of upper airways. As in many other scientific research, some issues have been resolved, and new ones also encountered, that are still to be investigated further.

Making the system totally compatible with standards rigids endoscopes was a big challenge, and took more time than expected, especially the design of the illumination system. Anyway, this system can still be enhanced, adding more illumination fibers would certainly increase the efficiency. Another important improvement could be made if using pulsed laser light, short high power light pulses would allow for reduced acquisition time without damaging the tissues, and thus enhance the robustness of the system with regards to vibrations or sample changes during measurements. But this raises the question of the modification of the coherence properties of the source when using pulsed light.

In an operating room environment, it is hardly impossible for the medical staff to maintain the endscope in the same position during all the scanning process. In order to achieve robust total tri-dimensional surface topography, the contouring should take place completely independently of any long delay stage shift. One way to achieve this goal could be to acquire the interferograms on the fly during usual endoscopic navigation. In this sense, the integration of a sensor to record the endoscope orientation in order to re-position the extracted contour line in an absolute coordinate system will be required. Commercial solutions such as gyroscopes or magnetic trackers could be used for that purpose.

On the software side, more realistic 3D rendering could be achieved with the help of an implementation of a fast RBF interpolation algorithm, in order to be able to interpolate on data cloud points of more than 2000 sample points.

Besides these practical aspects, there are more fundamental studies that could be very interesting. In particular it was observed that the characteristic of the fringe pattern, such as the visibility of the fringes, and their spreading, changes as function of the material under study. It is clear that the coherent pattern created, the superposition of the slow varying speckle pattern and of the interference between the object and reference wave, has a close relationship with the intrinsic optical properties of the tissues,

such as the absorption coefficient, and the scattering coefficient with its associated phase function. Concerning this aspect, measurements of the tissue properties of pig trachea and bronchial tubes can be found in appendix B. An idea would be to point out how these coefficients affect the visibility and the spreading of the interference pattern. A study of this relationship could potentially open new applications in the field of tissues characterization.

Bibliography

[1] J. Dumon, "A dedicated tracheobronchial stent," Chest **97**(2), 328–332 (1990). 1

[2] G. Simpson, M. Strong, G. Healy, S. Shapshay, and C. Vaughan, "Predictive factors of success or failure in the endoscopic management of laryngeal and tracheal stenosis," Ann Otol Rhinol Laryngol **91**, 384–388 (1982). 1

[3] J. J. Armstrong, M. S. Leigh, I. D. Walton, A. V. Zvyagin, S. A. Alexandrov, S. Schwer, D. D. Sampson, D. R. Hillman, and P. R. Eastwood, "In vivo size and shape measurement of the human upper airway using endoscopic long-range optical coherence tomography," Optics Express **11**(15), 1817–1826 (2003). 3, 14, 53

[4] J. Schmitt, "Optical Coherence Tomography (OCT): a review," IEEE Journal on Selected Topics in Quantum Electronics **5**(4), 1205–1215 (1999). 3, 9, 53

[5] L. Froehly, S. N. Martin, T. Lasser, C. Depeursinge, and F. Lang, "Multiplexed 3D imaging using wavelength encoded spectral interferometry: A proof of principle," Optics Communications **222**(1-6), 127–136 (2003). 3, 53

[6] A. Tumlinson, J. Barton, B. Povazay, H. Sattman, A. Unterhuber, R. Leitgeb, and W. Drexler, "Endoscope-tip interferometer for ultrahigh resolution frequency domain optical coherence tomography in mouse colon," Optics Express **14**(5), 1878–1887 (2006). 3

[7] D. Yelin, W. White, J. Motz, S. Yun, B. Bouma, and G. Tearney, "Spectral-domain spectrally-encoded endoscopy," Optics Express **15**(5), 2432–2444 (2007). 3, 53

[8] J. Zara and C. Lingley-Papadopoulos, "Endoscopic OCT approaches toward cancer diagnosis," IEEE Journal on Selected Topics in Quantum Electronics **14**(1), 70–81 (2008). 3, 9

[9] F. Chen, G. M. Brown, and M. Song, "Overview of three-dimensional shape measurement using optical methods," Optical Engineering **39**(1), 10–22 (2000). 3

[10] H. Takasaki, "Moiré Topography," Applied Optics **9**(6), 1467–1472 (1970). 3

[11] S.-W. Kim, Y.-B. Choi, and J.-T. Oh, "Reverse engineering: High speed digitization of free-form surfaces by phase-shifting grating projection moiré topography," International Journal of Machine Tools and Manufacture **39**(3), 389–401 (1999). 3

[12] C. Hernandez, G. Vogiatzis, and R. Cipolla, "Multiview photometric stereo," IEEE Transactions on Pattern Analysis and Machine Intelligence **30**(3), 548–554 (2008). 3

[13] B. Forster, D. VanDeVille, J. Berent, D. Sage, and M. Unser, "Complex wavelets for extended depth-of-field: A new method for the fusion of multichannel microscopy images," Microscopy Research and Technique **65**(1-2), 33–42 (2004). 3

[14] J. Mitic, "Application of CMOS image sensors in optical sectioning and polarization microscopy," Ph.D. thesis, EPFL, Lausanne (2004). 3

[15] J. Goodman, "Statistical properties of laser speckle patterns," Laser Speckle and Related Phenomena pp. 9–75 (1975). 4, 21

[16] J. W. Goodman, "Some fundamental properties of speckle," J. Opt. Soc. Am. **66**(11), 1145–1150 (1976). 4, 21

[17] U. Schnars and W. Jüptner, "Digital recording and numerical reconstruction of holograms," Measurement Science and Technology **13**(9), R85–R101 (2002). 5

[18] E. Cuche, P. Marquet, and C. Depeursinge, "Simultaneous amplitude-contrast and quantitative phase-contrast microscopy by numerical reconstruction of Fresnel off-axis holograms," Applied Optics **38**(34), 6994–7001 (1999). 5, 23

[19] I. Yamaguchi, J.-I. Kato, S. Ohta, and J. Mizuno, "Image formation in phase-shifting digital holography and applications to microscopy," Applied Optics **40**(34), 6177–6186 (2001). 5

[20] P. Smigielski, F. Albe, and B. Dischli, "Real-time holographic endoscopy," in *Holography, Interferometry, and Optical Pattern Recognition in Biomedicine II*, vol. 1647, pp. 186–193 (Publ by Int Soc for Optical Engineering, Los Angeles, CA, USA, 1992). 5

[21] O. Coquoz, "Endoscopic holography with a muticore optical fiber applied to biomedical imaging," Ph.D. thesis, EPFL (1994). 5

[22] S. Schedin, G. Pedrini, H. J. Tiziani, and A. K. Aggarwal, "Comparative Study of Various Endoscopes for Pulsed Digital Holographic Interferometry," Appl. Opt. **40**(16), 2692–2697 (2001). 5, 53

[23] G. Pedrini, M. Gusev, S. Schedin, and H. J. Tiziani, "Pulsed digital holographic interferometry by using a flexible fiber endoscope," Optics and Lasers in Engineering **40**(5-6), 487–499 (2003). 6, 53

[24] T. S. Anaya, F. M. Santoyo, M. DeLaTorre-Ibarra, G. Pedrini, and W. Osten, "Endoscopic pulsed digital holography for 3D measurements," Optics Express **14**(4), 1468–1475 (2006). 6, 54

[25] T. S. Anaya, M. D. la Torre, and F. M. Santoyo, "Microstrain detection using simultaneous endoscopic pulsed digital holography," Optical Engineering **47**(7), 073601 (pages 4) (2008). 6, 54

[26] E. Kolenovic, W. Osten, R. Klattenhoff, S. Lai, C. von Kopylow, and W. Jüptner, "Miniaturized Digital Holography Sensor for Distal Three-Dimensional Endoscopy," Appl. Opt. **42**(25), 5167–5172 (2003). 6, 53

[27] P. Massatsch, "Low coherence digital holographic microscopy : applications to vision in turbid media and biomedical imaging," Ph.D. thesis, EPFL, Lausanne (2003). 6

[28] R. Jones and C. Wykes, *Holographic and Speckle Interferometry* (Cambridge University Press, 1989). 6

[29] M. Lehmann, "Statistical theory of two-wave speckle interferometry and its application to the optimization of deformation measurements," Ph.D. thesis, EPFL, Lausanne (1998). 6

[30] R. Sirohi, "Speckle interferometry," Contemporary Physics **43**(3), 161–180 (2002). 6, 7

[31] P. Jacquot, "Speckle interferometry: A review of the principal methods in use for experimental mechanics applications," Strain **44**(1), 57–69 (2008). 6

[32] Y. Hung and H. Ho, "Shearography: An optical measurement technique and applications," Materials Science and Engineering R: Reports **49**(3), 61–87 (2005). 6

[33] G. Jaisingh and F. P. Chiang, "Contouring By Laser Speckle." Applied Optics **20**(19), 3385–3387 (1981). 8, 15

[34] C. Joenathan, R. K. Mohanty, and R. S. Sirohi, "Contouring by speckle interferometry," Opt. Lett. **10**(12), 579 (1985). 8, 15

[35] R. Rodriguez-Vera, D. Kerr, and F. Mendoza-Santoyo, "Electronic speckle contouring," J. Opt. Soc. Am. A **9**(11), 2000 (1992). 8, 15, 53

[36] D. V. Prieto and J. Garcia-Sucerquia, "Three-dimensional surface contouring of macroscopic objects by means of phase-difference images," Appl. Opt. **45**(25), 6381–6387 (2006). 8, 15

[37] R. Tatam, J. Davies, C. Buckberry, and J. Jones, "Holographic surface contouring using wavelength modulation of laser diodes," Optics & Laser Technology **22**(5), 317–321 (1990). 8, 15

[38] M. Takeda and H. Yamamoto, "Fourier-transform speckle profilometry: three-dimensional shape measurements of diffuse objects with large height steps and/or spatially isolated surfaces," Applied Optics **33**(34), 7829–7837 (1994). 8, 15

[39] J. Kandulla, B. Kemper, S. Knoche, and G. VonBally, "Two-wavelength method for endoscopic shape measurement by spatial phase-shifting speckle-interferometry," Applied Optics **43**(29), 5429–5437 (2004). 8, 53

[40] M. Huang and B.-S. Yun, "Self-marking phase-stepping electronic speckle pattern interferometry (ESPI) for determining a phase map with least residues," Optics and Laser Technology **39**(1), 136–148 (2007). 8

[41] Q. Yu, S. Fu, X. Liu, X. Yang, and X. Sun, "Single-phase-step method with contoured correlation fringe patterns for ESPI," Optics Express **12**(20), 4980–4985 (2004). 8

[42] H. Yun, C. Hong, and S. Chang, "Least-squares phase estimation with multiple parameters in phase-shifting electronic speckle pattern interferometry," Journal of the Optical Society of America A: Optics and Image Science, and Vision **20**(2), 240–247 (2003). 8

[43] B. Bhaduri, M. Kothiyal, and N. Mohan, "A comparative study of phase-shifting algorithms in digital speckle pattern interferometry," Optik **119**(3), 147–152 (2008). 8, 15

[44] T. Bothe, J. Burke, and H. Helmers, "Spatial phase shifting in electronic speckle pattern interferometry: Minimization of phase reconstruction errors," Applied Optics **36**(22), 5310–5316 (1997). 8

[45] B. Bhaduri, N. K. Mohan, M. P. Kothiyal, and R. S. Sirohi, "Use of spatial phase shifting technique in digital speckle pattern interferometry (DSPI) and digital shearography (DS)," Opt. Express **14**(24), 11,598–11,607 (2006). 8, 15

[46] S. Knoche, B. Kemper, G. Wernicke, and G. von Bally, "Modulation analysis in spatial phase shifting electronic speckle pattern interferometry and application for automated data selection on biological specimens," Optics Communications **270**(1), 68–78 (2007). 8

[47] B. Bhaduri, N. Mohan, and M. Kothiyal, "Digital speckle pattern interferometry using spatial phase shifting: Influence of intensity and phase gradients," Journal of Modern Optics **55**(6), 861–876 (2008). 8

[48] B. Kemper, J. Kandulla, D. Dirksen, and G. von Bally, "Optimization of spatial phase shifting in endoscopic electronic speckle pattern interferometry," Optics Communications **217**(1-6), 151–160 (2003). 8, 54

[49] B. Kemper, D. Dirksen, W. Avenhaus, A. Merker, and G. VonBally, "Endoscopic double-pulse electronic-speckle-pattern interferometer for technical and medical intracavity inspection," Applied Optics **39**(22), 3899–3905 (2000). 8, 53

[50] M. Matham and N. Sujatha, "Digital speckle pattern interferometry for deformation analysis of inner surfaces of cylindrical specimens," Applied Optics **43**(12), 2400–2408 (2004). 8

[51] B. E. A. Saleh and M. C. Teich, *Fundamentals of Photonics* (Wiley Interscience, 1991). 8, 20, 61

[52] M. Laubscher, "Innovative experimental concepts for optical coherence tomography," Ph.D. thesis, EPFL, Lausanne (2004). 9

[53] T. Dresel, G. Häusler, and H. Venzke, "Three-dimensional sensing of rough surfaces by coherence radar," Appl. Opt. **31**(7), 919–925 (1992). 9, 13, 16

[54] W. An and T. Carlsson, "Digital measurement of three-dimensional shapes using light-in-flight speckle interferometry," Optical Engineering **38**(8), 1366–1370 (1999). 9

[55] B. Nilsson and T. Carlsson, "Simultaneous measurement of shape and deformation using digital light-in-flight recording by holography," Optical Engineering **39**(1), 244–253 (2000). 9, 16

[56] T. Carlsson, B. Nilsson, and J. Gustafsson, "System for acquisition of three-dimensional shape and movement using digital Light-in-Flight holography," Optical Engineering **40**(1), 67–75 (2001). 9

[57] I. Balboa, H. D. Ford, and R. P. Tatam, "Low-coherence optical fibre speckle interferometry," Measurement Science and Technology **17**(4), 605–616 (2006). 9, 15, 54

[58] A. Ellerbee and J. Izatt, "Phase retrieval in low-coherence interferometric microscopy," Optics Letters **32**(4), 388–390 (2007). 9

[59] P. Egan, M. Whelan, F. Lakestani, and M. Connelly, "Random depth access full-field low-coherence interferometry applied to a small punch test," Optics and Lasers in Engineering **45**(4), 523–529 (2007). 9

[60] C. Sheppard, M. Roy, and M. Sharma, "Image formation in low-coherence and confocal interference microscopes," Applied Optics **43**(7), 1493–1502 (2004). 9

[61] J. a. Izatt, M. R. Hee, G. M. Owen, E. A. Swanson, and J. G. Fujimoto, "Optical coherence microscopy in scattering media," Optics Letters **19**(8), 590–592 (1994). 9

[62] M. Davidson, K. Kaufman, and I. Mazor, "Coherence probe microscope." Solid State Technology **30**(9), 57–59 (1987). 9

[63] W. Oh, B. Bouma, N. Iftimia, R. Yelin, and G. Tearney, "Spectrally-modulated full-field optical coherence microscopy for ultrahigh-resolution endoscopic imaging," Optics Express **14**(19), 8675–8684 (2006). 9

[64] C. Dunsby, Y. Gu, and P. French, "Single-shot phase-stepped wide-field coherence-gated imaging," Optics Express **11**(2), 105–115 (2003). 9

[65] M. S. Hrebesh, Y. Watanabe, and M. Sato, "Profilometry with compact single-shot low-coherence time-domain interferometry," Optics Communications **281**(18), 4566–4571 (2008). 9, 16

[66] J. Kuhn, T. Colomb, F. Montfort, F. Charrière, Y. Emery, E. Cuche, P. Marquet, and C. Depeursinge, "Real-time dual-wavelength digital holographic microscopy with a single hologram acquisition," Opt. Express **15**(12), 7231–7242 (2007). 9

[67] P. Somers and N. Bhattacharya, "Maintaining sub-pixel alignment for a single-camera two-bucket shearing speckle interferometer," Journal of Optics A: Pure and Applied Optics **7**(6), S385–S391 (2005). 10

[68] K. Creath, "PHASE-SHIFTING SPECKLE INTERFEROMETRY." in *Proceedings of SPIE - The International Society for Optical Engineering*, vol. 556, pp. 337–346 (1985). 13, 15

[69] R. Bays, G. Wagnières, D. Robert, J.-F. Theumann, A. Vitkin, J.-F. Savary, P. Monnier, and H. van den Bergh, "Three-dimensional optical phantom and its application in photodynamic therapy," Lasers in Surgery and Medicine **21** (1997). 13, 71, 72

[70] T. E. Carlsson and B. Nilsson, "Measurement of distance to diffuse surfaces using non-scanning coherence radar," Journal of Optics **29**(3), 146–151 (1998). 16

[71] T. Colomb, E. Cuche, F. Charrière, J. Kühn, N. Aspert, F. Montfort, P. Marquet, and C. Depeursinge, "Automatic procedure for aberration compensation in digital holographic microscopy and applications to specimen shape compensation," Appl. Opt. **45**(5), 851–863 (2006). 20

[72] J. Uozumi and T. Asakura, "First-order probability density function of the laser speckle phase," Optical and Quantum Electronics **12**(6), 477–494 (1980). 21

[73] S. Equis and P. Jacquot, "Simulation of speckle complex amplitude: Advocating the linear model," in *Speckle06: Speckles, From Grains to Flowers*, vol. 6341, pp. – (Nimes, 2006). 21

[74] W. Lauterborn, T. Kurz, and M. Wiesenfeldt, *Optique cohérente*, vol. Enseignement de la Physique (Masson, 1997). 22

[75] E. Cuche, F. Bevilacqua, and C. Depeursinge, "Digital holography for quantitative phase-contrast imaging," Opt. Lett. **24**(5), 291–293 (1999). 25

[76] T. Randen and J. Husoy, "Filtering for texture classification: A comparative study," IEEE Transactions on Pattern Analysis and Machine Intelligence **21**(4), 291–310 (1999). 34

[77] J.-D. Boissonnat and F. Gazais, "Smooth surface reconstruction via natural neighbour interpolation of distance functions," Computational Geometry: Theory and Applications **22**(1-3), 185–203 (2002). 34

[78] H. Hoppe, T. DeRose, T. Duchamp, J. McDonald, and W. Stuetzle, "Surface reconstruction from unorganized points," Computer Graphics (ACM) **26**(2), 71–78 (1992). 34

[79] J. Carr, W. Richard Fright, and R. Beatson, "Surface interpolation with radial basis functions for medical imaging," IEEE Transactions on Medical Imaging **16**(1), 96–107 (1997). 34, 44

[80] M. Arigovindan, M. Sühling, P. Hunziker, and M. Unser, "Variational image reconstruction from arbitrarily spaced samples: A fast multiresolution spline solution," IEEE Transactions on Image Processing **14**(4), 450–460 (2005). 34

[81] C. Vazquez, E. Dubois, and J. Konrad, "Reconstruction of nonuniformly sampled images in spline spaces," Image Processing, IEEE Transactions on **14**(6), 713–725 (2005). 34

[82] L. Greengard, "Fast Algorithms for Classical Physics," Science **265**(5174), 909–914 (1994). 34, 45

[83] R. Beatson, J. Cherrie, and C. Mouat, "Fast fitting of radial basis functions: Methods based on preconditioned GMRES iteration," Advances in Computational Mathematics **11**(2-3), 253–270 (1999). 34, 45

[84] R. Beatson, W. Light, and S. Billings, "Fast solution of the radial basis function interpolation equations: Domain decomposition methods," SIAM Journal of Scientific Computing **22**(5), 1717–1740 (2001). 34, 45

[85] A. Faul, G. Goodsell, and M. Powell, "A Krylov subspace algorithm for multiquadric interpolation in many dimensions," IMA Journal of Numerical Analysis **25**(1), 1–24 (2005). 34, 45

[86] L. Wang, B. Yuan, and X. Tang, "Implicit surface reconstruction from noisy 3D scattered data," in *International Conference on Signal Processing Proceedings, ICSP*, vol. 2 (2007). 34, 45

[87] N. Mitra and A. Nguyen, "Estimating surface normals in noisy point cloud data," in *Proceedings of the Annual Symposium on Computational Geometry*, pp. 322–328 (2003). 34, 46

[88] M. Unser, "Local Linear Transforms for Texture Measurements," Signal Process. **Vol. 11**, Pp. 61–78 (1986). 36

[89] I. Kalliomäki and J. Lampinen, "On steerability of Gabor-type filters for feature detection," Pattern Recogn. Lett. **28**(8), 904–911 (2007). 37

[90] F. Charrière, T. Colomb, F. Montfort, E. Cuche, P. Marquet, and C. Depeursinge, "Shot-noise influence on the reconstructed phase image signal-to-noise ratio in digital holographic microscopy," Applied Optics **45**(29), 7667–7673 (2006). 42

[91] H. Hopkins, "Optical system having cylindrical rod-like lenses, USA Patent number 3257902," (1960). 59

[92] S. Dobson and H. Hopkins, "A new rod-lens relay system offering improved image quality," Journal of Physics E: Scientific Instruments **22**(7), 450–455 (1989). 59

[93] S. Dobson, "An easily manufactured rod-lens relay system with improved image quality," Measurement Science and Technology **3**(7), 674–677 (1992). 59

[94] T. Tomkinson, J. Bentley, M. Crawford, C. Harkrider, D. Moore, and J. Rouke, "Rigid endoscopic relay systems: A comparative study," Applied Optics **35**(34), 6674–6683 (1996). 59

[95] M. Born and E. Wolf, *Principles of Optics: Electromagnetic Theory of Propagation, Interference and Diffraction of Light* (Cambridge University Press, 1999). 61

[96] J. W. Goodman, *Introduction to Fourier optics* (Roberts, 2005). 61

[97] M. Gu, *Advanced Optical Imaging Theory* (Springer, 1999). 61

[98] F. Bevilacqua, "Local optical characterization of biological tissues in vitro and in vivo," Ph.D. thesis, EPFL, Lausanne (1998). 93

[99] P. Thueler, "Optical spectral probing for epithelial tissue characterisation," Ph.D. thesis, EPFL, Lausanne (2000). 94
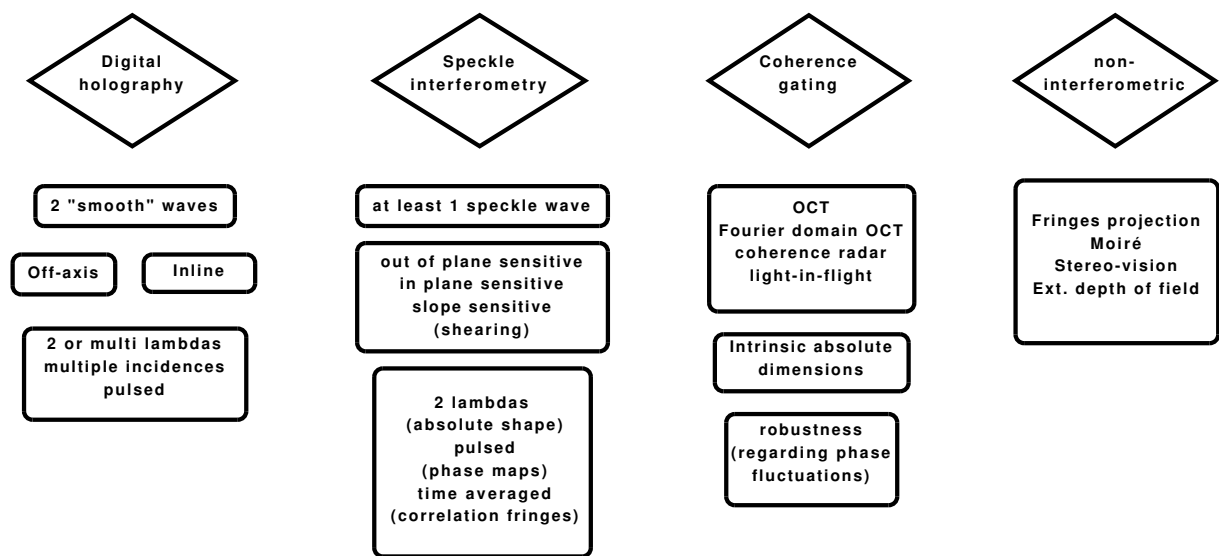
Appendix A

Optical contouring methods

Digital holography	**Speckle interferometry**	**Coherence gating**	**non-interferometric**

2 "smooth" waves

Off-axis   **Inline**

2 or multi lambdas multiple incidences pulsed

at least 1 speckle wave

out of plane sensitive in plane sensitive slope sensitive (shearing)

2 lambdas (absolute shape) pulsed (phase maps) time averaged (correlation fringes)

OCT Fourier domain OCT coherence radar light-in-flight

Intrinsic absolute dimensions

robustness (regarding phase fluctuations)

Fringes projection Moiré Stereo-vision Ext. depth of field

Figure A.1: Flow chart summary of contouring methods, with some key features.

Appendix B

Optical coefficients of pig bronchial parts

In a biological sample, light undergoes different interaction: at interface, light can be reflected or refracted, when light is refracted in the tissue, it can be absorbed, or, when looking at the trajectory of a specific photon, it can finally be emitted in a different direction after having interacted with microscopic dielectric variation, which is called scattering.

The *absorption coefficient* μ_a is defined as the probability of absorption per unit of infinitesimal pathlength, and the *scattering coefficient* μ_s is the scattering probability per unit of infinitesimal pathlength. Their inverse correspond to the associated mean free paths.

If a scattering event occurs, the probability per unit solid angle for a change of direction of the photon is given by the *phase function*. The first moment of the phase function is the *anisotropy factor* g_1. It represents the mean value of the cosine of the scattering angle. If the medium is isotropic, which is generally assumed for biological samples, the phase function depends only on the scattering angle. In tissue, g_1 is typically between 0.7-0.99, which means that the scattering is preferably in the forward direction. The *reduced scattering coefficient* μ_s' is defined as:

$$\mu_s' = \mu_s \left(1 - g_1\right),$$

where g_1 is the 1st order moment of the phase function.

The *diffusion coefficient* D is linked to these parameters by $D = \left[3\left(\mu_a + \mu_s'\right)\right]^{-1}$. The *transport mean free path* is defined as $mfp' = \left(\mu_a + \mu_s'\right)^{-1}$, for more informations, the interested reader can refer to Dr. Bevilacqua's thesis [98].

In his thesis Bevilacqua showed that in reflectance geometry, the number of moments

to take into account was related to the distance ρ between the source and detection of diffusely reflected light. The closer the detection is made from the source, the more anisotropic is the radiance and the greater is the number of moments to take into account. When $0.5 \leqslant \rho\mu_s' \leqslant 5$, the phase function could not be considered as linearly anisotropic, but that its two first moments g_1 and g_2 should be taken into account. g_1 is related to forward scattering. The 2nd moment, g_2, is related to Rayleigh-Gans scattering.

It is possible to define the parameter γ:

$$\gamma = \frac{1 - g_2}{1 - g_1}.$$

γ is unitless and in the range $[0, +\infty[$. γ decreases when the backscattering becomes more important and/or when the number of small particles with respect to the wavelength increases.

By modifying the random phase term added to the object field in section 2.3 with respect to these parameters it should be possible to take into account the contribution of the scattered light to the speckle effect. Further investigations have to be performed in order to clearly identify how the scattering is linked to the speckle phenomenon.

In order to measure μ_a and μ_s' on sample taken from a pig bronchial tree, the *Micromed*® reflectance probe developed by Dr. Thueler during his thesis has been used [99].Measurement have been performed on different locations, namely on sites on the trachea, on a primary bronchus, and on a secondary bronchus (see fig. B.2 for a schematic of these different locations in the case of a human bronchial tree).
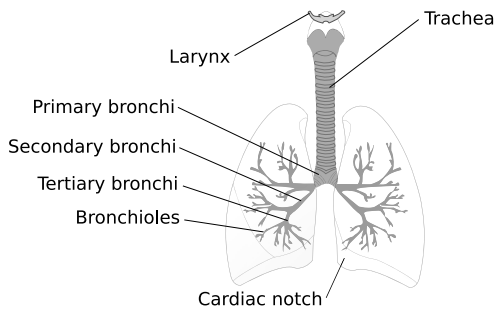

Figure B.2: Schematic of a bronchial tree (from wikipedia.org [1])

Fig. B.1 shows the absorption coefficients measured on the chosen pig bronchial parts. The absorption peaks due to hemoglobin, centered around 525 nm and 560 nm, are clearly visible on the two bronchi samples. For these two curves, the two peaks shape is similar to the absorption spectrum of oxy-hemoglobin. When looking at the absorption of the trachea sample, no high absorption peak can be observed.

Fig. B.3 presents the reduced scattering coefficient, for the 3 chosen bronchial parts. For the two bronchi sample, the measured values for wavelengths below 580 nm were probably corrupted by the high absorption peaks due to oxy-hemoglobin, as the peaks are clearly visible in the scattering spectrum, too. As well, for the trachea sample, values for wave-

---

[1]http://en.wikipedia.org/wiki/Image:Diagrama_de_los_pulmones.svg
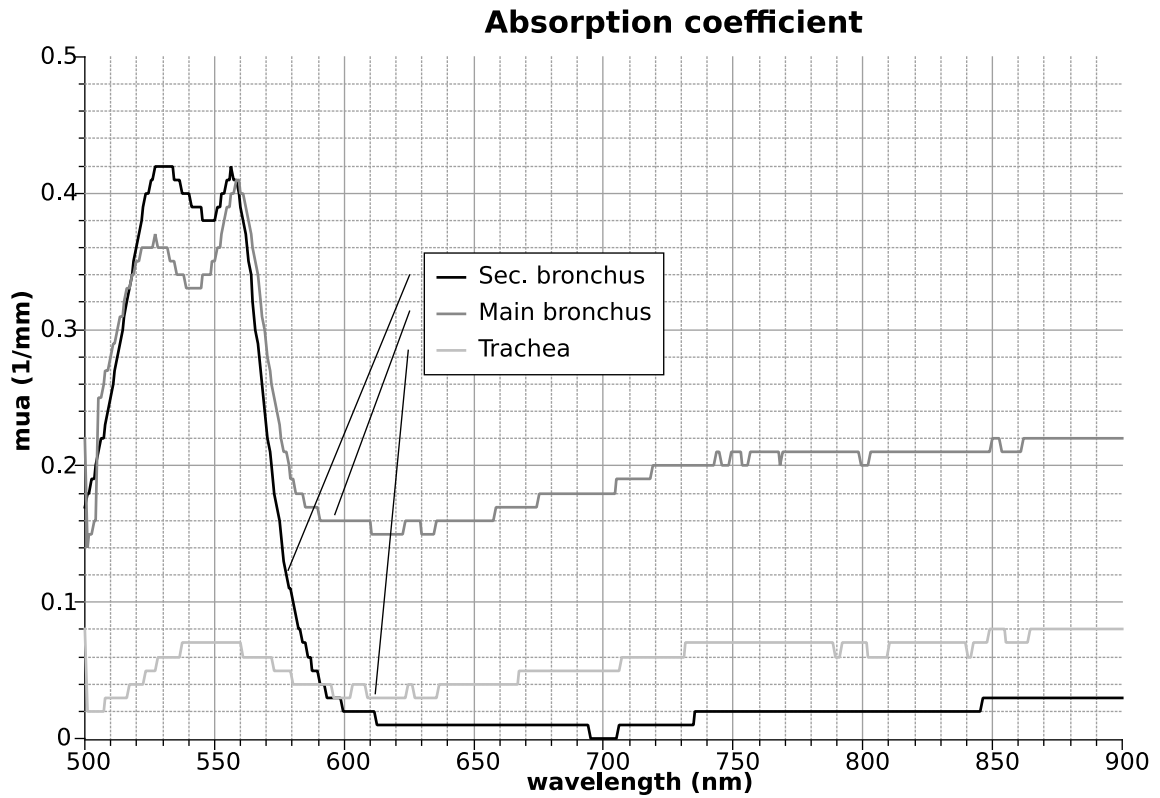
Absorption coefficient

Figure B.1: Absorption coefficient (μ_a) of pig bronchus.

lengths above 840 nm seem to be insignificant, regarding the discontinuity of the curve. It can be observed that for 661 nm, which is the central wavelength of the laser source used in the endoscopic setup, all the samples show low absorption and quite high reduced scattering.

As an indication, γ for trachea parts is almost constant over the whole spectrum and has a value around 1. On the other hand, for bronchial parts, γ tends to get bigger (around 2.5), but it is still constant over the whole spectrum. This shows that the trachea parts are more likely to have higher backscattering than bronchial parts, which is also observed with eye inspection.
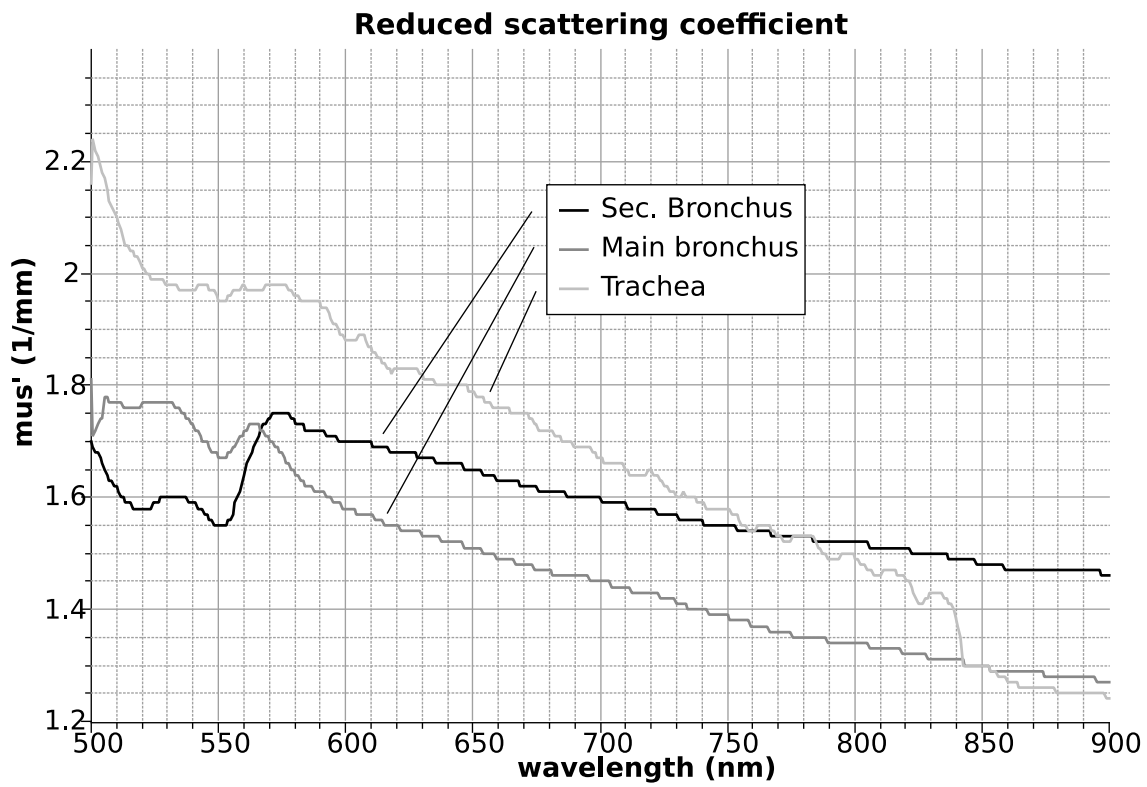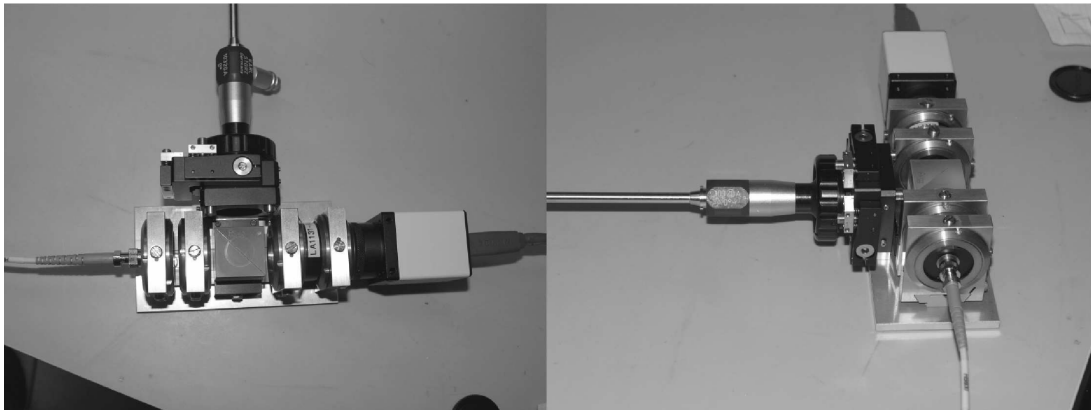
Figure B.3: Reduced scattering coefficient (μ'_s) of pig bronchial parts.

Appendix C

Prototype snapshots

Figure C.1: Snapshot of the prototype endoscopic module. Overall dimensions: $115 \times 83 \times 94$ mm.
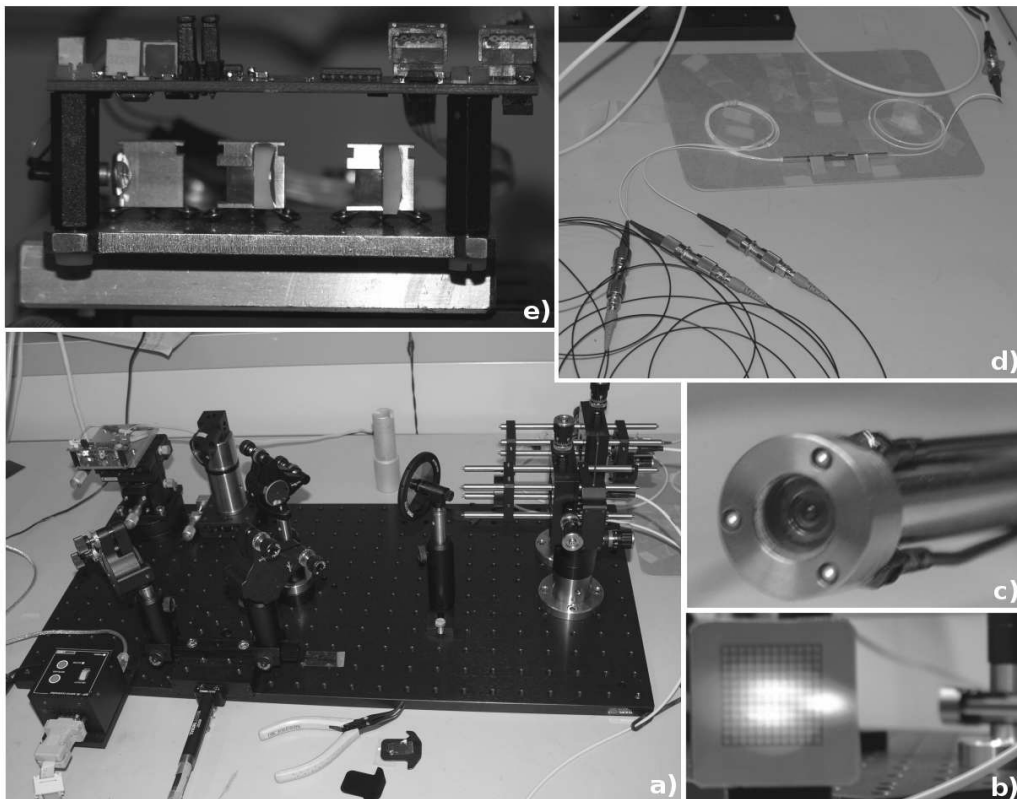
Figure C.2: Snapshot of the prototype bench module. (a) bench module, (b) typical illuminated zone, here on a tilted paper plane, (c) zoom of the mount for 3 fibers illumination system, (d) view of the 1×3 fiber coupler and the 3 patch-cables for illumination, (e) reduced coherence laser source.

Appendix D

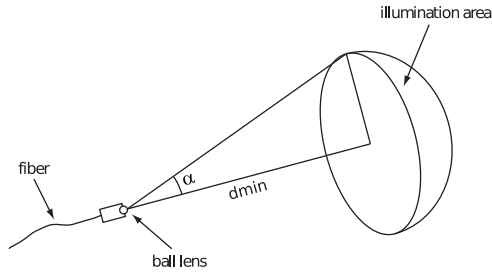# Evaluation of laser illumination hazards

Figure D.1: Eye risk-free conditions.

As established by the ANSI standard Z136.1, chapter 8.2.2, the maximum permissible exposure (MPE) for a cw laser emitting with a wavelength between 0.4 and 1.4 μm is 2.6 mW/cm^2, for an aversion response time of the eye of 0.25 s. Based on this normalization, it is possible to estimate the minimal distance between the laser illumination system and the eye that is considered as "risk-free", commonly called the Nominal Ocular Hazard Distance (NOHD),

$$d \geq \sqrt{\frac{P_{max}}{MPE} \cdot \frac{1}{2\pi \left(\frac{1-\cos\alpha}{\cos^2\alpha} \right)}}$$

Where α is half the angle of divergence of the illumination system.

In the case of the illumination with the ball-lens design described in subsec. 4.4.2, our laser illumination system delivers a maximum power (Pmax) of 15 mW with $\alpha = 18.64°$, thus eye damage might occurs if the system is pointed toward the eyes with a distance between the ball lens and the eye $d_{min} = 4$ cm.

For the system using 3 illumination fibers, $\alpha = 6.65°$, and the maximum power delivered by one fiber is Pmax = 5 mW, which gives the condition $d_{min} = 6.7$ cm.

Anyway the system will be in use only when the endoscope is inserted in the trachea observing the region of interest for the stenosis diagnosis. But to prevent any hazard due to a malfunction of the hardware when removing the endoscope from the patient, laser

illumination should shut down or protective eyewear could be worn for the patient. It is important to denote that the illumination power of the system is in the same range as the one emitted by a barcode reader, which is a laser class I product.

Norms:
– ANSI Z136.1, United States National Consensus Standards for laser safety.
– IEC 60825, International Electrotechnical Commission, Safety for Laser Products.

Appendix E

Application note on software implementation

All the algorithms described in chap. 3 have been developed in the *Matlab*® environment. The acquisition procedure and the delay stage control, on the other hand, take place in *Labview*®. In order to provide a complete user-friendly package, a library has been build with the set of *Matlab* algorithms. Calling this library directly from *Labview* is not possible, as all the compiled code is set around a specific type of data, the `mxArray` type, which integrates matrices in C code. In order to encapsulate into `mxArray` the data to be processed and pass them to the *Matlab* library (and vice-versa), a "wrapping" library has been developed. Fig. E.1 shows a flow chart of the software package.

The interface needs a couple of files as input:

- a configuration text file, containing some values needed for the system to operate properly, such as the pixel size of the CCD, or the length of the illumination fibers.

- 3 binary images, needed to perform the masking operation for each fibers.

- 2 text files, containing the orientation and frequency map needed to perform matched Gabor filtering.

The *Labview* interface is in charge of saving the measurements. It is possible to save each step of the procedure, the interferograms, the filtered images and the post processed images are saved either as picture files or as text files containing the values as double precision floats. The coordinates of the delay stage are also saved, as they are necessary if offline processing has to be performed further. Of course, the final 3D data points clouds are saved, as well as the RBF interpolated data.

Calls are made in *Labview* to the wrapping library for 3 groups of *Matlab* functions:
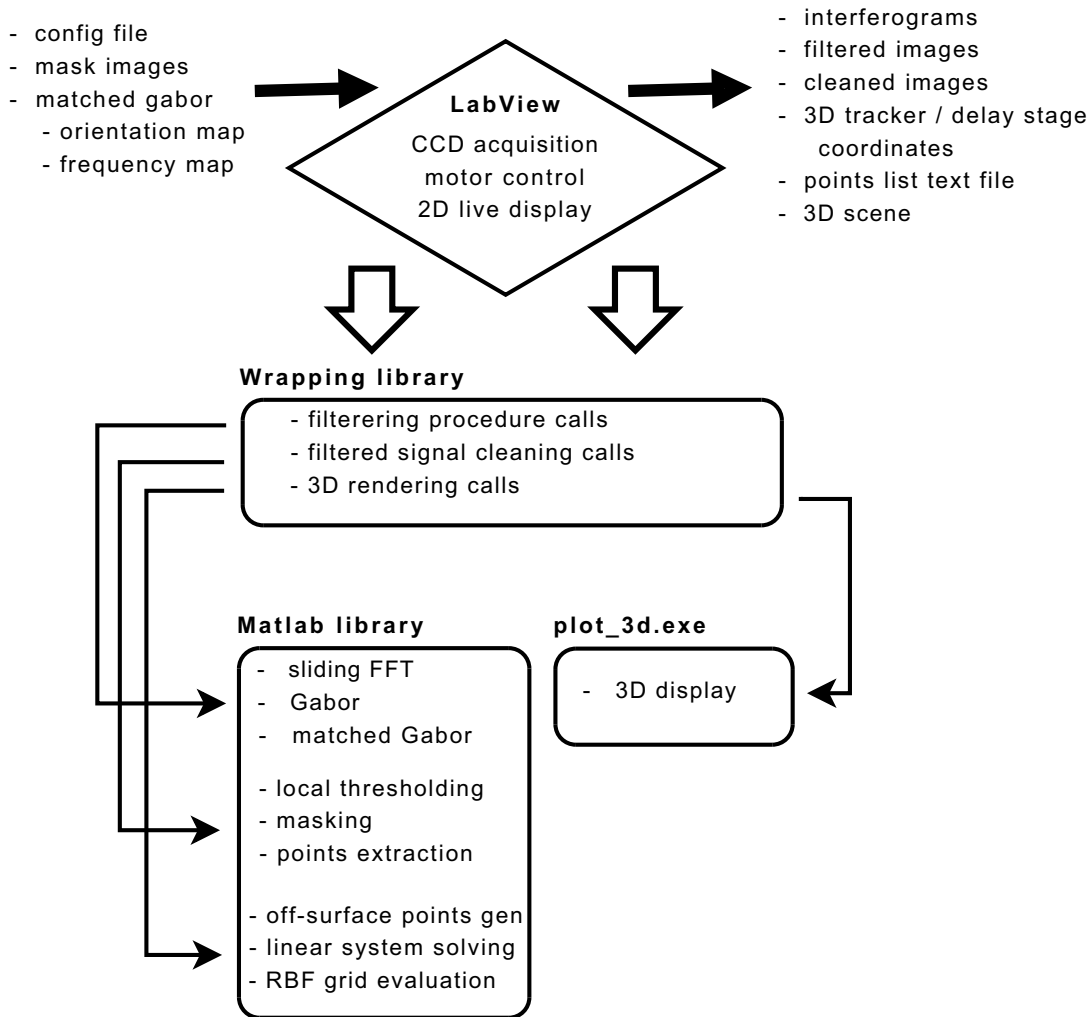
Figure E.1: Flow chart of the software package.

- the filtering procedure calls are used to access the desired functions in charge of the chosen filtering technique described in 3.2. The incremental formulation of the local FFT filter, the Gabor filter and the matched Gabor filter are implemented.

- The filtered signal cleaning calls deal with the algorithms in charge of local thresholding, masking procedure for 3 fibers illumination and 3D coordinates extraction.

- Off-surface point generation, solving of the linear system in eq. 3.10 and RBF evaluation are handled by the 3D rendering calls.

For 3D scene display and manipulation, an external program is started when the user presses the corresponding button in *Labview*.

This approach has been found to bring valuable modularity and flexibility. Indeed, the algorithms have been implemented with the high power of matrix computing, along with the numerous extension toolboxes available in *Matlab*, and the hardware has been easily

interfaced in the *Labview* environment. Beside this, for future software development, one can simply enhance functionality by creating new *Matlab* functions and calling them in the right function of the wrapping library, there is no need to dig into the modification of the *Labview* interface.

Yves Delacrétaz
Ch. de la Forêt 2
1052 Le Mont-sur-Lausanne
Switzerland
++41 78 892 96 37
y.delacretaz@a3.epfl.ch
29 years old, swiss

Microengineering with a specialization in biomedical optics.

EDUCATION

2008 PhD, "Endoscopic Low Coherence Interferometry Applied to Tri-Dimensional Contouring of Upper Airways", Ecole Polytechnique Fédérale de Lausanne (EPFL), thesis director: Prof. C. Depeursinge.

2004 Master of Science MSc in Microengineering (EPFL, orientation: applied photonics).

1998 BAC, type C, Lausanne.

WORK EXPERIENCE

11.2005 - 12.2008 Research assistant at the Advanced Photonics Laboratory (APL), EPFL.

Development of a new method for optical 3D contouring and realization of a prototype to achieve 3D imaging of upper-airways through commonly used rigid endoscopes. Development of an integrated software environment for acquisition, signal processing and 3D rendering to create an easy to use measurement system. Patent pending. Supervision of a Master thesis work, teaching assistant for practical works, teaching assistant for Bachelor and Master degree courses.

11.2004 – 10.2005 Research engineer at the Optical Fiber Devices group, APL, EPFL: "Fiber attenuator reliability under high optical power", under the leadership of Dr. H. Limberger.

Fabrication of Fiber Bragg gratings (FBGs) and FBGs based Fabry-Perot resonators using excimer 193 nm laser and frequency doubled Ar+ laser. Characterization of the temperature induced local fiber Bragg grating wavelength shift using high power laser irradiation, which revealed applications in remote wavelength tuning for optical communication networks and sensing applications. Modeling of heat flow in fiber attenuators using Comsol MultiPhysics[R].

05.2004 – 10.2004 Engineer at the Microvision and microdiagnostics group, APL, EPFL: "Design of a device to demonstrate 3D endoscopy for bronchial parts", under the leadership of Prof. C. Depeursinge.

3D contouring method for endoscopic applications demonstration through the realization of a bench lab setup.

08.2002 – 09.2002 Training period at the biomedical maintenance workshop of the Centre Hospitalier Universitaire Vaudois (CHUV), Lausanne.

Dialysis devices maintenance. Normalized check-up and reparation of the peristaltic pump systems. On site assistance.

UNDERGRADUATE PROJECTS

03.2003 – 06.2003 "Measurement of Thin Water Layers by Spectroscopy", NAM, ITOP, EPFL.
Water layers assessment in Pelton wheel runnels. The approach permitted to obtain robust angle-free measurements with a precision of 2% on a range of several centimeters.

10.2002 – 02.2003 "Modeling of the Electrostimulated Muscular Contraction", LSR2, IPR, EPFL.
Through the development and the implementation under Matlab/Simulink$^{(R)}$ of the inverse model of the electrostimulated muscular contraction, this project permitted to determine the steady state as well as the transient current amplitude to apply to electrode patches in order to recreate specific movements of the leg for paraplegic rehabilitation.

LANGUAGES

French	Mother tongue
English	Speaking: experimented (C1 level), writing: experimented (C2 level)
German	Basics (gymnasium level)

TECHNICAL SKILLS

Optics	Coherent and incoherent imaging, image acquisition, interferometers design, image/signal processing, fiber optics, high power lasers.
Computing	• OS: Windows / Linux (administration). • Publishing: LATEX, Office, Photoshop, Illustrator. • Programming: C/C++, Java, Matlab/Simulink, Labview, HTML. • CAD: Proe and Solidworks (3D modeling), Zemax (Optical design), Comsol Multiphysics (FEM modeling).

INTERESTS AND PERSONAL SKILLS

Sports	Cycling, snowboarding, mountain walking.
Leisure Computing	Open source software and OS, web design.
Interpersonal	Non-violent communication theory, introspection.

PUBLICATIONS POSTPONED DUE TO PATENT FILLING

1. Y. Delacretaz, F. Lang, and C. Depeursinge. *Off-axis low coherence interferometry contouring.* To be submitted, 2008.
2. Y. Delacretaz, F. Lang, and C. Depeursinge. *Endoscopic low coherence interferometry in upper airways.* To be submitted, 2008.
3. Y. Delacretaz, D. Boss, F. Lang, and C. Depeursinge. *Fringe extraction and 3d data cloud points representation applied to low coherence interferometry.* To be submitted, 2008.